Universidade do Porto

Faculdade de Engenharia

Master's Thesis

Failure prediction in composite wing-box for civil transport aircraft via global-local analysis: with focus on skin-stringer certification

Guilherme Fernandes

Supervisor: Professor Volnei Tita

Thesis submitted to Universidade do Porto – Faculdade de Engenharia
in partial fulfillment of the requirements for the degree of
Master in Mechanical Engineering - Aeronautical and Vehicles Structures

MEM



Departamento de Engenharia Mecânica
Faculdade de Engenharia

October, 2023

Candidate: Guilherme Fernandes, No. 201806137, up201806137@up.pt

Scientific Guidance: Prof. Dr. Volnei Tita, voltita@sc.usp.br

Scientific Co-Guidance: Prof. Dr. Federico Danzi, fdanzi@inegi.up.pt



Departamento de Engenharia Mecânica
Faculdade de Engenharia
Rua Dr. Roberto Frias, Porto

October, 2023

"Thoughts without content are empty,
intuitions without concepts are blind."

Immanuel Kant

Acknowledgements

As I approach the culmination of my enriching five-year academic journey at the Faculty of Engineering of the University of Porto, I am overwhelmed with gratitude for the incredible opportunities I have been blessed with. This moment would not have been possible without the unwavering support and guidance of the exceptional individuals who have played pivotal roles in my success.

First and foremost, I extend my deepest appreciation to my esteemed mentors, Professor Volnei Tita and Professor Federico Danzi. Their expertise, wisdom, and ceaseless belief in my potential have been instrumental in shaping my academic growth and the successful completion of this thesis. Their guidance and encouragement throughout this journey has been truly invaluable, and I am honoured to have collaborated with such distinguished academics.

I also extend my heartfelt thanks to Prof. Carolina Furtado for generously providing the time and resources to share constant advices and guide me throughout the entirety of the thesis.

To all my esteemed professors, I express my gratitude for imparting knowledge that has left a lasting impact on me. The teachings I have received from each of you will continue to guide me in all my future endeavours. Furthermore, my sincere appreciation also goes to my dear colleagues and friends. Your constant encouragement and assistance have been a driving force in my pursuit of excellence, both academically and personally. I cherish the camaraderie we share and the memories we have created together.

Lastly, I would like to extend my gratitude to my beloved parents, José and Glória, whom which I owe the deepest debt of gratitude due to the unwavering support, love, and patience that have been the foundation of my achievements.

Abstract

Within the aeronautical industry, due to their insurmountable mechanical properties, unidirectional prepreg laminates embody the standard composite materials. Despite this, carbon fibre-reinforced polymers still present disadvantages when compared to the traditional metallic alloys, in terms of production and certification costs. Thereby, with technology improving as well as the knowledge on failure mechanisms in these structures, it is imperative to push towards the limits of engineering and develop numerical tools that ease the costs of certifying certain aeronautical components.

This thesis undertakes a thorough investigation into the use of the Global-Local approach for analysing carbon fibre-reinforced polymers (CFRPs) in the domain of aviation constructions. The commencement of the trip entails a comprehensive initiation, including the articulation of the issue, contextual backdrop, aims, and the arrangement of the thesis, so establishing the foundation for the ensuing inquiry. The state-of-the-art and literature review section provides an overview of the development of composite materials within the aeronautical sector. Certification procedures pertaining to aviation materials undergo thorough scrutiny, hence offering valuable insights into the many methods, standards, and regulations that are implemented to guarantee the airworthiness of such materials.

The following part focuses mostly on the numerical modelling of damage in composite materials. This study provides a comprehensive analysis of several failure processes seen in composite materials, including the failure of both fibres and matrices, along with the occurrence of delamination. The section on numerical modelling outlines the process of creating a composite damage model, with a particular focus on cohesive zone models and continuum damage mechanics. This study provides a comprehensive examination of intralaminar damage modes, specifically focusing on fibre fracture and inter-fibre fracture. The investigation serves as a foundational basis for later analyses.

The validation of the numerical model is performed by means of a skin-stringer model, which encompasses the utilisation of experimental data and the validation of the Finite Element Model. The material characteristics of various components,

such as carbon fibre reinforced polymers (CFRPs), adhesives, and cohesive elements, undergo thorough characterization processes. The study presents a comprehensive set of numerical data, which includes global analysis, where a full shell model is developed in order to depict the displacement field that will later be transmitted to the local one. Herein, several analysis are conducted in order to validate this procedure, specifically, displacement fields, stress distributions and the load-displacement curve are studied to assure the reliability of this step. After, a full solid model with ply-by-ply discretisation, paired with cohesive zone modelling is developed and thus, validated. The same line of thought is applied and complemented by a delamination analysis. The effectiveness of the Global-Local method in accurately representing intricate CFRP failure behaviour is proven.

The study concludes with an examination of a wing-box, which entails the creation of a finite element model, determination of boundary conditions and loading conditions, and conducting global and local model simulations. At this point, after achieving a validated strategy, the same global shell model is developed and paired with a local solid model with ply-by-ply discretisation. Here, with the lack of experimental results, the analysis consists on a logical assessment of the values achieved by these numerical models. Despite intensive testing, the final strategy developed failed when transferring the displacement field between models and, thus, main conclusions are presented at the end of this section. The final portion of the paper addresses the limitations of the study and proposes potential avenues for further research. Here, main discoveries are presented so that a better understanding of the restrictions of this methodology is achieved. Thereby, the adopted standard modelling approach does not appear valid for extremely complex structures, such as the one in study.

Ultimately, this thesis highlights the significant impact that CFRPs have on the field of aeronautical engineering, emphasising the crucial role the development of new analytical and numerical methods. The application of the Global-Local approach in achieving safe aircraft structures is of essence and thus, the main motivation throughout this project. Withal, in light of the limitations identified, future research should focus on more appropriate material sub-routines, as well as the improvement of the method towards geometrical intricate structures.

Keywords: Composite materials, Finite element method, Damage, Aeronautical structure, Global-local technique.

Resumo

Na indústria aeronáutica, devido às suas propriedades mecânicas inultrapassáveis, os laminados pré-impregnados unidireccionais constituem o padrão dos materiais compósitos. Não obstante, os polímeros reforçados com fibra de carbono apresentam, ainda, desvantagens face às tradicionais ligas metálicas, tanto em termos de custos de produção como de certificação. Por conseguinte, devido a constantes melhorias tecnológicas e desenvolvimento do conhecimento sobre os mecanismos de falha nas estruturas compósitas, é imperativo ultrapassar os limites da engenharia atuais e desenvolver ferramentas numéricas que reduzam os custos de certificação dos componentes aeronáuticos.

A presente dissertação retrata uma investigação exaustiva sobre a utilização da abordagem global-local para a análise de polímeros reforçados com fibras de carbono (CFRPs) no domínio das estruturas aeronáuticas. O início da viagem implica uma iniciação abrangente, incluindo a articulação da questão, o contexto, os objectivos e a organização da tese, estabelecendo assim as bases para a investigação que se segue. A secção do estado da arte e da revisão da literatura apresenta uma panorâmica do desenvolvimento dos materiais compósitos no sector aeronáutico. Os processos de certificação relativos aos materiais aeronáuticos são alvo de um exame minucioso, onde são descritas informações valiosas sobre os muitos métodos, normas e regulamentos que são implementados para garantir a aeronavegabilidade destes componentes.

A seguinte secção centra-se, sobretudo, na modelação numérica de danos em materiais compósitos. Este estudo fornece uma análise abrangente de vários processos de falha observados em materiais compósitos. A utilização da análise de sub-modelação no Abaqus e a sua aplicação na análise de um painel-longarina são elementos fundamentais desta abordagem. A secção sobre modelação numérica descreve o processo de criação de um modelo de dano composto, com especial incidência nos modelos de zonas coesivas e na mecânica do dano contínuo. Este estudo fornece uma análise abrangente dos modos de dano intralaminar, focando especificamente a fratura das fibras e a fratura entre fibras. A investigação serve como base fundamental para análises posteriores.

A validação do modelo numérico é efectuada através de um modelo painel-longarina, que engloba a utilização de dados experimentais e a validação do modelo de elementos finitos. As características materiais de vários componentes, tais como polímeros reforçados com fibras de carbono (CFRPs), adesivos e elementos coesivos, são objeto de processos de caraterização exaustivos. O estudo apresenta um conjunto abrangente de dados numéricos, que inclui uma análise global, onde é desenvolvido um modelo de casca completo para representar o campo de deslocamentos que será posteriormente transmitido ao modelo local. Para validar este procedimento, são realizadas várias análises, nomeadamente, os campos de deslocamentos, as distribuições de tensões e a curva carga-deslocamento são estudados para garantir a fiabilidade deste passo. Posteriormente, é desenvolvido e validado um modelo sólido completo com discretização por camadas, associado à modelação de zonas coesivas. A mesma linha de pensamento é aplicada e complementada por uma análise de delaminação. A eficácia do método Global-Local na representação exacta do comportamento de rotura dos CFRP é comprovada.

O estudo termina com a análise de uma caixa de asa, o que implica a criação de um modelo de elementos finitos, a determinação das condições de fronteira e das condições de carga, e a realização de simulações globais e locais do modelo. Nesta altura, depois de obtida uma estratégia validada, o mesmo modelo global de casca é desenvolvido e emparelhado com um modelo local de sólido com discretização camada a camada. Neste ponto, com a falta de resultados experimentais, a análise consiste numa avaliação lógica dos valores obtidos por estes modelos numéricos. Apesar dos testes intensivos, a estratégia final desenvolvida falhou na transferência do campo de deslocamentos entre modelos e, por isso, as principais conclusões são apresentadas no final desta secção. A parte final do artigo aborda as limitações do estudo e propõe potenciais caminhos para investigação futura. Aqui, são apresentadas as principais descobertas para que se possa compreender melhor as restrições desta metodologia. Assim, a abordagem de modelação padrão adoptada não parece ser válida para estruturas extremamente complexas, como a que está em estudo.

Em jeito de conlusão, esta dissertação realça o impacto significativo que os CFRPs têm no domínio da engenharia aeronáutica, enfatizando o papel crucial do desenvolvimento de novos métodos analíticos e numéricos. A aplicação da abordagem Global-Local na obtenção de estruturas aeronáuticas é essencial e, portanto, a principal motivação ao longo deste projeto. No entanto, tendo em conta as limitações identificadas, a investigação futura deverá centrar-se em sub-rotinas de

materiais mais adequadas, bem como na melhoria do método para estruturas geometricamente complexas.

Palavras-Chave: Materiais compósitos, método dos elementos finitos, estrutura aeronáutica, técnica global-local, dano.

Contents

List of Figures xi

List of Tables xv

List of Acronyms xvii

I Introduction 1

1 Introduction 3

1.1 Problem Statement . . . 3
1.2 Background . . . 4
1.3 Objectives . . . 5
1.4 Thesis layout . . . 6

II State-of-art and literature review 9

2 Composite materials in the aeronautical industry 11

2.1 Composite Structures in Aircrafts . . . 11
2.2 Aircraft Materials Certification . . . 14
2.2.1 Approaches and criteria for aircraft design . . . 15
Damage Tolerant . . . 16
Safe-life Design . . . 17
Fail-safe Design . . . 18
2.2.2 Regulations . . . 18
Part 23 - Airworthiness Standard: Normal, Utility. Acrobatic, and Commuter Category Airplanes. . . . 22
Part 25 - Airworthiness Standard: Transport Category Airplanes. . . . 23

3 Numerical modelling of damage in composite materials 27

3.1 Composite Failure Mechanisms . . . 27
3.1.1 Fibre and Matrix failure . . . 28
3.1.2 Delamination . . . 34

Failure Modes . . . 34
Strain energy release rate - G . . . 35
Delamination models . . . 35
3.1.3 Finite Element Methodology applied to composite materials . 37
Hashin Model in ABAQUS . . . 38
Interface Elements . . . 40
3.1.4 Skin-Stringer applications . . . 40
3.2 Global-Local Technique . . . 44
3.2.1 Abaqus Submodelling analysis . . . 45
Shell-to-solid submodeling in Abaqus . . . 45
3.2.2 Global-Local Technique in skin-stringer analysis . . . 46

III Numerical model **51**

4 Composite Damage Model **53**
4.1 Cohesive Zone Models . . . 53
4.2 Continuum damage mechanics . . . 61
4.2.1 Introduction . . . 61
4.2.2 Intralaminar material model . . . 62
Compliance tensor calculation: first approach . . . 63
Compliance tensor calculation: second approach . . . 63
4.2.3 3D stiffness tensor of the damaged model . . . 65
4.2.4 Intralaminar damage evaluation strategy . . . 66
4.2.5 Intralaminar damage modes: Fibre Fracture (FF) . . . 68
Longitudinal tensile damage model . . . 68
Longitudinal compressive damage model . . . 69
4.2.6 Intralaminar damage modes: inter fibre fracture (IFF) . . . 69
Transverse tensile damage mode . . . 69
Transverse compressive damage mode . . . 69
4.2.7 In-plane shear damage mode . . . 70
4.2.8 Smeared crack formulation . . . 71

5 Skin-stringer validation **75**
5.1 Experimental Data . . . 75
5.2 Finite Element Model Validation . . . 77
5.2.1 Material properties . . . 77
Carbon-fibre reinforced polymer . . . 77
Adhesive and Cohesive Elements . . . 77
Stringer filament . . . 78
5.2.2 Global model . . . 78

5.2.3 Local Models 81

6 Numerical results **83**
6.1 Global analysis 83
6.1.1 Displacement Field 84
6.1.2 Stress Distribution 85
6.1.3 Reaction Forces 85
6.2 Local Results 87
6.2.1 Displacement Field 87
6.2.2 Stress Distribution 88
6.2.3 Reaction Forces 90
6.2.4 Delamination Analysis 91

IV Wing-box analysis **95**

7 Finite Element Model **97**
7.1 Wing-box geometry 97
7.2 Boundary Conditions 100
7.3 Loading Conditions 101
7.4 Limit and ultimate loading 106
7.5 Global Model 109
7.6 Local Model 111

8 Wing-Box Results **113**
8.1 Global Results 113
8.2 Local Results 114

V Limitations and Conclusion **117**

9 Limitations **119**

10 Conclusions and future work **123**
10.1 Conclusions 123
10.2 Future work 127

Appendix A Wing-box Global Model Results **141**
A.1 Displacement Field, U 142

List of Figures

2.1 Percentage of total structural weight attributed to composites and the use of composites [14], [15]. 13
2.2 Mission profile and consequent stress spectrum [23]. 15
2.3 Durability and Damage Tolerance design routines for airframe structures [27], [30]. 16
2.4 Building block approach to certification [20], [37]. 20
2.5 Metal fatigue crack damage and non-growing damage in composite materials [37]. 24

3.1 Fibre failure evolution in an UD composite under axial tension [51]. 28
3.2 Fracture modes [69]. 34
3.3 Sources of delamination in composite materials [69]. 35
3.4 Mixed Mode-I and Mode-II delamination criteria [69]. 36
3.5 Equivalent stress versus displacement [80]. 39
3.6 Geometry of the specimen analysed [89] 42
3.7 Discrete interface elements connecting skin and stringer parts [89]. . 42
3.8 Center zone in shell-to-solid submodeling [104]. 46
3.9 Two-way loose coupling procedure for skin-stringer failure mechanisms [89]. 47

4.1 Top: FPZ of a quasi-brittle material. Middle: CZM concept. Bottom: stress distribution along the crack path for a constant cohesive law under pure mode I loading [107]. 54
4.2 Tri-linear cohesive law obtained by superposing two bi-linear laws [108]. 56
4.3 Spatial representation of a cohesive element. [115] 56
4.4 Traction-separation response [115]. 57
4.5 Illustration of mixed-mode response in cohesive elements [115]. . . . 59
4.6 Strain energy density G and complementary strain energy density G^* for the unidirectional case 64
4.7 Details of the implemented progressive failure procedure [116]. . . . 67
4.8 RVE loaded along the 2-direction and subsequent law [116]. 71
4.9 Possible mesh densities for the composite RVE [116]. 72
4.10 Energy dissipation as function of element size [120] 73

5.1 Local model of the stiffener with ply orientations. 78
5.2 Ply stack definition. 79
5.3 Smooth step implemented for the boundary conditions 80
5.4 Boundary conditions implemented. 80
5.5 3D local model. 81
5.6 Sub-modelling boundary conditions. 82
5.7 Final global-local models. 82

6.1 Deformation overview of the static model. 84
6.2 Normal stress along the x-axis distribution of the static model. . . . 85
6.3 Load-displacement curves of global analysis for debonded panel D1 with comparison to experimental and numerical results extracted from literature [89]. 86
6.4 Magnitude displacement field. 87
6.5 Deformation overview the local validation model along directions. . . 88
6.6 Stess distribution in the local model. 89
6.7 S11 distribution focus on the interface region. 89
6.8 Load-displacement curves of the local analysis for debonded panel D1 with comparison to experimental and numerical results extracted from literature [89]. 90
6.9 Delamination evolution at distinct displacements. 91
6.10 Displacement relation between the global and local models along the y-axis direction. 92
6.11 Quadratic stress criteria evolution. 93
6.12 Final delamination plot at $t = 27.60s$. 93

7.1 Wing planform of the wing-box in study. 97
7.2 Cross-section geometry of the ribs. 98
7.3 Spar geometry. 98
7.4 Geometry of the flanges: (a) Stringer, (b) Main front spar (L1), (c) Secondary rear spar (L2). 98
7.5 Approximation of the wing as a beam. 100
7.6 Equivalent boundary conditions for the wing-box. 100
7.7 Concentrated forces in the rib section. 101
7.8 Position of the distributed shear force components for each rib. . . . 102
7.9 Load regions along the wing span. 102
7.10 Wing regions along the wing span for load estimation. 103
7.11 Methodology for determining the horizontal shear force applied in each rib for load case 1. 103
7.12 Methodology for determining the horizontal shear force applied in each rib for load case 2. 104

7.13 Resulting loads on the wing tip for load case 1. 105
7.14 Resulting loads on the wing tip for load case 2. 105
7.15 Coupling constraint for the wing tip loads. 106
7.16 Boundary conditions and loads applied in the wing-box: (a) load case 1 (b) load case 2. 108
7.17 Mesh. 109
7.18 Structured mesh in the lower panel around the inspection hole. . . . 110
7.19 Structured mesh in the partition around the central hole in rib N2. . 110
7.20 First local model. 112
7.21 Mesh. 112

8.1 Results for the global wing-box analysis. 114
8.2 Displacement evolution in the wing-box global-local model. 115
116figure.caption.129
9.1 Mesh stress concentrations. 120
9.2 Resultant of the stress concentration. 120
9.3 Resultant of the stress concentration in the local wing-box skin. . . . 121

A.1 Magnitude displacement field. 142
A.2 Displacement field along the x-axis direction. 143
A.3 Displacement field along the y-axis direction. 144
A.4 Displacement field along the z-axis direction. 145

List of Tables

2.1 Summary of regulations evolution history [28]. 21

3.1 Failure criteria for fibres under tension [57]. 30
3.2 Failure criteria for fibres under compression [57]. 31
3.3 Failure criteria for fibres under compression [57]. 31
3.4 Criteria for matrix failure under tension [57]. 32
3.5 Criteria for matrix failure under compression [57]. 33
3.6 Failure criteria for fibres in tension and compression [57]. 34
3.7 Failure criteria for delamination initiation [57]. 37
3.8 Failure criteria for delamination growth [57]. 37

4.1 Parameter definition for Damage Evolution [115]. 60
4.2 Damage Evolution in Abaqus [115]. 61

5.1 Dimension of the panel [mm] [98]. 75
5.2 Material properties for IM7/8552 carbon/epoxy unidirectional tape [98], [124]–[132]. 77
5.3 Material data for cohesive elements [89]. 78
5.4 Elastic filament material properties. 78

7.1 Thickness, t, of the main structural elements. 99
7.2 Shear forces acting on the modelled part of the wing-box for the load case 1. 104
7.3 Shear forces acting on the modelled part of the wing-box for the load case 2. 104
7.4 Resulting bending and torsional moments acting on the wing tip for load case 1. 106
7.5 Resulting bending and torsional moments acting on the wing tip for load case 2. 106
7.6 Forces for limit condition: load case 1. 107
7.7 Forces for ultimate condition: load case 1 [N]. 107
7.8 Forces for limit condition: load case 2. 107
7.9 Forces for ultimate condition: load case 2. 108
7.10 Moments for limit condition: load case 1. 108

7.11 Moments for ultimate condition: load case 1. 108
7.12 Moments for limit condition: load case 2. 108
7.13 Moments for ultimate condition: load case 2. 108
7.14 Types of elements per region. 109

List of Acronyms

AC	Advisory Circular
AFP	Automatic Fibre Placement
ASTM	American Society for Testing Materials
ATL	Automated Tape Laying
BBA	Building Block Approach
CAR	Civil Aeronautic Regulation
CCZM	Continuum Cohesive Zone Modelling
CFRP	Carbon Fibre-Reinforced Polymer
CZM	Cohesive Zone Modelling
DCB	Double Cantilever Beam
DCZM	Discrete Cohesive Zone Modelling
DD	Domain Decomposition
DT	Damage Tolerance
EASA	European Aviation Safety Agency
ENF	End-Notched Flexure
FAA	Federal Aviation Administration
FAR	Federal Aviation Regulation
FE	Finite Element
GFRP	Glass Fibre-Reinforced Polymer
ITs	Inspection Thresholds
JAR	Joint Aviation Requirement
LL	Limit Load

MMB	Mixed Mode Bending
MPD	Maintenance Planning Document
NDI	Non-Destructive Inspection
PMC	Polymer Matrix Composites
RIIs	Repeat Inspection Intervals
RTM	Resin Transfer Moulding
TP	Test Pyramid
UD	Unidirectional
UL	Ultimate Load
VC	Cruise Velocity
VCCT	Virtual Crack Closing Technique
XWB	eXtra Wide Body

Part I

Introduction

Chapter 1

Introduction

1.1 Problem Statement

The aerospace industry is constantly pushing towards the limits of engineering, constantly thriving to optimize every design and process, in order to assure the safest, most advanced product available. To achieve this, composite materials are gaining a large role in the industry, due to high strength and stiffness-to-weight ratios, allowing significant reduction in airframe weight, increasing fuel efficiency, and reducing pollution, acoustic emissions, as well as maintenance requirements and subsequent expenses. Moreover, by using composite materials, the opportunities are infinite, since a simple change in stack direction or ply-thickness could drastically influence the response of the whole structure.

The introduction of composite materials posed a substantial impact on the structural certification strategy for the fuselage, wings and fuel tanks. Being that metallic structures, such as titanium-aluminium alloys have been used for many years, their isotropic behaviour is well-known for every scenario an aircraft could encounter.

Thus, as commercial aircraft are, nowadays, the safest mode of transport, these new materials must be subjected to many levels of certification requirements, versing from assessing individual material properties, to extremely expensive component tests made on specific parts. This approach to certification, referred to as the Building Block approach (BBA), is present throughout the process of designing and producing aeroplanes.

Taking into account the expensive design, manufacturing, testing and certification processes, there is a progressive demand for reliable computational models, in order to increase knowledge and predict the behaviour of composite structures in all loading scenarios.

Nowadays, high-fidelity constitutive models for composite materials have been successfully implemented in several finite element frameworks and used to foresee complex damage mechanisms and failure propagation at coupon level. Despite their accurate prediction capabilities, these powerful tools cannot be directly used in more complex structures, i.e., the top of the aforementioned Building Block, due to enormous computational costs. Hence, a plausible approach arises that overcomes these limitations and creates a continuous flow of information from a global model of complex structures to more accurate and detail-rich high-fidelity models - the Global-Local Technique.

1.2 Background

The use of carbon fibre-reinforced composite polymers (CFRP) in aircraft structures has been growing in recent years, as aluminium airframes have been replaced with aforestated materials.

Furthermore, another key advantage of the usage of composite structures when compared to metallic components is the substitution of riveted and bolted joints for bonded joints. This is particularly interesting when connecting skin and subsequent stringers as it causes a more even stress distribution, largely improving fatigue behaviour and, thus, increasing service time of the component.

Nowadays, the industry requires more complex numerical models, capable of predicting damage initiation and propagation in composite materials that must account for any micro-structural mechanisms and their relation to material responses [1] and, ergo, focus more on progressive damage models [2]. As mentioned above, not only composite materials increase the difficulty of modelling more advanced aeronautical components. Bonded joints and the use of cohesive models increase exponentially the difficulty of computing such structures.

Experimental procedures along with fatigue and fracture mechanics evaluations are required to verify the structural stability of composite structures. The safe-life analysis, which ensures sufficient conditions throughout the system's operations, requires extensive testing, demanding large budgets and time spans. This highlights the absolute necessity to develop accurate numerical tools that are capable of predicting the mechanical response of composite material components.

Hence, the excessive necessity of testing during all stages of aircraft design - versing from design and mechanical development of the components, to certification and in-service inspection and consequent repairs - paired with computational advances

and constant improvements of numerical models for damage prediction emphasizes many exciting opportunities for the future of the aeronautical industry.

1.3 Objectives

This thesis seeks to expand the technological development of modelling and simulation techniques for more complex aeronautic structures. The emphasis is placed on using numerical approaches to determine an experimentally compliant model to validate the technique in order to later compute a more complex aeronautical structure.

The main objective of this dissertation is to develop an one-way global-local technique which provides accurate and reliable resources whilst lowering immensely computational costs. Furthermore, as composite materials are still very difficult to model via commercial software, an user-defined subroutine is introduced as a way to asses material damage. This major goal of this thesis is to then use this validated approach to a real aeronautical system under realistic load conditions. The ultimate objective of this project is to, therefore, use this methodology to skin-stringer connections and to interlaminar failure amongst these components.

Overall, the specific objectives include:

- a precise summary of the state-of-the-art in terms of both composite material applications in the aeronautic industry and numerical modelling of damage in composite laminates. The former is crucial in order to determine the current state of the industry and the motivation for incorporating intricate models to lower costs and assist certification procedures. Furthermore, we aim to examine the necessary damage processes, the significance of the chosen damage scale, the typical methods used in mesoscale modelling, and finally the tactics frequently applied in the numerical modelling of composite structures, such as the global-local technique.

- a detailed examination of the nuances of the herein composite damage model, including how to depict intra- and interlaminar damage.

- the development of a verified global-local method to apply to the aeronautical structure, ascertaining the computational expenses and improvements to prior techniques.

- specific focus on skin-stringer connections and consequent failure behaviour.

- the development of finite element models of an aircraft structure representative system as means to verify the application of different modelling methodologies.

- assessing the validity of the approach proposed in this study with respect to the damage model, modelling strategy and global-local variation utilised, comparing the results to experimental tests.
- evaluating the methodology developed for failure prediction of a civil aircraft wing-box under real load cases.

1.4 Thesis layout

The thesis begins with an introductory section that encompasses many key components. Firstly, it addresses the problem statement, clearly identifying the issue at hand. Secondly, it establishes the backdrop, providing relevant context and background information. Thirdly, it explains the objectives of the thesis, clearly stating the goals and intentions of the research. Lastly, it offers a concise preview of the thesis layout, providing a quick overview of the organisation and structure of the document.

In chapter 2, we explore the use of composite materials in the field of aeronautics. This section examines the significant role that composites play in aircraft constructions, the process of materials certification, and the regulatory framework that influences the aerospace sector. Furthermore, this journey progresses to chapter 3, where modelling tools and the respective background is presented and succinctly defined.

Advancing to chapter 4, a comprehensive analysis of cohesive zone models, continuum damage mechanics, and intralaminar damage modes, providing valuable understanding of the fundamental modelling methodologies used is depicted, being the first step towards the validation of the model.

Thus, we proceed to the numerical analysis of a skin-stringer interface, which is depicted in chapter 5. Here, a thorough investigation into material properties and experimental data is made, prior to the establishment and definition of both the global and local models. After carefully explaining every nuance of the aforestated models, chapter 6 offers the findings of the study, which include global and local analysis results. These results include displacement fields, stress distributions, reaction forces, and delamination analyses. Together, these findings offer a thorough understanding of the research conclusions.

After validating the technique, we developed a more realistic case depicted in terms of a wing-box structure. Herein, in Part IV, an introductory overview of the finite element model used for the study of a wing-box structure is shown in chapter 7. The discussion covers the key aspects of the model, such as its geometric representation, the prescribed boundary conditions, and the applied loading conditions. This comprehensive presentation serves as a foundation for the future analysis and investigation. Furthermore, we advance into chapter 8, where the findings of the

wing-box analysis are presented, including both global and local outcomes. These results provide significant insights into the performance of composite materials inside intricate structural configurations.

Finally, Part V is developed. This Section begins with a critical evaluation of the limits and restrictions of the research, providing a clear understanding of the study's boundaries, depicted in chapter 9. We conclude this project by providing a concise summary of the research results, presenting the derived conclusions, and proposing prospective avenues for future research. In chapter 10, an emphasis on the importance and consequences of the study within the aerospace sector, specifically in relation to carbon fibre reinforced polymers is presented, culminating in important conclusions developed throughout this study and finally, potential new approaches that should be made to complement this study.

Part II

State-of-art and literature review

Chapter 2

Composite materials in the aeronautical industry

In this chapter, we delve into the introduction and escalating improvements of composite materials in the aeronautical engineering. We commence with exploring how these materials offer exceptional properties, driving innovation in aircraft design ever since after the Second World War, which lead to the aeroplanes that cross our skies every day. We further advance to the certification procedures that assure the marvellous safety and reliability of aircrafts in the modern era.

2.1 Composite Structures in Aircrafts

The aeronautical industry is constantly growing and pushing the engineering limits, striving towards new improvements. As many innovative systems, the use of composite materials began in the 1940s, propelled by the military industry after the Second World War, by the introduction of glass fibre-reinforced polymers (GFRPs). Likewise, sandwich-type honeycomb structures and glass fibre-reinforced composites were also introduced to the aviation industry in the 1940s [3]. In 1943, the United States Air Force, mandated exploratory projects that focused on building structural parts for military aircraft. These initiatives culminated in the Vultee BT, which presented a GFRP fuselage with the face material using both a glass-fabric honeycomb and a balsa core [4]. Nonetheless, these practical applications of the material

quickly highlighted technical constraints that limited the functions and demanded additional testing [5].

Advancing to the 1960s, composite materials consisting of boron-based fibres impregnated with distinct polymers were implemented in aerospace structures. These materials evolved into the present-day carbon fibre composites, referred to as CFRP (carbon fibre-reinforced polymers) or even PMC (polymer matrix composites) [6] and terminated their usage due to the development of graphite fibres, which made the initial boron-based materials obsolete, as a result of high costs and production challenges of the latter [5]. By the late 1960s, the aviation community turned its complete focus to carbon fibre-reinforced polymers, which were applied, on a demonstration basis, to military aircraft, particularly, to trim tabs, spoilers and doors [7].

At the beginning of the 1980s, it was clear that composite materials were extremely attractive, causing the shift from conventional isotropic materials to composites, due to their enhanced mechanical properties:

- Overall exceptional specific properties [6], particularly, stiffness and strength-to-weight ratios [8], which result in significant weight reductions, varying from 10% up to 30%, yielding substantial fuel savings and consequent decrease in carbon dioxide emissions, as well as improvements in payload capacity and flight range [1], [9]–[11].

- Improved fatigue resistance, expanding the lifetime of a specific component or entire system, which lower costs for airlines and, thus, make the product more desirable [9]–[11].

- Remarkable corrosion resistance, lowering the number of required inspections and decreasing maintenance costs [9].

Furthermore, composite materials allow tailor made layups that can vary depending on the mechanical requirements of the component [6], as well as fewer rivets and joints, increasing aircraft reliability and decreasing vulnerability to fatigue fractures brought on by stress concentrations caused by such elements [11].

For aircraft manufacturers, whom main focus is to produce an attractive product to satisfy airlines, the great mechanical properties paired with the lighter-weight made composite materials exquisite replacements for the typical aluminium/titanium alloys. Nonetheless, the manufacturing methods necessary to create large-scale composite structures have been one of the significant obstacles in the involvement of composite materials in commercial aircraft. The process of weaving, braiding, and epoxy injection is usually used to create composite materials, which can be time and money-consuming [12].

Albeit, as production technology has developed, processes like Automatic Fibre Placement (AFP) and Resin Transfer Moulding (RTM) have made it simpler and

faster to create composite structures, making the material more appealing commercial aircraft manufacturers. This increase in applications can be highlighted by the rise in percentage of total structural weight attributed to composites, as observed in Figure 2.1 [13].

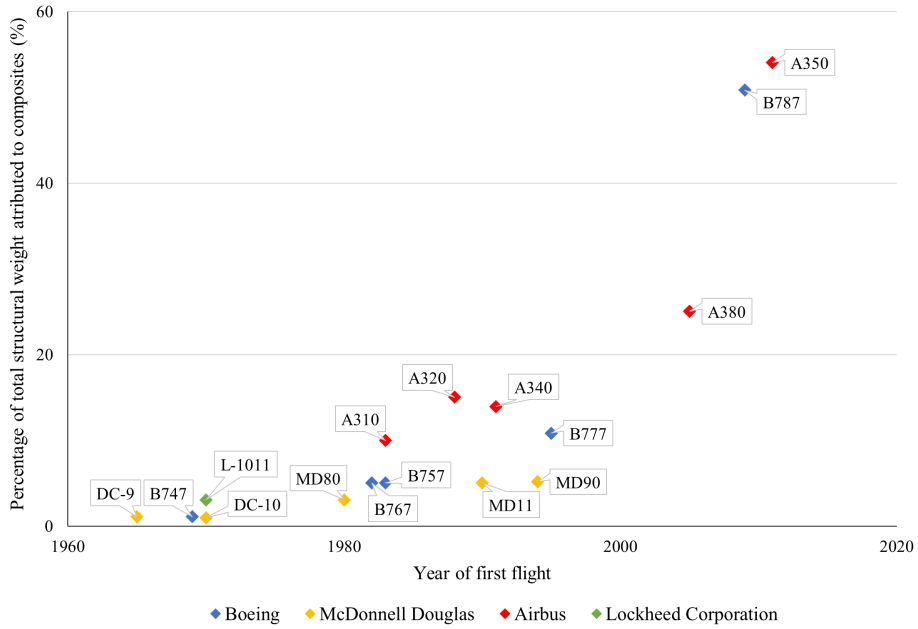


Figure 2.1: Percentage of total structural weight attributed to composites and the use of composites [14], [15].

Ergo, as it can be observed above, composite materials contribute over 50% of the structural mass of well-known commercial aircraft, such as the Boeing 787 and the Airbus 350XWB [16]. This highlights how the industry has evolved towards composite materials, mainly CFRPs.

Analysing two distinct aircraft from the French manufacturer Airbus, the famous A380, "The King of the Skies", and the aforementioned A350XWB - eXtra Wide Body - , many components are made of carbon fibre-reinforced polymers. Firstly, the A380 was the first ever commercial aircraft with a CFRP central wing box, which, due to the enormous size of the component, justified the intensive use of Automated Tape Laying (ATL) technology. In addition, the upper deck floor beams and rear pressure bulkhead are also made of CFRP [14].

Secondly, the Airbus 350XWB, the long-haul future. This aircraft, due to its design and materials, seriously surpassed the competition, i.e., the Boeing 787 Dreamliner, much of this due to the use of composite materials and recent technology to produce the components. This aircraft shows carbon fibre-reinforced polymers in many of the components that have no corrosion and high fatigue loads, meaning that the wings, centre wing box and keel beam, skin panels, frames, stringers and

doors (passenger & cargo) are all made of CFRP, resulting in a light airframe with 53% composites.

Moreover, the usage of composite materials does not only impact the weight and strength of the structure but also brings many benefits in terms of maintenance costs. When compared to the A380, this airplane requires 50% fewer structure maintenance tasks, and the threshold for the airframe is 12 years compared to eight for the A380 [17]. Another aspect that allows fewer production costs and optimal safety is the introduction of an ultrasonic inspection tool defined as "Percephone", implemented solely due to the use of composite materials. This system allows the operators to check for delamination in the composite plies, using ultrasonic inspection through previously drilled holes in the fuselage [18].

All in all, this section highlights the importance composite materials have been gaining in the aeronautical industry and emphasizes how vital is to search and implement new techniques to optimize this constantly growing process.

2.2 Aircraft Materials Certification

Contrary to metals, which are defined by their isotropic behaviour,i.e., their mechanical properties are independent of the orientation and do not vary with the direction, composite materials show an anisotropic behaviour that has no plane or axes of material symmetry [19]. Hence, when these materials were introduced to aeronautical structures, certification procedures for metallic airframes could no longer be used and new regulations were implemented [20].

In order to approve composite structures in the airframe of commercial aircraft and assure the safety of the aeronautical sector, companies must adhere to strict certification procedures that are laid out by regulatory organisations like the European Aviation Safety Agency (EASA) in Europe and the Federal Aviation Administration (FAA) in the United States of America.

To ensure that the aircraft will pass the qualification and certification processes, design allowables are created with the help of testing the performance of materials and components. Sufficient component, subcomponent, element, or coupon tests are necessary, further increasing the trial load. Therefore, it would be advantageous to shorten these tests by comprehending fatigue and fracture mechanisms, and damage tolerances [21].

Both safe-life and fail-safe designs must be taken into account so that fatigue assessment takes into account the structural resistance to fracture initiation and fatigue damage growth until catastrophic failure [21].

Variable amplitude fatigue ranges must be assessed from in-service structures, which could consist of many turning points that cause enormous test times and expenses - Figure 2.2 [22].

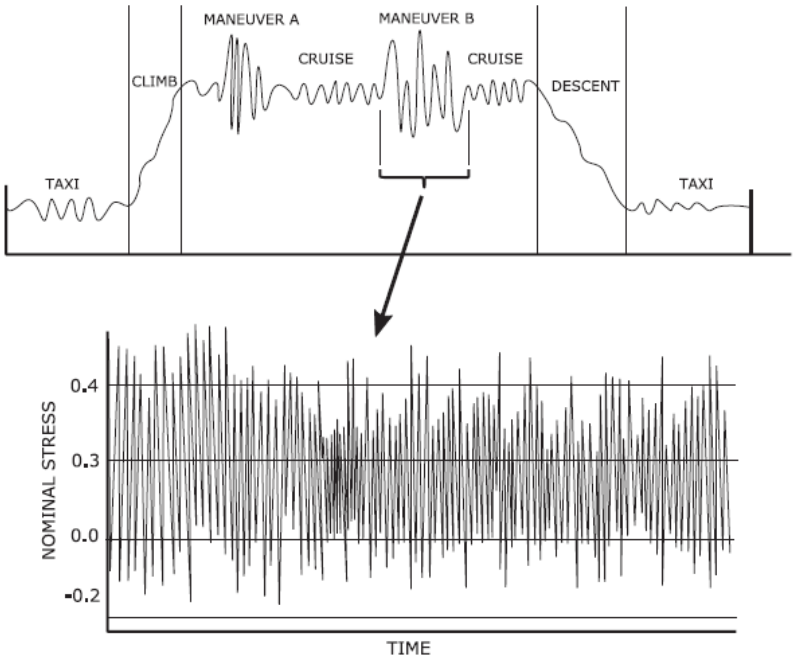


Figure 2.2: Mission profile and consequent stress spectrum [23].

2.2.1 Approaches and criteria for aircraft design

One of the key aspects that assures the safety of commercial aircraft is the comprehensive regulations to maintain airworthiness and continued airworthiness, that applies to design, manufacturing process, operations and maintenance [24]–[28].

Ergo, prior to the description of the various design philosophies, it is crucial to establish the definition of airworthiness. This can be encountered in an Italian RAI-ENAC Technical Regulations text: "*For an aircraft, or aircraft part, (airworthiness) is the possession of the necessary requirements for flying in safe conditions, within allowable limits*" [29]. Furthermore, it is important to define three key aspects of the aforementioned definition, i.e., safe conditions, possession of necessary requirements and allowable limits.

1. **Safe conditions**: this is related to the normal course and safe conclusion of the flight [29].

2. **Possession of necessary requirements**: this implies that every system of the aircraft is designed in accordance to the tested criteria, in order to fly in the safest conditions, as mentioned previously. Here, the regulations pose a pivotal aspect, as they establish the standards for design requirements, versing from structural strength to flight requirements, criteria for optimal design practice, systems, fatigue and flutter response, mandatory tests and maintenance operations, among many others [29].

3. **Allowable limits**: aircraft must establish a flight envelope, depending on the velocity and structural load factors. The operational conditions, like the day-visual flight rule, night flight, in or out flight of icing conditions are established.

   Examples of the significance of flying within the permitted limitations include overweight take-offs, aerobatic movements conducted with aircraft designed with load factors for non-acrobatic operations, flights without adequate protection under icing conditions, and breaching speed restrictions [29].

Since many airframe issues arise from fatigue-related problems, it is crucial to determine the Damage Tolerance (DT) philosophy, so that structures must be constructed with gradual crack propagation in mind, as well as fail-safe support provided by crack arrests or multiple load paths [28]. Figure 2.3 illustrates distinct design philosophies applied to every civilian aircraft.

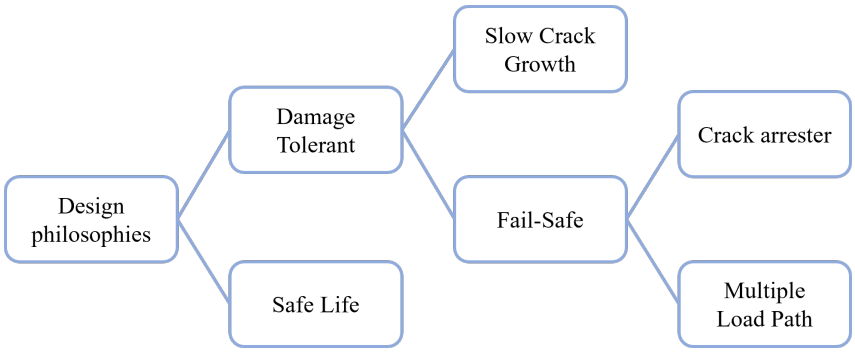


Figure 2.3: Durability and Damage Tolerance design routines for airframe structures [27], [30].

Damage Tolerant

Structures that can survive the impacts of damage or cracks that may appear throughout the service life are those that have been designed with damage tolerance in mind. Predicting the development of fractures or other damage in the structure and, thus, designing it to be able to endure those impacts without catastrophic collapse are corner stones of damage tolerance designs.

Thus, the FAA [31] defines this requirement as: "*Damage tolerance is the attribute of the structure that permits it to retain its required residual strength for a period of use after the structure has sustained a given level of fatigue, corrosion, accidental, or discrete source damage.*"

The DT design philosophies allow cracks to appear while the system is being used, but every damage must be found and fixed in accordance with the specifications laid out in the Maintenance Planning Document (MPD), which must be verified by numerous tests and approved by authorities as part of the type certification processes. The main components of an MPD are the Inspection Thresholds (ITs)

and Repeat Inspection Intervals (RIIs), which correspond to preset Non-Destructive Inspection (NDI) procedures [28].

The objective of this fatigue design tool is to forecast how long it will take a crack to expand from its presumed beginning size to its critical size in the component. Cracks in a damage-tolerant structure are seen as a preexisting condition. Then, inspection intervals are established to keep an eye out for these cracks far before it is anticipated that they may become serious [32].

The design principles for damage tolerance in composite materials diverge notably from those applicable to conventional metallic parts, owing to the distinctive attributes and behaviour shown by composites. Due to their anisotropic qualities, whereby their mechanical characteristics display variation in accordance with the direction, the behaviour of composites is contingent upon the orientation of the fibres embedded inside the matrix. Therefore, the design of composites with high damage tolerance requires a meticulous examination of the impact of damage on several properties, including strength, stiffness, and fracture toughness in different orientations.

Moreover, the process of identifying and evaluating damage in composite materials is inherently more intricate compared to that of metals. The presence of internal damage, such as delamination or fibre breaking, may not be immediately apparent and may need the use of sophisticated non-destructive testing (NDT) methods, such as ultrasonic inspections and thermography. Furthermore, the repair protocols for composite materials exhibit unique characteristics, which include the application of composite materials to patch regions that have been damaged, while also assuring appropriate curing and alignment. The complicated nature of material behaviour, damage detection, and repair processes necessitates a specialised and detailed examination of damage-tolerant design in composite materials. This area of research requires deep comprehension of composite mechanics and fracture behaviour.

Safe-life Design

In 1952, the famous Havilland Comet initiated its jet commercial services, rising to the top of the competition just to decline two years later, when two distinct aircraft disintegrated during a flight just three months apart. This infamous catastrophe is, actually, one of the most impacting in the aeronautical industry, since it was caused by cracks on the countersunk fastener holes adjacent to severe radii corners at windows and escape hatches [33] and lead to changing the design of the windows to rounded shapes, in order to avoid severe stress concentrations in the corners.

Past definitions stated that safe-life meant that without visible fractures, the structure has been assessed to be able to sustain the repeated loads of varying magnitude predicted over its service life [32]. Nonetheless, according to the FAA [34], this definition was changed to imply "that number of events, such as flights,

landings, or flight hours, during which there is a low probability that the strength will degrade below its design ultimate value due to fatigue cracking."

Fail-safe Design

Specifying, the fail-safe design, referred to as Safety by Design, is based on a design idea with a sufficient life duration without fatigue damage. Despite this, devices with multiple load paths should be designed and be inspectable in service [28]. This results in a system that is fully prepared for failure, meaning that redundant systems are implemented to avoid catastrophic failure.

According to the fail-safe design philosophy, redundant load pathways should be offered as fall-backs in the event of localised failure. The following is the recognised FAA definition [31]: "*Fail safe is the attribute of the structure that permits it to retain its required residual strength for a period of unrepaired use after the failure or partial failure of a principal structural element*".

2.2.2 Regulations

Firstly, the main composite properties that forced tailor-made composite certification procedures are [20]:

- Environmental sensitivity, i.e., temperature and humidity in which the aircraft operates. This is particularly relevant for matrix-dominated properties, because of their organic nature.
- Better fatigue response than metals, particularly for thermoset matrices, meaning that the main issue is static strength requirements.
- Sensitivity to in-plane delamination - practical effects regarding the susceptibility to low-velocity accidental impact damage and induced out-of-plane secondary loads in complex build-up structures.
- Structural properties are not process dependent, highlighting consequences on material qualification procedures and quality requirements.
- Poor electrical connectivity, causing severe problems for lighting certification procedures.

The factors above resulted in changes and new regulations that maintained commercial aircraft as the safest most reliable mean of transportation. Thus, after highlighting the necessary concepts, it is crucial to analyse any important regulation for composite materials in aircraft structures.

To begin with, the first guidance paper released by the Federal Aviation Administration, focused on the early composite structural applications - such as the Boeing

737 horizontal stabiliser and the DC10 vertical fins was the AC 20-107 [35], published on the 7th of October of 1984. This regulation centred on the environmental sensitivity and the necessity of structural substantiation tests [20]. These guidelines were later updated to the Advisory Circular 20-107A [35], arising from discussions of both American and European experts [20].

Furthermore, the European version of the aforementioned guidelines was published on the 16th of June of 1986, named the JAR ACJ 25.603. This paper addressed the three key issues of the AC 20-107A [35].

At that time, the majority of composite aeroplane structures in Europe only had one material supplier approved, leading to a large number of industrial issues, the most serious of which is the complete dependence of the aircraft project on the dependability of the chosen supply.

It was required to construct a compliance philosophy to address this topic because the applicable AC's did not specifically address this issue. With so many material modification, substantiation programmes that required approval as part of the A320 post-certification activities arose. This proved to be a remarkable opportunity for the Airbus partners and the European airworthiness authorities involved to coordinate their efforts.

This evolution arrived at one of the most important aspects of composite materials in the aeronautical industry, i.e., their introduction to the Building Block approach to design. Hence, only after the component has been treated (or at least the resin has had time to cure), can composite materials develop their mechanical characteristics. These characteristics must be examined using specimens that are representative of all the important aspects of the structure's design since they are procedure dependent and pose the primary objective of the building block approach (BBA) and its related test pyramid (TP), as shown of Figure 2.4, was proposed in the 1970s [36].

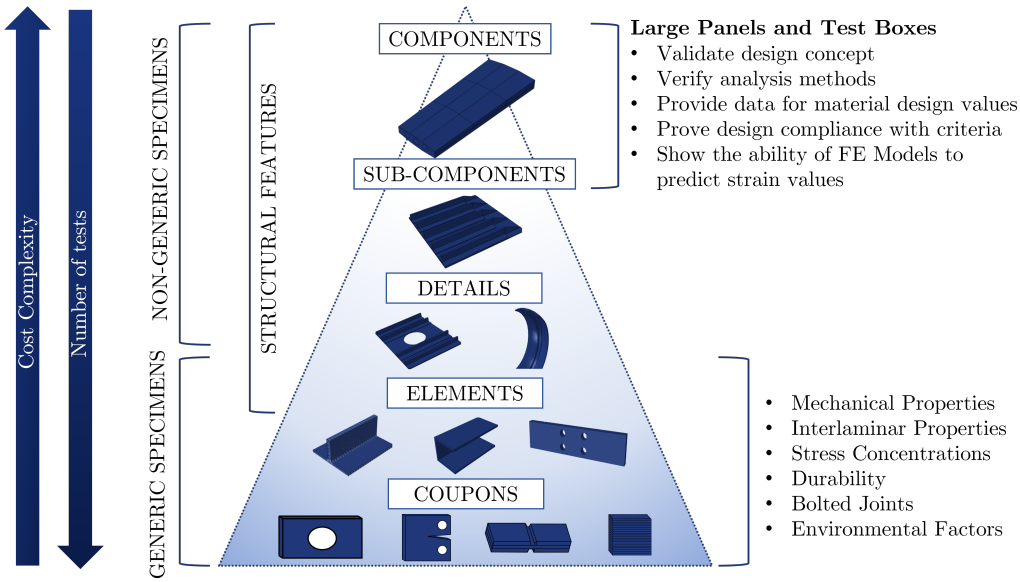


Figure 2.4: Building block approach to certification [20], [37].

Before taking a closer look into more specific composite regulations, Table 2.1 shows a brief summary of the evolution history of aircraft regulations.

Table 2.1: Summary of regulations evolution history [28].

Period	Regulation	Evolution Stories
1949	CAR 4b.316	Implemented fatigue strength in aircraft designs (based on safety by retirement).
1954	HavillandD.H.106	Full-scale fatigue tests should be detached from static tests.
1956	CAR 4b.270	Introduced fail-safe option, and test validation requirements to the safety by design concept.
1958	B-47	Fatigue analysis cannot solely assure aircraft safety-design loads should be proximate to real operations.
1958-1969	ASIP & series Doc.	Incorporated ASIP for military aircraft, to ascertain fatigue life with full-scale fatigue tests.
1964	14 CFR 25.571	CAR 4b.270 was rectified to 14 CFR 25.571 without major alterations.
1968	ASD-TR-66-57	Necessary tests for 1) Materials; 2) Machining processes; 3) Joints to final assemblies.
1970	F-5	It is necessary to balance designs for static and fatigue. introduced cold working as a way to increase tiredness.
1966-1977	KC-135	Static and fatigue designs must be balanced, and material selection is crucial.
1972	MIL-SID-1530	Validation tests for coupons, junctions, components, structural operating mechanisms and control systems were necessary for ASIP.
1978	Amdt.25-45AC 25.571-1	Increased Damage Tolerance Requirements for every civil aircraft, including in-service fleets.
1986	AC 25.571-1A	Taken into account separate source damages.
1997	AC 25.571-1 B	Instituted the concept of scatter factors in certification.
1998	Amdt.25-96/AC 25.571-1C	Required test validations for No WFD appeared before DSG for civil aircraft.
2004	MIL-STD-1530B	Superseded MIL-HDBK1530B, in which the required items for corrosion were included.
2005	MIL-STD-1530C	Risk analysis was included into ASIP and a link to airworthiness certification was made.
2010	Amdt.25-132/AC 25.571-1D	Establish LOV validation standards for civil aircraft that are applicable to all currently operating aircraft.
2016	MIL-STD-1530D	Adding criteria for composite, cost-effective service life, and NDI method capabilities.

FAR-25 [38] and CS-25 papers [39] are mandatory standards that the FAA and

EASA have released to set design requirements. The FAR-25 [38] includes the fundamental rules, whereas Advisory Circulars (ACs) contain additional information. The certification specifications included in the CS-25 1 are common technical interpretations of the fundamental airworthiness criteria. The book is divided into sections, with sections B (Flight), C (Structure), and D (Design and Construction) being the most crucial with regard to loads and aeroelasticity.

Finally, versing into the composite airframe regulations, it is important to highlight:

Part 23 - Airworthiness Standard: Normal, Utility. Acrobatic, and Commuter Category Airplanes.

23.573 Damage tolerance and fatigue evaluation of structure

Composite airframes must be evaluated under this section, instead of 23.571 and 23.572. The composite airframe structure, the failure of which would result in catastrophic loss of the airplane, in each wing including canards, tandem wings, and winglets), empennage, their carry through and attaching structure, movable control surfaces and their attaching structure fuselage, and pressure cabin using the damage tolerance criteria prescribed in the following paragraphs [40], [41]:

(a1) The ability of the structure to carry the maximum load with damage up to the level of detectability taking into account the inspection processes used must be shown by testing or analysis backed by tests.

(a2) Testing, or analysis backed by testing, are required to determine the growth rate or absence of growth of damage that may result from fatigue, corrosion, manufacturing faults, or impact damage under repeated loads anticipated in service.

(a3) The ability to endure critical limit flight loads, also known as ultimate loads, must be demonstrated by residual strength tests, or analysis supported by residual strength tests, with the level of observable damage being compatible with the findings of damage tolerance evaluations. The presented loads for pressurised cabins must be able to withstand:

- **(i)** Critical limit flight loads when normal operating pressure and anticipated external aerodynamic pressures are combined.
- **(ii)** Predicted aerodynamic pressures in a 1 g flight paired with a cabin differential pressure equal to 1.1 times the normal operating differential pressure without any other load.

(a4) The development of an inspection programme appropriate for usage, by operation and maintenance staff, must take into account the damage growth between initial detectability and the value chosen for residual strength demonstrations.

(a5) Any bonded joint whose failure would cause the catastrophic loss of the aircraft must have its maximum load capacity supported by one of the following techniques:

(i) The maximum disbonds of each bonded joint necessary to meet the requirements of paragraph (c) of this section must be established by analysis, testing, or a combination of the two. Design elements must be used to avoid disbonds of each bonded joint that are bigger than this;

(ii) Each production unit that will subject each critical bonded joint to the critical limit design load must undergo proof testing;

(iii) Techniques for nondestructive examination that guarantee the sturdiness of each joint must be devised, and they must be repeatable and dependable.

Part 25 - Airworthiness Standard: Transport Category Airplanes.

25.571 Damage tolerance and fatigue evaluation of structure.

(a1) General. An evaluation of the strength, detail design, and fabrication should prove that catastrophic failure due to fatigue, corrosion, or accidental damage, will be avoided throughout the aircraft's operational life. Advisory Circular AC No. 25.571-1 contains guidance information relating to the requirements of this section.

(b) The examination must include a determination of the likely sites and types of wear and tear brought on by corrosion, fatigue, or unintentional damage. Analysis backed by test findings and (where available) service experience must be used to make the decision. Where the design is such that this sort of damage may be predicted to occur, damage at many places resulting from past fatigue exposure must be taken into account. The evaluation must include static and repetitive load evaluations that are backed by test data. At any point during the operating life, the degree of damage must be consistent with the initial detectability and subsequent increase under repeated loads. The examination of residual strength must demonstrate that the remaining structure can sustain the following loads, which are referred to as static ultimate loads, that correspond to the following conditions:

- Limit symmetrical manoeuvring conditions - specified in 25.337 at Cruise Velocity (VC) and in 25.345.

- Limit gust conditions - shown in 25.341 at the specified speeds up to VC and in 25.345.
- Limit rolling conditions - detailed in 25.349.
- Limit unsymmetrical conditions - stated in 25.367 and 25.427, at speeds up to VC.
- Limit yaw manoeuvring conditions - described in 25.351 at the specified speeds up to VC.

Long-term flight of composite structures is permitted with residual strength slightly exceeding Limit Loads. Regardless of how resistant a composite structure is to damage progression, damage that reduces residual strength below Ultimate Load must be located and corrected right away by setting a reasonable inspection interval in order to reach standards of safety comparable to or greater than metal practises, as shown on Figure 2.5.

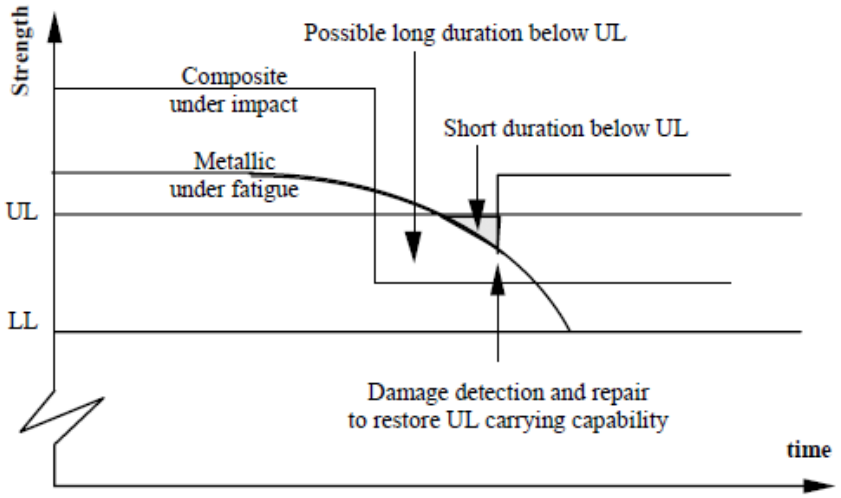


Figure 2.5: Metal fatigue crack damage and non-growing damage in composite materials (Ultimate Load (UL) and Limit Load (Limit Load)) [37].

Furthermore, focusing now on bonded joints in civilian aicrafts, the requirements are present of the aforestated regulations and are extensively discussed within Federal Aviation Administration Advisory Circular AC20-107B [42], albeit they can be summarised as follows [43]:

- It is crucial to maintain the adhesive bond strength and durability within the working environment.
- The repair must be able to withstand the maximum load while exhibiting damage that is just barely detectable.

- The repair procedure should be able to withstand the maximum load that it is designed for, even if there is visible damage such as impact damage or the progression of pre-existing damage due to fatigue.
- The pace of increase of damage from threshold levels to the extent of damage used for the assessment of residual strength must be such that it facilitates the establishment of an inspection programme.

Whilst rules allow for fatigue-induced damage development, composite or bonded structures have often been constructed based on a "no growth" condition, as guided by FAA AC20-107A [35], [44]. The reason for this may be attributed to a lack of comprehensive knowledge on fatigue damage in composites and bonded joints, particularly when compared to metals. Additionally, there is a dearth of proven analytical techniques for predicting fracture propagation in these materials. The most recent iteration of this circular (AC20-107B) addresses a more intricate methodology for validating tiredness, including some provisions for restricted instances of sluggish or halted development [43].

However, the overarching issues outlined in reference [44] persist. In order to meet the aforementioned criteria, adherence must be validated using established methods, namely via the use of "testing" or "analysis," bolstered by evidence. In the context of a repair, which is typically an isolated event, it is advantageous to validate the design through analysis techniques that have been verified on generic and representative repairs. This validation should involve the use of material properties that have been substantiated through tests conducted on representative coupons and elements, for both the repair materials and the parent materials involved. This serves as further incentive to implement standardisation measures for maintenance materials within the aerospace sector, in addition to other advantages such as enhanced accessibility and supply.

The major aircraft structure's essential certification criteria for bonded repair may be succinctly defined as follows [43]:

1. Initial and long-term integrity of the adhesive bondline must be guaranteed.
2. Structural performance standards are met and supported by evidence.

Chapter 3

Numerical modelling of damage in composite materials

In the present chapter, we explore failure mechanisms of CFRPs, focusing in their definition and potential Finite Element Modelling applications. Lastly, we introduce how to model such materials into Abaqus and, finally, a noteworthy methodology for modelling complex parts is shown- the Global-Local technique, reviewing the literature to prove the benefits of these methodology

3.1 Composite Failure Mechanisms

Macroscopic fracture/failure in CFRP components are complex and can be influenced by several factors, such as fibre orientation, loading conditions, and material properties, highlighting the challenges inherent to the development of failure models that account for multiple mechanisms. Ergo, preceding total rupture, these materials demonstrate local failures at lower length-scales - discrete damage events-, for instance: fibre breakage, pullout or kinking/buckling -fibre-dominated modes-, matrix cracking and fibre/matrix de-bonding -matrix dominated modes-, and delamination between plies - detachment between two adjoining layers-, that grow and accumulate - damage evolution- throughout the loading process [1], [45]–[49].

Fibre fracture, matrix cracks and delamination may be divided into intralaminar and interlaminar damage. The first refers to the many underlying micro-mechanical

failure mechanisms (such as fibre fracture/buckling, matrix cracking, fibre/matrix de-bonding and pull-out), and the second to the inter-facial separation between plies [1], [45]–[49].

Furthermore, to better understand the following sections, in failure criteria, the σ, τ, ϵ and γ are the stress and strain in the normal and shear directions whilst X, Y, Z and S are strengths in the fibre, matrix, through-thickness and shear directions. Subscripts 1,2 and 3 are related to the fibre, transverse and through-thickness directions; T and C are for values in tension and compression, respectively, and "is" refers to *in-situ* strengths.

The latter relates to the fact that a ply embedded within a multidirectional laminate has increased transverse and tensile strengths, as proven experimentally [50].

3.1.1 Fibre and Matrix failure

In composite materials, the aggregation of individual fibre failures inside plies causes fibre failure in tension as there are not sufficient intact fibres to support the required loads. This can be visualised in Figure 3.1.

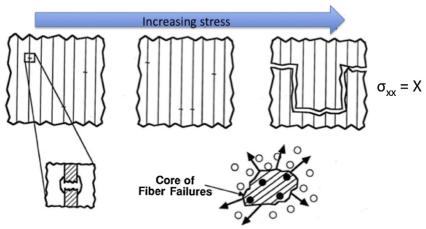


Figure 3.1: Fibre failure evolution in an UD composite under axial tension [51].

One of the first attempts at a failure theory for composites was published by Azzi and Tsai [52], developing their work from Hill's theory for yielding and plastic flow of anisotropic metals [53]. Hill derived a generalized isotropic yield criterion, arriving at the presented equation Equation 3.1.

$$F\left(\sigma_{yy}-\sigma_{zz}\right)^2+G\left(\sigma_{zz}-\sigma_{xx}\right)^2+H\left(\sigma_{xx}-\sigma_{yy}\right)^2+2\left(L\tau_{yz}^2+M\tau_{zx}^2 +N\tau_{xy}^2\right)=1 \tag{3.1}$$

where F, G, H, L, M and N are material constants which represent direction-dependent yielding. Azzi and Tsai highlighted that, if the x-axis is aligned with the fibre direction in a unidirectional composite, the y-axis is the plane of isotropy and, therefore, the material is transversely isotropic [51]. As the plies in a lamina are thin, by defining the z-axis in the thickness direction, it is possible to neglect the stress components σ_{zz}, τ_{zx} and τ_{zy} and, by adapting Equation 3.1 according to the

aforementioned considerations and by mathematical manipulation, they arrived at Equation 3.2, i.e., the Tsai-Hill failure criteria.

$$\frac{\sigma_{xx}^2}{X^2} + \frac{\sigma_{yy}^2}{Y^2} - \frac{\sigma_{xx}\sigma_{yy}}{X^2} + \frac{\tau_{xy}^2}{T^2} = 1 \tag{3.2}$$

The above equation shows that failure can only occur when linear elastic response of any combination of stress components - σ_{xx}, σ_{yy} and τ_{xy} - reaches the limit condition. Ergo, the failure modes expressed by the aforestated criteria are:

- Tension/compression failure in the fibre direction, when $\sigma_{xx} = X$.
- Tension/compression normal to the fibre, when $\sigma_{yy} = Y$.
- Shear failure on the $x - y$ plane, when $\tau_{xy} = T$.

One relevant aspect of this criterion is that at $\sigma_{xx} = X$ failure happens at a single point, meaning that the ply loses its respective carrying capacity in the fibre direction. This means that failures starts at random points and propagates until the ultimate failure of the ply, depending on the location of the points, as showed on the above figure.

Advancing, another relevant failure theory was introduced in 1967 by Hoffman [54], in which he stated that all composite failure modes were brittle fracture, meaning that the linear elastic response in every stress component terminated at a limit value - fracture strength. The key distinction between this criteria and the former is that Azzi and Tsai's criterion allocated distinct strengths in tension and compression for each direction, normal or along the fibres.

Furthermore, in 1971 Tsai and Wu [55] established an accurate ellipsoidal representation of the failure surface by defining a scalar-valued function f of the stress tensor components related to the surface, as seen in Equation 3.3, in which F_{ij} and F_{ijjl} are the second and forth order strength tensors.

$$f(\sigma_{ij}) = F_{ij}\sigma_{ij} + F_{ijkl}\sigma_{ij}\sigma_{kl} = 1 \tag{3.3}$$

Finally, in 1980, Hashin [56] stated that failure representation in plane stress by a single ellipsoidal surface was not applicable to every scenario. Hashin defended that governing stress interactions must be represented by quadratic polynomials, as linear formulations proved insufficient. Thus, for plane stress conditions in an unidirectional composite, for $\sigma_1 > 0$, Hashin's criteria is:

$$\left(\frac{\sigma_1}{X}\right)^2 + \left(\frac{\sigma_6}{T}\right)^2 = 1 \tag{3.4}$$

Hashin postulated the existence of a failure plane that passed through the matrix (i.e., between fibres) for matrix failure modes, with the critical normal and shear

traction components on the plane dictating its inclination. Hence, since the tractions on the failure plane are expressed by tensor transformation, the failure function is as observed on Equation 3.5.

$$g\left(\sigma_{22}, \sigma_{33}, \sigma_{23}, \sigma_{12}, \sigma_{13}, \theta\right) = 1 \tag{3.5}$$

where θ is the angle of inclination between the transverse axis - x_2 and the plane's normal. Thus, for plane stress scenarios, Hashin arrived at the following equation for tensile matrix mode, i.e., $\sigma_2 > 0$:

$$\left(\frac{\sigma_1}{X_\mathrm{T}}\right)^2 + \left(\frac{\tau_{12}}{S_{12}}\right)^2 \geqslant 1 \tag{3.6}$$

Furthermore, different in-plane failure criteria for fibre failure under tension can be observed in Table 3.1.

Table 3.1: Failure criteria for fibres under tension [57].

Criteria	Equation
Fibre Max-stress	$\sigma_1 \geqslant X_\mathrm{T}$
Fibre Max-strain	$\varepsilon_1 \geqslant \varepsilon_{1_\mathrm{T}}$
Hashin-3D (1980) [56]	$\left(\frac{\sigma_1}{X_\mathrm{T}}\right)^2 + \frac{1}{S_{12}^2}\left(\tau_{12}^2 + \tau_{13}^2\right) \geqslant 1$
Hashin-2D (1980) [56]	$\left(\frac{\sigma_1}{X_\mathrm{T}}\right)^2 + \left(\frac{\tau_{12}}{S_{12}}\right)^2 \geqslant 1$
Chang-Chang (1987) [58]	$\sqrt{\left(\frac{\sigma_1}{X_\mathrm{T}}\right)^2 + \frac{\tau_{12}^2/2G_{12} + \frac{3}{4}\alpha\tau_{12}^4}{S_{12_\mathrm{is}}^2/2G_{12} + \frac{3}{4}\alpha S_{12_\mathrm{is}}^4}} \geqslant 1$
Puck (1998) [59]	$\frac{1}{\varepsilon_{1_\mathrm{T}}}\left(\varepsilon_1 + \frac{v_{\mathrm{f}12}}{E_{\mathrm{f}1}} m_{\mathrm{f}_\sigma} \sigma_2\right) \geqslant 1$

For compression scenarios, fibre failure occurs due to microbuckling and formation of kink bands. The former, is a more global failure model whilst the latter is initiated by local microstructural defects and is more common after testing [57], [60]. Table 3.2 shows several criteria for this type of failure.

Table 3.2: Failure criteria for fibres under compression [57].

Criteria	Equation
Fibre Max-stress	$\sigma_1 \geqslant X_{\mathrm{C}}$
Fibre Max-strain	$\varepsilon_1 \geqslant \varepsilon_{1_{\mathrm{C}}}$
Greszczuk (1974) [61]	$\sigma_1 \geqslant \frac{G_{12}^{\mathrm{m}}}{1-V_{\mathrm{f}}}$
Chang-Lessard(1991) [62]	$\sigma_1 \geqslant \bar{X}_{\mathrm{C}}$
Puck (1998) [59]	$\frac{1}{\varepsilon_{1\mathrm{c}}}\left\lvert\left(\varepsilon_1 + \frac{v_{\mathrm{f}12}}{E_{\mathrm{f}1}} m_{\mathrm{f}_\sigma} \sigma_2\right)\right\rvert \geqslant 1 - (10\gamma_{21})^2$
LaRC03 (2003) [50]	$\sigma_{22}^m < 0 : \left\langle \frac{\lvert\tau_{12}^m\rvert + \eta_{12}\sigma_{22}^m}{S_{12_{\mathrm{is}}}} \right\rangle \geqslant 1$
	$\sigma_{22}^m > 0 :$
	$(1-g)\left(\frac{\sigma_{22}^m}{Y_{T_{\mathrm{k}}}}\right) + g\left(\frac{\sigma_{22}^m}{Y_{T_{\mathrm{ks}}}}\right)^2 + \left(\frac{\tau_{12}^m}{S_{12\ \mathrm{s}}}\right)^2 \geqslant 1$
LaRC04 (2005) [63]	For $\sigma_{2m2m} < 0 : \frac{\lvert\tau_{1m2m}\rvert}{S_{12\ \mathrm{s}} - \eta_{12}\sigma_{2m2m}} \geqslant 1$
	For $\sigma_{2m2m} > 0 : (1-g)\left(\frac{\sigma_{2m2m}}{Y_{T_{\mathrm{is}}}}\right) +$
	$g\left(\frac{\sigma_{2m2m}}{Y_{T_{\mathrm{is}}}}\right)^2 + \frac{\Lambda_{23}^0 \tau_{2m3\varphi}^2 + \chi(\gamma_{1m2m})}{\chi\left(\gamma_{12_{\mathrm{i}}}^u\right)} \geqslant 1$
Maimí et al. (2007) [64]	$\langle\lvert\tau_{12}^m\rvert + \eta_{12}\sigma_{22}^m\rangle / S_{12} \geqslant 1$

Finally, for both tension and compression, Table 3.3 is presented.

Table 3.3: Failure criteria for fibres under compression [57].

Criteria	Equation
Lee (1982) [65]	$\sigma_1 \geqslant \sigma_{\mathrm{FN}}$ or $\sqrt{(\sigma_{12}^2 + \sigma_{13}^2)} \geqslant \sigma_{\mathrm{FS}}$
Christensen (1997) [66]	$\alpha_2 k_2 \sigma_1 + \frac{1}{4}(1+2\alpha_2)\sigma_1^2 - \frac{(1+\alpha_2)^2}{2}\frac{(\sigma_2+\sigma_3)}{2}\sigma_1 \leqslant$
	k_2^2
Huang et al. (2003) [67]	Use dissipated energy density $\phi(\varepsilon)$ to
	indicate damage: fibre failure for $\phi(\varepsilon) > D_t$,
	where D_t is the dissipated energy density
	threshold.

Furthermore, matrix failure is an extremely complex phenomenon, due to the fact that cracks start at defects or interfaces and culminate in a failure across a critical fracture plane [57]. Criteria for failure under tension assume the aforementioned plane in the transverse direction, depending on a interaction between in-plane shear stresses and the tensile normal. For composites in compression, contrary to under tension, the fracture plane is not assumed by every author in these criteria. Nevertheless, it is relevant to highlight that, despite the fact that matrix compression occurs in shear, the fracture plane commonly observed is $53^\circ \pm 2^\circ$ [57].

Thus, relevant criteria for matrix failure under tension is shown in Table 3.4, for compression in Table 3.5 and for the tension and compression in Table 3.6.

Table 3.4: Criteria for matrix failure under tension [57].

Criteria	Equation
Matrix Max-stress	$\sigma_2 \geqslant Y_\mathrm{T}$
Fibre Max-strain	$\varepsilon_2 \geqslant \varepsilon_{2_\mathrm{T}}$
Hashin-3D (1980) [56]	$\frac{(\sigma_2+\sigma_3)^2}{Y_\mathrm{T}^2} + \frac{\tau_{23}^2-\sigma_2\sigma_3}{S_{23}^2} + \frac{\tau_{12}^2-\tau_{13}^2}{S_{12}^2} \geqslant 1$
Chang-Chang (1987) [58]	$\sqrt{\left(\frac{\sigma_2}{Y_\mathrm{T}}\right)^2 + \frac{\tau_{12}^2/2G_{12}+\frac{3}{4}\alpha\tau_{12}^4}{S_{12_\mathrm{s}}^2/2G_{12}+\frac{3}{4}\alpha S_{12_\mathrm{s}}^4}} \geqslant 1$
Puck (1998) [59]	$\sqrt{(\tau_{21}/S_{21})^2 + \left(1-p_{\perp 1}^{(+)}Y_\mathrm{T}/S_{21}\right)^2(\sigma_2/Y_\mathrm{T})^2} + p_{11}^{(+)}\sigma_2/S_{21} \geqslant 1-\lvert\sigma_1/\sigma_{1\mathrm{D}}\rvert$
LaRC03 (2003) [50]	$(1-g)\left(\frac{\sigma_2}{Y_{\mathrm{T}_\mathrm{h}}}\right) + g\left(\frac{\sigma_2}{Y_{\mathrm{T}_\mathrm{k}}}\right)^2 + \left(\frac{\tau_{12}}{S_{12_\mathrm{h}}}\right)^2 \geqslant 1$
LaRC04 (2005) [63]	$(1-g)\left(\frac{\sigma_2}{Y_{\mathrm{T}_\mathrm{k}}}\right) + g\left(\frac{\sigma_2}{Y_{\mathrm{T}_\mathrm{k}}}\right)^2 + \frac{\Lambda_{23}^0\tau_{23}^2+\chi(\gamma_{12})}{\chi\left(\gamma_{12_\mathrm{h}}^{\mu}\right)} \geqslant 1$
Maimí et al. (2007) [64]	$\sigma_2 \geqslant 0$: $\sqrt{(1-g)\left(\frac{\sigma_2}{Y_\mathrm{T}}\right) + g\left(\frac{\sigma_2}{Y_\mathrm{T}}\right)^2 + \left(\frac{\tau_{12}}{S_{12}}\right)^2} \geqslant 1$ $\sigma_2 < 0$: $\langle\lvert\tau_{12}\rvert + \eta_{12}\sigma_2\rangle / S_{12} \geqslant 1$

Table 3.5: Criteria for matrix failure under compression [57].

Criteria	Equation
Matrix Max-stress	$\sigma_2 \geqslant Y_C$
Fibre Max-strain	$\varepsilon_2 \geqslant \varepsilon_{2_C}$
Hashin-2D (1980) [56]	$\sigma_2/Y_C \left[\left(Y_c/2S_{23}\right)^2 - 1\right] + \left(\sigma_2/2S_{23}\right)^2 +$ $\left(\tau_{12}/S_{12}\right)^2 \geqslant 1$
Chang-Lessard (1991) [62]	$\sqrt{\left(\sigma_2/Y_C\right)^2 + \frac{\tau_{12}^2/2G_{12}+\frac{3}{4}\alpha\tau_{12}^4}{S_{12\ s}^2/2G_{12}+\frac{3}{4}\alpha S_{12\ s}^4}} \geqslant 1$
Puck (1998) [59]	For 2D plane stress, Mode B, $\theta_{fp} = 0°$, $\frac{1}{S_{21}}\left(\sqrt{\tau_{21}^2 + \left(p_{\perp 1}^{(-)}\sigma_2\right)^2} + p_{\perp 1}^{(-)}\sigma_2\right) \geqslant 1 - \left\lvert\frac{\sigma_1}{\sigma_{1D}}\right\rvert$ for $\sigma_2 < 0$ and $0 \leqslant \lvert\sigma_2/\tau_{21}\rvert \leqslant R_{\perp\perp}^A/\lvert\tau_{21c}\rvert$
LaRC03 (2003) [50]	$\sigma_1 < Y_C : \tau_{23_{em}}^m/S_{23} + \tau_{12_{em}}^m/S_{12_{is}} \geqslant 1$ $\sigma_1 \geqslant Y_C : \tau_{23_{err}}/S_{23} + \tau_{12_{em}}/S_{12_s} \geqslant 1$ $\tau_{23_{\circlearrowleft}}^m, \tau_{12}^m$: stresses in 2D kink frame, at φ
LaRC04 (2005) [63]	$\sigma_1 \geqslant -Y_C : \left(\frac{\tau_{23}^\alpha}{S_{23}-\eta_{23}\sigma_n}\right)^2 + \left(\frac{\tau_{12}^\alpha}{S_{12\ s}-\eta_{12}\sigma_n}\right)^2 \geqslant 1$ $\sigma_1 < -Y_C : \left(\frac{\tau_{23}^m}{S_{23}-\eta_{23}\sigma_n^m}\right)^2 + \left(\frac{\tau_{12}^m}{S_{12}-\eta_{12}\sigma_n^m}\right)^2 \geqslant 1$ $\sigma_n, \tau_{23}^\alpha, \tau_{12}^\alpha$: stresses in fracture plane, at α $\sigma_n^m, \tau_{23}^m, \tau_{12}^m$: stresses in 3D kink frame, at ϕ, φ
Maimí et al. (2007) [64]	$\sqrt{\left(\tau_{23}/S_{23}\right)^2 + \left(\tau_{12}/S_{12}\right)^2} \geqslant 1$ $\alpha_0 = 53°, \theta = \arctan\left(-\sigma_{12}/\sigma_{22}\sin\alpha_0\right)$ $\tau_{23_{er}} =$ $\langle -\sigma_{22}\cos\alpha_0\left(\sin\alpha_0 - \eta_{23}\cos\alpha_0\cos\theta\right)\rangle$ $\tau_{12_{er}} = \langle\cos\alpha_0\left(\lvert\tau_{12}\rvert + \eta_{12}\sigma_{22}\cos\alpha_0\sin\theta\right)\rangle$

Table 3.6: Failure criteria for fibres in tension and compression [57].

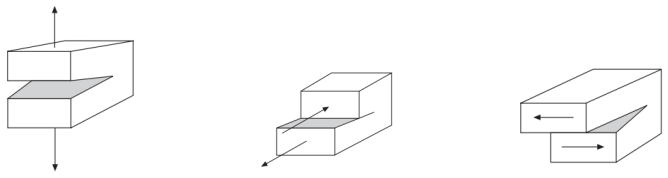
Criteria	Equation
Lee (1982) [65]	$\sigma_2 \geqslant \sigma_{\mathrm{MN}}$ or $\sqrt{(\sigma_{12}^2 + \sigma_{13}^2)} \geqslant \sigma_{\mathrm{MS}}$
Christensen (1997) [66]	$\alpha_1 k_1 (\sigma_2 + \sigma_3) + (\sigma_{12}^2 + \sigma_{31}^2) +$ $(1 + 2\alpha_1) \left[\frac{1}{4}(\sigma_2 - \sigma_3)^2 + \sigma_{23}^2\right] \leqslant k_1^2$ $k_1 = S_{12} = \frac{1}{2}\lvert Y_{\mathrm{C}}\rvert, \alpha_1 = \frac{1}{2}(\lvert \mathrm{Y_C/Y_T} - 1)$
Gosse (2001) [68]	$J_1 = \varepsilon_1 + \varepsilon_2 + \varepsilon_3$ or $\varepsilon_{\mathrm{eqv}} = \sqrt{\frac{(\varepsilon_1-\varepsilon_2)^2+(\varepsilon_1-\varepsilon_3)^2+(\varepsilon_2-\varepsilon_3)^2}{2}}$
Huang et al. (2003) [67]	Failure when $J_1 \geqslant J_{1_{\mathrm{att}}}$ or &eqv $\geqslant \varepsilon_{\mathrm{eqv\ ats}}$ use dissipated energy density $\phi(\varepsilon)$: matrix failure for $0 \leqslant \phi(\varepsilon) \leqslant D_t$

3.1.2 Delamination

In order to better understand the concept of delamination and crack growth, as well as the values used on Finite Element Models, it is important to overview fracture mechanics concepts.

Failure Modes

Hence, every crack can be traced to a combination of three fracture modes - Mode I , Mode II and Mode III. Thus, Mode-I depicts the opening of the crack faces, whilst Mode-II is the sliding mode, and Mode-III the ripping mode -out-of-plane shear mode- deformation, as observed in Figure 3.2.



(a) Mode-I (b) Mode-II (c) Mode-III

Figure 3.2: Fracture modes [69].

Strain energy release rate - G

In 1957, Irwin [70] calculated the work necessary to close a crack of length $a+\delta a$ to the original length a. This is due to the fact that the work needed to close a crack is the same to extend the aforesaid crack. Hence, Irwin defined the stress energy release rate, G, as followed:

$$G = \lim_{\Delta a \to 0} \frac{W}{\Delta a} = \lim_{\Delta a \to 0} \frac{1}{2\Delta a} \int_0^{\Delta a} \sigma_y(\Delta a - r) \cdot v(r) dr \tag{3.7}$$

By mathematical manipulation with each modes stress-intensity factors', Irwin obtained Equation 3.8.

$$G = G_I + G_{II} + G_{III} = \frac{K_I^2}{E'} + \frac{K_{II}^2}{E'} + (1+v)\frac{K_{III}^2}{E} \tag{3.8}$$

Delamination models

This failure mechanism happens at stress-free edges because of different properties of individual layers, at ply drops - internal and external - and at regions prone to out-of-plane bending. The main cause of delamination are the structural and material discontinuities that grow to interlaminar stresses [69]. This is graphically visualised in Figure 3.3.

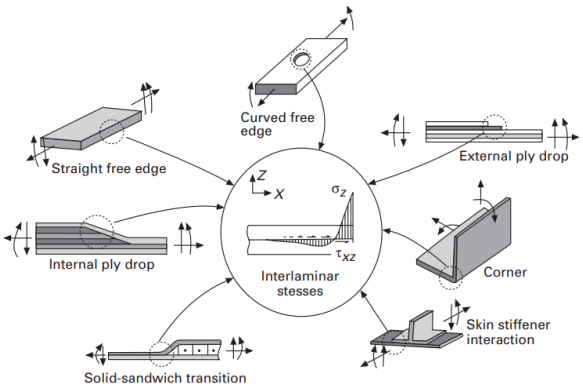


Figure 3.3: Sources of delamination in composite materials [69].

To forecast the beginning and progression of delamination, it is necessary to characterise the interlaminar fracture toughness linked with each of the fracture modes and compute the appropriate strain energy release rates (G_I, G_{II}, G_{III}) for each mode associated with the configuration and loading of interest. The methods to calculate interlaminar fracture toughness using the aforementioned fracture mechanics concepts are outlined in the infamous *Mil Handbook 17* [71]. Made by the American Society for Testing Materials (ASTM), this book highlights the necessary standards for Mode-I - Double Cantilever Beam, DCB - and for mixed Mode-I and

Mode-II (Mixed Mode Bending, MMB). To arrive at the fracture toughness for pure Mode-II, an End-Notch Flexure (ENF) test can be utilised [72].

Therefore, the interlaminar fracture toughness is the critical value of the strain energy release rate, G_C, which is plotted as a function of the mixed mode ration - $\frac{G_{II}}{G_C}$ as observed in Figure 3.4.

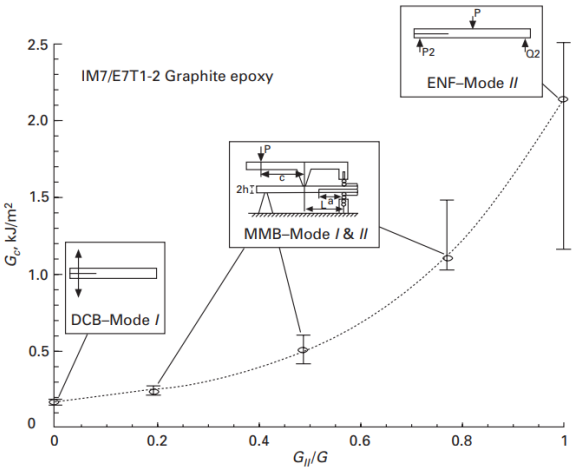


Figure 3.4: Mixed Mode-I and Mode-II delamination criteria [69].

Delamination analysis require a criteria centred on mixed-mode failure and thus, two distinct equations stand out: Wu and Reuter [73] criteria, and Benzeggah and Kenane [74].

$$\left(\frac{G_I}{G_{Ic}}\right)^m + \left(\frac{G_{II}}{G_{IIc}}\right)^n + \left(\frac{G_{III}}{G_{IIIc}}\right)^p \geq 1 \tag{3.9}$$

$$\frac{G_I + G_{II}}{G_{Ic} + (G_{IIc} - G_{Ic})\left[\frac{G_{II}}{G_I + G_{II}}\right]^m} \geq 1 \tag{3.10}$$

Finally, Reeder developed the latter criteria to account for three-dimensional cases where G_{IIC} and G_{IIIC} have different values - Equation 3.11 [75].

$$\frac{G_I + G_{II} + G_{III}}{G_{Ic} + \left(\frac{G_{II}(G_{IIc} - G_{Ic}) + G_{III}(G_{III} - G_{Ic})}{G_I + G_{II} + G_{III}}\right)\left[\frac{G_{II} + G_{III}}{G_I + G_{II} + G_{III}}\right]^{m-1}} \geq 1 \tag{3.11}$$

To finalise, many other models have been developed in order predict delamination initiation - Table 3.7 - and to anticipate crack growth in pre-existing delamination - Table 3.8.

Table 3.7: Failure criteria for delamination initiation [57].

Criteria	Equation
Max stress initiation	$\sigma_3 \geqslant Z_{\mathrm{T}}, \tau_{31} \geqslant S_{31}, \tau_{23} \geqslant S_{23}$
Hashin (1982) [56]	$\left(\frac{\sigma_3}{Z_{\mathrm{T}}}\right)^2 + \left(\frac{\tau_{23}}{S_{23}}\right)^2 + \left(\frac{\tau_{31}}{S_{31}}\right)^2 \geqslant 1$
Lee (1982) [65]	$\sigma_3 \geqslant Z_{\mathrm{T}}$ or $\sqrt{(\sigma_{12}^2 + \sigma_{13}^2)} \geqslant S_{23}$
Tsai (1997) [76]	$\frac{\sigma_1^2 - \sigma_1\sigma_3}{X_{\mathrm{T}}^2} + \left(\frac{\sigma_3}{Z_{\mathrm{T}}}\right)^2 + \left(\frac{\tau_{23}}{S_{23}}\right)^2 \geqslant 1$
Tong-Tsai (1997) [76]	$\frac{\sigma_1^2 - \sigma_1\sigma_3}{X_{\mathrm{T}}^2} + \left(\frac{\sigma_3}{Z_{\mathrm{T}}}\right) + \left(\frac{\tau_{23}}{S_{23}}\right)^2 \geqslant 1$
Degenerated Tsai (1997) [76]	$\left(\frac{\sigma_1}{X_{\mathrm{T}}}\right)^2 + \left(\frac{\sigma_3}{Z_{\mathrm{T}}}\right)^2 + \left(\frac{\tau_{23}}{S_{23}}\right)^2 \geqslant 1$

Table 3.8: Failure criteria for delamination growth [57].

Criteria	Equation
Power Law Growth [77]	$\left(\frac{G_{\mathrm{I}}}{G_{\mathrm{I_c}}}\right)^m + \left(\frac{G_{\mathrm{II}}}{G_{\mathrm{II_c}}}\right)^n + \left(\frac{G_{\mathrm{II}}}{G_{\mathrm{II_c}}}\right)^p \geqslant 1$
Yan et al. (1991) [56]	$G_{\mathrm{T}} \geqslant G_{I_c} + \rho\frac{G_{II}}{G_I} + \tau\left(\frac{G_{II}}{G_I}\right)^2$
Reeder (1993) [78]	For $\frac{G_{II}}{G_I} < \frac{\frac{1}{\zeta}G_{I_c}+G_{I_{I_c}}}{G_{I_c}+\xi G_{I_c}}, \frac{G_I - \xi G_{II}}{G_{I_c}} \geqslant 1$ For $\frac{G_{II}}{G_I} < \frac{\frac{1}{\zeta}G_{I_c}+G_{I_c}}{G_{I_c}+\xi G_{I_c}}, \frac{\zeta G_{II} - G_I}{\zeta G_{II_c}} \geqslant 1$
B-K Law [74]	$G_{\mathrm{T}} \geqslant G_{I_{\mathrm{C}}} + (G_{I_{\mathrm{C}}} - G_{I_{\mathrm{C}}})\left[G_{II}/\left(G_I + G_{II}\right)\right]^\eta$

3.1.3 Finite Element Methodology applied to composite materials

As described on the previous sections, composite materials show a wide range of failure mechanisms due to their complex structure, possibilities and manufacturing

processes. Thus, when computing a composite structure, it is more accurate to think of the composite material as a structure itself than a simple material [57].

Nowadays, many softwares like Abaqus and NASTRAN already have introduced these equations into their Finite Element Models. In terms of ply degradation, the most standard models used are the Hashin criteria and the Larc05.

Hashin Model in ABAQUS

Focusing on the software used throughout this project, i.e., Abaqus and the most relevant model, four different failure modes are considered: fibre rupture in tension, buckling and kinking in compression, matrix cracking under transverse tension and shearing, and,finally, matrix crushing under transverse compression and shearing [79].

As this is a FE model, the aforementioned equations now are in terms of the stress tensor,$\widehat{\sigma}$, for each element. This (effective) stress tensor is computed from Equation 3.12.

$$\widehat{\sigma} = \mathbf{M}\sigma \tag{3.12}$$

Here, σ is the true stress, whilst $\mathbf{M}$ is the damage operator, computed as follows:

$$\mathbf{M} = \begin{bmatrix} \frac{1}{(1-d_f)} & 0 & 0 \\ 0 & \frac{1}{(1-d_m)} & 0 \\ 0 & 0 & \frac{1}{(1-d_s)} \end{bmatrix} \tag{3.13}$$

in which $\mathbf{d_f}$, $\mathbf{d_m}$ and $\mathbf{d_s}$ are internal variables used to characterize fibre, matrix and shear damage, respectively.

Before any damage initiation and evolution, the damage operator, $\mathbf{M}$ is equal to the identity matrix, and, therefore, $\widehat{\sigma} = \mathbf{0}$ [79].

Versing into damage evolution with Hashin's model, it is clear that, prior to initiation, the material is linearly elastic, with the stiffness matrix of a plane stress orthotropic material [80]. Hence, the material's response is computed from

$$\sigma = \mathbf{C_d}\varepsilon^{el} \tag{3.14}$$

where ε^{el} is the elastic strain and $\mathbf{C_d}$ is the damaged elasticity matrix - Equation 3.15.

$$\mathbf{C_d} = \frac{1}{D}\begin{bmatrix} (1-d_f)\,E_1 & (1-d_f)\,(1-d_m)\,\nu_{21}E_1 & 0 \\ (1-d_f)\,(1-d_m)\,\nu_{12}E_2 & (1-d_m)\,E_2 & 0 \\ 0 & 0 & (1-d_s)\,GD \end{bmatrix} \tag{3.15}$$

Here, the component **D** represents the current state of the fibre damage and the internal variables **d** are as previously explained.

In Abaqus, the Hashin law is expressed in terms of a stress-displacement relation, evolving as observed in Figure 3.5 for the four failure modes defined previously.

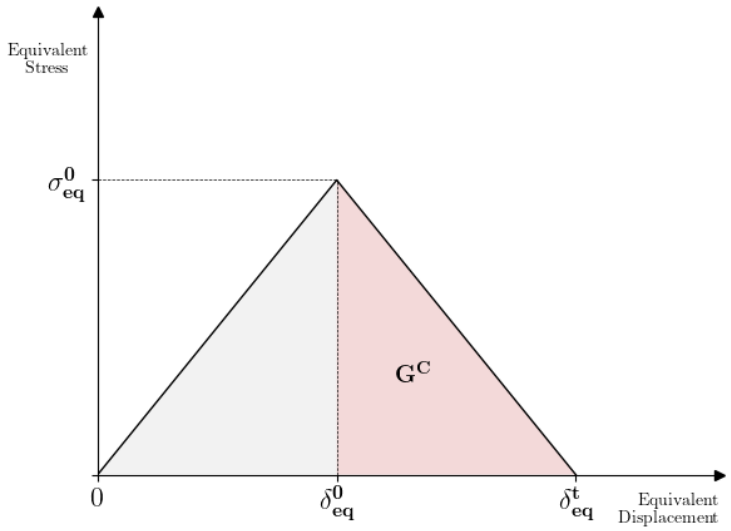


Figure 3.5: Equivalent stress versus displacement [80].

Ergo, for fibre tension ($(\widehat{\sigma}_{11} \geq 0)$):

$$\delta_{eq}^{ft} = L^c \sqrt{\langle \varepsilon_{11} \rangle^2 + \alpha \varepsilon_{12}^2} \tag{3.16}$$

$$\sigma_{eq}^{ft} = \frac{\langle \sigma_{11} \rangle \langle \varepsilon_{11} \rangle + \alpha \tau_{12} \varepsilon_{12}}{\delta_{eq}^{ft} / L^c} \tag{3.17}$$

and for fibre compression ($\widehat{\sigma}_{11} < 0$):

$$\delta_{eq}^{fc} = L^c \langle -\varepsilon_{11} \rangle \tag{3.18}$$

$$\sigma_{eq}^{fc} = \frac{\langle -\sigma_{11} \rangle \langle -\varepsilon_{11} \rangle}{\delta_{eq}^{fc} / L^c} \tag{3.19}$$

Here, the characteristic length, $\mathbf{L^C}$ is based on the element geometry and formulation - it is the length of a line crossing the element for a first order element, half of the same typical length for a second order element.

After initiation, when $\delta_{\mathbf{eq}} \geq \delta^{\mathbf{0}}_{\mathbf{eq}}$, the damage variable for a particular mode is presented in Equation 3.20, in which δ_{eq}^f represents the displacement at which the material is totally damaged at the respective mode.

$$d = \frac{\delta_{eq}^f \left(\delta_{eq} - \delta_{eq}^0 \right)}{\delta_{eq} \left(\delta_{eq}^f - \delta_{eq}^0 \right)} \tag{3.20}$$

To conclude, it is crucial to remark that it is required to specify the energy dissipated due to failure, i.e., $\mathbf{G^C}$, corresponding to the area of the area highlighted in red in Figure 3.5.

Interface Elements

In order to model and compute delamination in composite materials, it is necessary to use the correct interface technique to simulate the adhesive. Most delamination growth investigations employ a fracture mechanics technique and assess the energy release rates G for self-similar delamination development [81].

Since the delamination models are divided into initiation and propagation, most delamination assessments are stress-based and include criteria like the quadratic interaction of the interlaminar stresses in combination with a characteristic distance . Since the typical distance is an average length that depends on the geometry and the qualities of the material, determining it always necessitates significant testing [81]–[83].

Thus, energy release rates are commonly evaluated using the Virtual Crack Closing Technique VCCT developed by Rybicki and Kanninen [84] based on Irwin's assumption explained previously. One key advantage is that this method is computationally efficient since just one analysis is required to determine the energy release rates [81].

The VCCT can provide useful insight into the onset and stability of delamination, but when employed to simulate delamination growth, it may necessitate the use of sophisticated moving mesh techniques to advance the crack front when local energy release rates reach a critical level [85]. Determining the location of the delamination front may be challenging for some geometries and load scenarios, and there must also be a specified starting delamination.

Hence, the use of (de)cohesion elements at interfaces between laminae overcomes some of the aforesaid difficulties. These are founded on Dudgale-Barenblatt cohesive zone approach [86], [87], relating to Griffith's fracture theory for a negligible cohesive zone size when compared with the characteristic dimensions, despite the shape of the constitutive equation [88]. The key advantage of this element is that it allows the simulation to predict both the onset and propagation of delamination without prior knowledge of the crack's location and propagation direction [81].

Decohesion elements can be splitted into two different groups,i.e., continuous interface elements and point decohesion elements. The use of streamlined interaction criteria of the energy release rates for the prediction of delamination propagation and the lack of an interaction criterion for the prediction of softening initiation under mixed-mode loading are characteristics of previously established decohesion components [81].

3.1.4 Skin-Stringer applications

Skin-stringer separation is one of the principal failure mechanisms of laminated composite structures, paired with fibre and matrix cracking. Delamination occurs

due to the relatively small interlaminar strength of the adjacent plies. As mentioned in the previous section, this phenomenon is commonly modelled by the VCCT or by means of cohesive interface elements.

In these scenarios, the drawback of the VCCT is that the crack initiation zone is difficult to predict in large scale complex structures. Cohesive Zone Modelling, CZM, proves to be a great solution for more complex cases [89].

Akterskaia et al. [89] studied the two different variations of CZM, Continuum CZM (CCZM) and Discrete CZM (DCZM). Due to mesh sensitivity and convergence issues, CCZM-based cohesive simulations require a large number of cohesive elements, which increases computing time. The latter, also known as point-wise discrete elements, is an alternative used to overcome the problems of the CCZM. Borg et al. [90] developed a discrete cohesive crack model that presupposes the existence of a maximum load surface of adhesion forces. The approach was implemented by joining the coincident nodes at the interface, and for each pair of these node pairings, a force-displacement relation was constructed. Following computations of the wasted work to zero value based on the fracture energy criterion, adhesive forces were decreased. The aforementioned approach proved to be efficient when it comes to mode I, II and mixed-mode experimental results. For three fracture tests, Xie and Waas [91] employed the DCZM based on non-linear spring type elements and traction-separation bilinear cohesive law. This method was demonstrated to be unaffected by mesh density or load escalation on the examples provided, and there were no convergence issues.

For the suggested discrete techniques to accurately simulate adhesive behaviour, forces or stresses must be calculated precisely, which for very complicated structures could only be done at a significant computational cost. As a result, a variety of multiscale techniques could be used to reduce the number of constitutive equations on the one hand, while also obtaining accurate results on the other. This is particularly important for complex structures, such as composite stringer-skin systems, which are subjected to many conditions.

Thus, several analytical and numerical experiments, skin-stringer separation in composite stiffened panels was taken into account in order to study their progressive damage, buckling, and post-buckling behaviour. Only a few of them will be mentioned in the paragraphs that follow. Wang and Bigger [92] examined the tensions between the stiffener and skin of composite panels with a focus on their separation. Finally, using three stiffened panels in compression, Falzon et al. [93] provided experimental findings looking at crack propagation through the skin-stiffener interface.

In a stiffened panel containing cohesive parts, Balzani and Wagner [94] investigated the debonding of the skin from the stiffener, whilst, Raimondo and Riccio [95], [96] carried out skin-stringer debonding analysis on the test case of two single stringer panels by using the VCCT.

Akterskaia et al. [89] examined the system presented in Figure 3.6 in a full shell (elements) model and a smaller solid model.

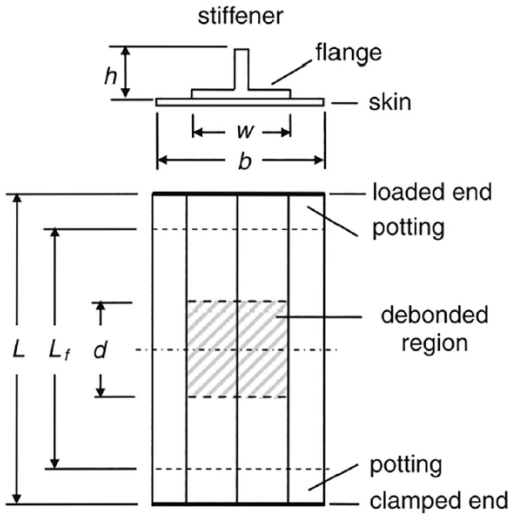


Figure 3.6: Geometry of the specimen analysed [89]

For the shell model, the connection between skin and stringer was made of spring type connector elements with linear elastic behaviour, tying opposite nodes of the two parts. The initial stiffness of these elements is computed using Equation 3.21 [89].

$$K = \frac{EA}{t} \tag{3.21}$$

E represents the Young's modulus of the adhesive layer whilst A and t are the in-plane nodal area and thickness, respectively. The connector elements, CONN3D2 in Abaqus, are used for shell models, in order to simulate the conditions of the adhesive layer without the use of cohesive elements. These elements tie conventional 2D shell elements of the skin and stringer, as observed in Figure 3.7.

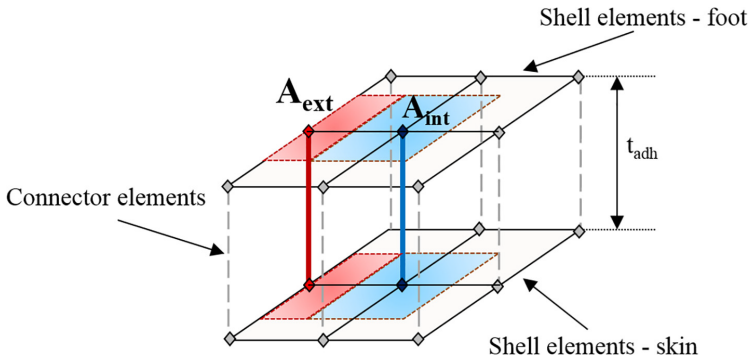


Figure 3.7: Discrete interface elements connecting skin and stringer parts [89].

After, using an additional Python script for the connector elements, the Quadratic Stress Criterion was applied - Equation 4.4 - in order to determine areas prone to delamination.

As for the solid model, traditional C3D8 elements were used for the skin and stringer whilst the CZM was conducted with non-zero thickness COH3D8 elements with bilinear traction-separation law for the adhesive layer. Furthermore, mesh convergence investigations proved that a element with 1mm in the in-plane length direction and a 0.25mm out-of-plane length, equalling to one element per lamina in the thickness direction were appropriate as for the reliability of the study and computational time. To conclude, four cohesive elements per length of one solid element, as increasing the number of cohesive elements proved to be unnecessary.

In order to connect the cohesive elements to the skin and stringer solid elements, the *Tie constraint was applied, defining the Master/Principal surface as the solid interface and the Slave/Secondary on the cohesive layer. This methodology predicted the possibility of convergence issues during the softening behaviour and stiffness degradation, which are common for cohesive elements. Ergo, in order to resolve this problem, viscous regularisation of the constitutive equations was used. A viscosity parameter of 0.001 was selected, which Akterskaia et al. [89] stated to be relatively high, despite the fact that greater viscosity parameters could lead to higher load peaks, they defended that it is crucial to judge each scenario in order to maintain a good balance between numerical convergence and experimental results.

Similarly, Hühne et al. [97] computed a reference model mimicking Akterskaia et al. [89], with the same mesh density and element type. This resulted in 32.800 C3D8 elements. This approach was use, contrary to the previous approach, to compute matrix and fibre damage.

The model was then compared to experimental values achieved by Orifici et al. [98], exhibiting a satisfactory results, although highlighting the need of introducing a global-local approach in order to save computational time, due the difficulty it is to model large scale complex composite systems.

For the purpose of this dissertation, following the previously defined failure and damage criteria, a sub-routine UMAT was implemented in the model as it allows the extraction of more information from the Finite Element Model when it comes to composite material response. In terms of cohesive modelling, the B-K law [74] will be implemented throughout this project. This will be later explained in chapter 4.

3.2 Global-Local Technique

Global-local approaches are essential design tools that have gained prominence for simulating big and complicated systems, due to the requirement to reduce computing effort on the one hand, without sacrificing quality and information of the areas more prone to damage [89]. Several methodologies have been implemented, varying from one-way or two-way, as well as loose and tight coupling procedures [97].

This methodology rose to overcome some of the difficulties of local multigrid algorithms, particularly for finite element applications. This was first introduced by Brandt [99] and extended to the FE method by Parsons and Hall [100], [101]. In local multigrid methods, in addition to a global coarse mesh, a hierarchy of local meshes is built in a manner known as the multigrid cycle to increase the effectiveness of a solution with an inexact local solver. Through prolongation and restriction operators that are defined on the entire overlapping local region, data is transported between hierarchical meshes [97].

Nevertheless, this approach has some drawbacks, mainly the fact that they are intrusive with commercial FE softwares - like Abaqus - and data transfer between hierarchical meshes throughout the overlapped region is problematic.

For this purpose, Gendre et al. [102] suggested a non-intrusive coupling concept to analyse local non-linearities, in order to lessen the intrusiveness using commercial FE codes, named the iterative global/local method. This utilises the non-overlapping domain decomposition (DD) data transfer method to modify the conventional global/local method.

Two models are needed for the iterative global/local algorithm: a nonlinear local fine mesh model and a linear global coarse mesh model. The technique, however, mandates that the boundary or interface of both meshes must match. The iterative global/local technique has many benefits, with the exception of the matching mesh on the interface: the data transfer of nodal displacement and force between the two models only occurs along the interface, which is simple and practicable to execute in numerical performance, making the iterative scheme non-intrusive by avoiding any modification of the industrial code or the solver [103].

From a computational standpoint, there are numerous ways to connect the various models that make up the solution scheme, giving rise to numerous subcategories of global/local and multiscale techniques. One-way and two-way strategies, as well as loose and tight coupling procedures, are potential distinctions between the present technologies. One-way coupling, as opposed to two-way coupling, refers to the fact that information is only transferred from one model to another, either from the global to the local model or vice-versa. Contrarily, two-way coupling methods unquestionably transmit information in both directions. Loose coupling involves the

employment of geographically separated models, or at the very least, different simulations that share information but are computed sequentially. This is relevant to the relationship between the two levels of analysis. Tight coupling, on the other hand, refers to numerical methods that resolve both the global and local systems of equations concurrently [97].

3.2.1 Abaqus Submodelling analysis

The global-local method is a submodelling technique that is implemented in Abaqus without many complications. This technique allows the study of a small region of a complex model with a refined mesh, by interpolating the solution of the larger model. This approach is particularly helpful when an exact, detailed answer must be obtained in the local region and the thorough modelling of that small area has little bearing on the final solution. The global solution, along with any loads placed on the local area, defines the response at the local region's border, which in turn determines the solution of the submodel. The method depends on the global model accurately specifying this submodel boundary reaction.

Abaqus allows two different submodelling techniques, either node-based or surface-based. The first is particularly interesting as it allows a great technique, i.e., shell-to-solid submodelling, which saves many computational efforts as it is possible to define a large scale shell model and transfer the boundary conditions for a more complex solid model, in order to achiever more reliable results.

Shell-to-solid submodeling in Abaqus

Since there will be discontinuities and the nodes in the shell model will not be located exactly on the correct location for the solid model, it is necessary to implement an interpolation procedure and consequent tolerance as to transfer the correct displacement field. Abaqus employs two different types of tolerances to establish the relationship between the local and global model. The nearest location on the global model's shell mid surface is first identified. The "image node" of the driven node will thereafter be referred to as this point. To determine if the image node falls inside the scope of the global model, utilise the external tolerance parameter. After then, the distance between the driven node and its image is compared to half of the user-specified maximum shell thickness - Figure 3.8.

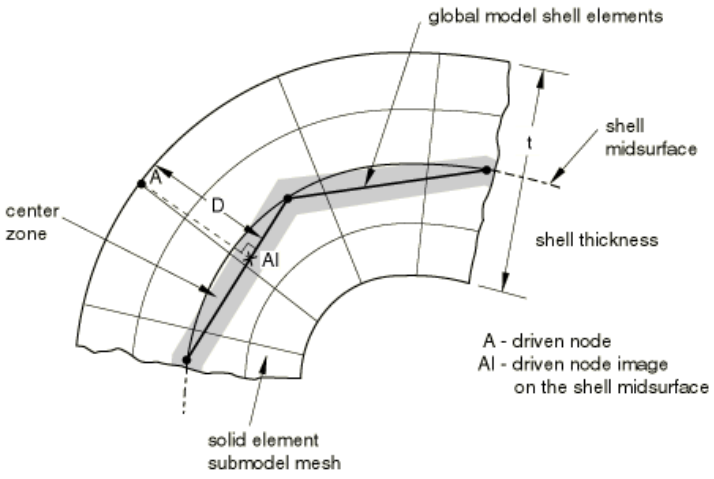


Figure 3.8: Center zone in shell-to-solid submodeling [104].

If located within half of the thickness plus the external tolerance, the node is accepted. Nonetheless, if the global model has different shell thicknesses, this check will only be roughly accurate, and in that case, it won't protect the user in areas of the global model where the thickness is less than the maximum thickness that the user has selected.

The prescribed values of the driven variables are interpolated from the values sent to the file output for the global model once the positions of the driven nodes (or image nodes for the shell-to-solid example) have been established. To get precise values at the driven nodes, these must have been written at a frequency high enough. For the global model nodes from which the values for the driven nodes will be interpolated, all components of displacements, temperatures, charges, and—for sophisticated steady-state dynamic analysis—the phase angles as well as the amplitudes, must be written. Responses are often written for all nodes in small global models. Node sets including the nodes in the areas surrounding the submodel border may be made for big global models [104].

Furthermore, the driven degrees of freedom in the shell-to-solid situation are automatically determined by the distance between the driven node and the midsurface of the shell. The user-specified centre zone, shown in Figure 3.8, is where the node must be in order for all displacement components to be driven. Only the displacement terms parallel to the shell midsurface are driven if the node is outside the centre zone. By default, 10% of the maximum shell thickness is used as the size of the centre zone.

3.2.2 Global-Local Technique in skin-stringer analysis

Due to the computational complexity of modelling large scale finite element models, especially those made with composite materials, the global-local submodeling technique proves to be an exceptional tool to access all types of failure mechanisms.

This approach has already been investigated by several aforementioned authors, particularly with the use of two-way coupling techniques.

Thus, the two-way coupling procedure is typically defined as shown in Figure 3.9. The coupling loop consists of three crucial operations, which are iteratively repeated until final collapse is achieved. Firstly, a global analysis is used in order to evaluate critical regions and determine the location of the local models. After, local models should be implemented, using the displacements provided by the global solution. Finally, based on average damage variables, global interface stiffness is computed and returned to the global level [89].

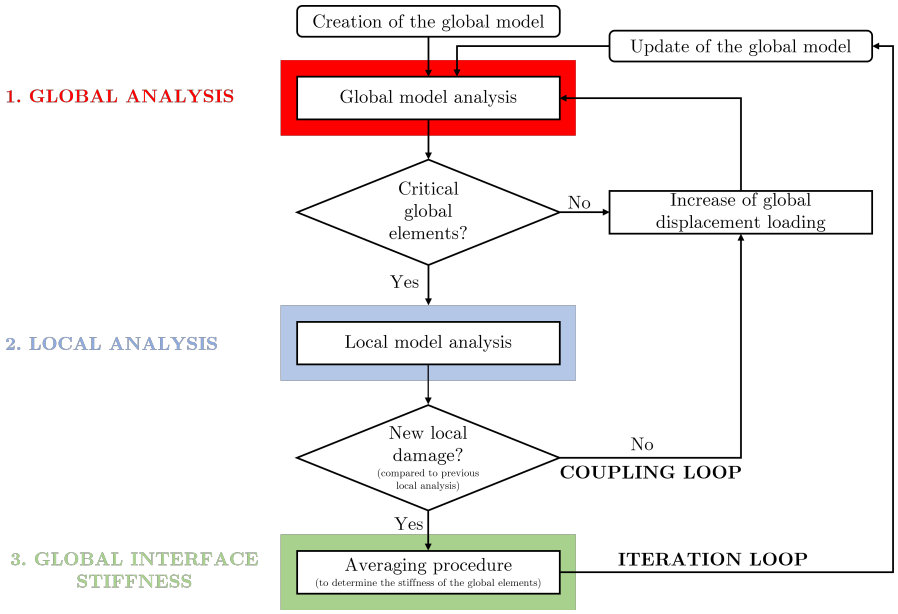


Figure 3.9: Two-way loose coupling procedure for skin-stringer failure mechanisms [89].

This methodology has been implemented for several skin-stringer analysis using many commercial Finite Element (FE) softwares, Abaqus included. Hühne et al. [97] created a FE-based two-way loose coupling method, capable of simulating composite structures while accounting for material and geometrical non-linearities, whilst achieving interaction between the two levels of computation. The information exchange accross models is carried iteratively, as shown Figure 3.9. The non-linear studies do not halt because the global and local simulations are run one after the other rather than concurrently. As for updating the global model, it is important to highlight that this was conducted by modifying material properties.

Firstly, the global model was implemented. This was achieved by the use of two-dimensional shell elements, due to the fact that the global model should be simple whilst preserving sufficient accuracy, in order to reach adequate and reliable results. As explained previously, the first purpose of this model is to accurately determine critical areas for posterior local analysis. Following, local models are created for

the aforementioned global regions, which are chosen based on the outcomes of the global simulation. Thus, these models are now composed by solid three-dimensional elements with denser meshes. Since the purpose of this study is to determine fibre and matrix failure, the use of a thorough material degradation model to analyse the development of intralaminar damage. In order to return information from the local to the global model, a so called "homogenisation-like" [97] was introduced, where one local part test consisting of the local components connected to one specific laminate layer of one global component were subjected to tension and shear tests in order to determine the updated engineering constants. Additionally, each of these local component tests included the final deteriorated material attributes from the local analysis, distinguished by a linear material definition.

This method was implemented following the geometry and experimental tests shown in Figure 3.6 [98]. Here, two separate reference models—one shell model and one solid model- were utilised to assess the coupling procedure's outcomes. The identical material degradation model was installed in both models, following [105]. 2700 shell elements (S4R of Abaqus), with a side-length equal to 4 mm, were chosen for the reference shell model following a preliminary mesh convergence analysis with respect to the lowest buckling load of the panel, while 680,800 volume elements (C3D8 of Abaqus), with an in-plane side-length equal to 1 mm and one element per layer over the thickness, were used for the reference solid model.

As for results, the difference between the maximum load levels is less than 1% for the coupling procedure, when compared to the reference shell model, exhibiting satisfactorily results. It was observed from the experimental and numerical findings shown in [98] that the coupling results closely matched the experimental data, whilst the other numerical simulations somewhat overestimate the maximum load attained during the test. In particular, the maximum load determined by the Orifici simulation differs from the maximum load determined by the coupling findings by around 15%. Nonetheless, this disparity could be due to the use of various damage criteria and degradation models in those computations, as well as the significance of interlaminar damage events. The overall results proved very reliable, showing the benefits of the global-local technique in material failure analysis.

Furthermore, this methodology was introduced to delamination analysis by Akterskaia et al. [89]. Here, the global model was developed as explained in Section 2.3.4 and the update of the global model was developed by changing the properties of the connector elements. Through the use of four coupling loops, a global-local analysis was done, increasing the prescribed displacement to the presented values: 1.0 mm, 1.4 mm, 1.6 mm, and 2.0 mm, respectively. Experimental and numerical results show that the stiffener's skin and foot have buckled in opposing directions, ruling out any problems with the layers' possible initial interpenetration during calculations.

Experimental tests proved that damage began from the debonded regions and, before spreading in the longitudinal directions, the damage grew along the pre-debonded edge from the first debonded locations. In terms of predicting the final debonded region, it was determined that the final experimental value was 165mm, whilst the global-local analysis yielded a value of 120mm. This was explained by the fact that fibre failure could influence the results and were not considered throughout the simulations.

All in all, it is safe to state that the global-local technique is extremely beneficial in terms of results reliability whilst saving computational efforts. This was proved by Akterskaia et al. [89] by showing a decrease of around 65% in terms of relative computational time whilst achieving satisfactory results.

Part III

Numerical model

Chapter 4

Composite Damage Model

This Part commences with a deep dive into the theory behind the modelling of cohesive elements, before taking a closer look into the software used throughout this thesis. This section advances, then, into the complicated intricacies of material sub-routines and its requirements to effectively pair the commercial software herein utilised. Following the definition of crucial concepts, the validation model is presented by carefully explanation of the materials used, as well as the methodology applied. The global and local models are defined and finally, analysed, culminating in the accurate validation of the technique.

4.1 Cohesive Zone Models

Failure of laminated fibre-reinforced composites is attributed to the occurrence of intralaminar and/or interlaminar damage mechanisms, namely delamination. These damage mechanisms are predominantly influenced by many elements, including loading conditions, geometric configuration, and stacking sequences. However, it is important to note that delamination is a prevalent form of damage in these materials due to their intrinsic weakness in interlaminar bonding. This weakness has the potential to greatly undermine their overall structural integrity. However, the identification of this issue during the inspection process is not a simple affair, thereby adding complexity to maintenance procedures in composite buildings. Consequently,

the apprehension over the initiation and progression of delamination is inherently a significant issue.

A methodology for numerically simulating delamination can be situated within the framework of Damage Mechanics, specifically in the form of Cohesive Zone Models (CZMs). These models have demonstrated significant effectiveness in conducting non-linear progressive failure analyses that encompass both ply damage and delamination [1], [106]. Hence, this approach is considered the most viable tool for assessing complex three-dimensional (3D) structures that exhibit many instances of delamination initiation and propagation fronts. It is being extensively employed in the modelling of interlaminar damage.

The notion of the cohesive zone model (CZM), as seen in Figure 4.1, represents the damaged material (fibre-reinforced polymer zone- FPZ) through the use of a hypothetical fracture (dashed line) that facilitates the transmission of cohesive forces across different surfaces. The tractions in question are regulated by a cohesive law that establishes a relationship between them and the crack opening displacements (CODs). This cohesive law is based on the concept of fracture energy.

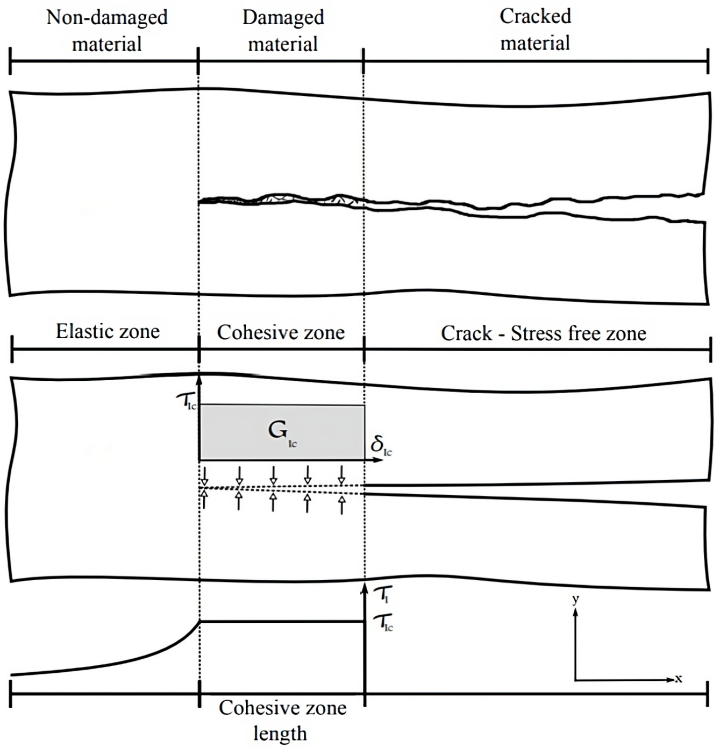


Figure 4.1: Top: FPZ of a quasi-brittle material. Middle: CZM concept. Bottom: stress distribution along the crack path for a constant cohesive law under pure mode I loading [107].

According to existing literature, cohesive zone models (CZMs) are subject to a cohesive interfacial law, commonly referred to as a traction-separation law. This law

establishes mechanical relationships between cohesive tractions (σ) and interfacial separations (δ), which play a crucial role in determining the softening behaviour and influencing the development of the fracture process zone (FPZ) [109]. The rule under consideration establishes the method in which interfacial behaviour is defined. According to this law, as the separation between interfaces grows, the tractions exerted across the interface initially reach a maximum value. However, they progressively decrease and ultimately disappear when total decohesion occurs, resulting in the complete degradation of both stiffness and strength [1], [108], [109]. Thus, via the inclusion of the characterization of both the initiation and progression of damage, cohesive zone models (CZMs) maintain the essential prediction criteria necessary for establishing a thorough depiction of fracture within a continuum. To get a comprehensive comprehension of the cohesive law, we shall examine a quasi-brittle bar with a length denoted as L and a cross-section denoted as A (as shown in

$$\sigma = \begin{cases} k\delta, \delta < \delta_i \\ (1-d)k\delta, \delta_i \leq \delta < \delta_f \end{cases} \tag{4.1}$$

where the variable "d" represents the damage variable that is influenced by the displacement jump. In other words, as the damage increases, the material's capacity to transport loads decreases. This relationship is captured by the parameter "d".

Experimental characterisation is necessary to determine initiation strength, fracture toughness, and shape parameters. These determinations can vary depending on the three opening modes: mode I (occurring in the normal direction), shear mode II (occurring in the in-plane direction), mode III (occurring in the out-of-plane direction), and mixed-mode [109]. However, the practical limitations associated with directly measuring these variables have led researchers to adopt alternate approaches such as analytical or semi-analytical computations using inverse techniques [110]–[112]. Various laws have been suggested for the representation of interlaminar damage in composite materials. These laws differ primarily in terms of the criteria for onset and evolution under mixed-mode conditions, as well as the assumed idealised shape that governs the progression of damage. The idealised shapes considered range from bi-linear to trapezoidal or exponential profiles. Nevertheless, it is important to acknowledge that even reduced geometries may demonstrate restricted precision, especially when faced with a significant Free Play Zone (FPZ) resulting from plastic deformation or the effects of fibre bridging and friction [109]. In such situations, the softening law could display a maximum point at small displacements in order to account for the localised deformation at the fracture tip, along with a longer decay at larger crack opening displacements to represent the effects of bridging in the region behind the crack.

As a result, in order to represent this complex behaviour, researchers have recommended the use of multi-linear softening laws [113], [114]. These laws combine two or more bi-linear cohesive rules, as seen in Figure 4.2 [1], [108]. These models have demonstrated the ability to not only offer a more accurate assessment of the length of the process zone, but also to provide a more exact depiction of R-curves that have been discovered by experimental means [1], [108], [113].

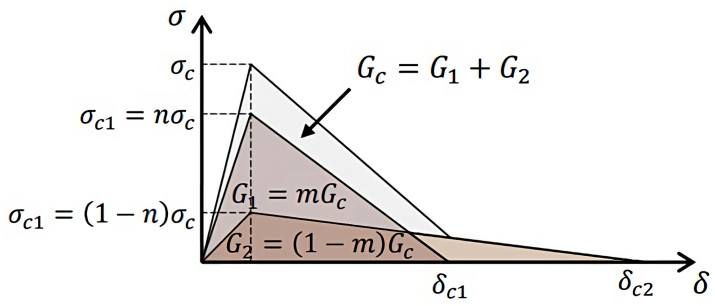


Figure 4.2: Tri-linear cohesive law obtained by superposing two bi-linear laws [108].

Versing now into Abaqus, this software offers a wide range of element types depending on the application and behaviour of the system. First , it is important to look into the physical representation of this mathematical concept, as shown in Figure 4.3

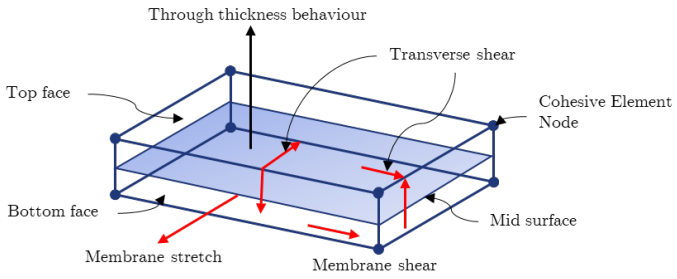


Figure 4.3: Spatial representation of a three-dimensional cohesive element and respective deformation modes [115] .

The transverse shear behaviour of the cohesive element is quantified by the relative displacement of the bottom and top faces measured in the plane orthogonal to the thickness direction. Although it is supposed that the cohesive elements do not produce any stresses in a purely membrane response, stretching and shearing of the mid surface of the element, positioned halfway between the bottom and top face are connected to membrane strains in the cohesive element [115].

For the modeling of bonded interfaces in composite structures traction-separation -based modelling should be used, as the cohesive elements are simulating a very thin

adhesive whose thickness should be considered, for practical purposes, null. This element should be located in areas with stress concentrations that are expecting cracks which must not propagate and deflect into the composite material.

In Abaqus, the traction-separation model assumes, initially, a linear elastic behaviour, followed by delamination initiation and propagation. Hence, the elastic behaviour can be defined by Equation 4.2.

$$\mathbf{t} = \begin{Bmatrix} t_n \\ t_s \\ t_t \end{Bmatrix} = \begin{bmatrix} E_{nn} & 0 & 0 \\ 0 & E_{ss} & 0 \\ 0 & 0 & E_{tt} \end{bmatrix} \begin{Bmatrix} \varepsilon_n \\ \varepsilon_s \\ \varepsilon_t \end{Bmatrix} = \mathbf{E}\varepsilon \tag{4.2}$$

Here, the traction vector $\mathbf{t}$ is made of three components, the two shear tractions, $\mathbf{t_n}$ and $\mathbf{t_s}$, and $\mathbf{t_t}$, the normal direction. Since $\mathbf{T_0}$ is the initial thickness of the cohesive element, ε refers to the normal strains in the three directions [115].

Similar to the framework used for damage modelling in conventional materials, the method used for cohesive materials consists of three parts: damage initiation criteria, an evolution law and a option of element deletion on a defined damaged state. Nonetheless, damage modelling for traction-separation response has particularities that should be studied prior to the simulation.

Firstly, the initial response of the cohesive element is linear as described formerly. This progresses until a defined parameter and begins to separate, as seen in Figure 4.4.

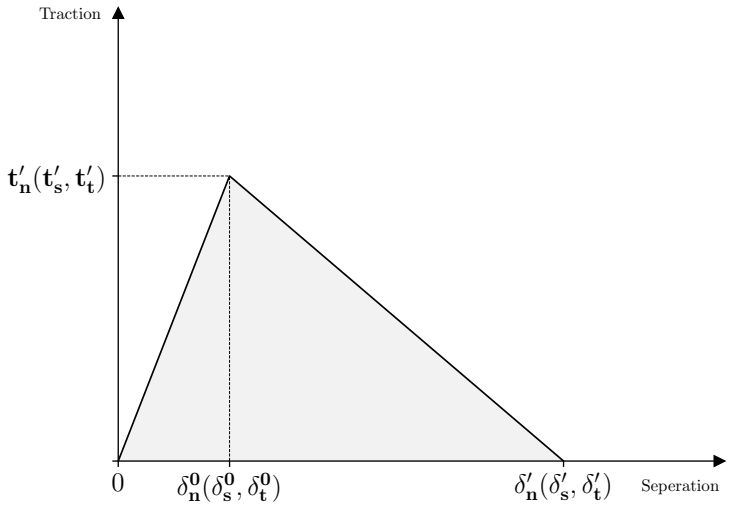


Figure 4.4: Traction-separation response [115].

t_n^o, t_s^o, and t_t^o represent the peak values of the nominal stress, which occurs when the deformation is either purely normal to the interface or purely in the first or the second shear direction, respectively. like, $\varepsilon_n^o, \varepsilon_s^o$, and ε_t^o represent the peak values of

the nominal strain when the deformation is either purely normal to the interface or purely in the first or the second shear direction, respectively.

Maximum and Quadratic Nominal Stress Criteria

When the maximum nominal stress ratio reaches a value of one, damage is presumed to start, expressed in Equation 4.3. As for the Quadratic Nominal Stress Criterion, damage is assumed to start when Equation 4.4 is verified.

$$\max\left\{\frac{\langle t_n\rangle}{t_n^o}, \frac{t_s}{t_s^o}, \frac{t_t}{t_t^o}\right\} = 1 \qquad (4.3) \qquad \left\{\frac{\langle t_n\rangle}{t_n^o}\right\}^2 + \left\{\frac{t_s}{t_s^o}\right\}^2 + \left\{\frac{t_t}{t_t^o}\right\}^2 = 1 \quad (4.4)$$

Maximum Nominal Strain Criteria

When the maximum nominal strain ratio reaches a value of one, damage is presumed to start. This need may be expressed as observed in Equation 4.5. Finally, for the Quadratic Nominal Strain Criterion, damage is assumed to start when Equation 4.6 is true.

$$\max\left\{\frac{\langle \varepsilon_n\rangle}{\varepsilon_n^o}, \frac{\varepsilon_s}{\varepsilon_s^o}, \frac{\varepsilon_t}{\varepsilon_t^o}\right\} = 1 \qquad (4.5) \qquad \left\{\frac{\langle \varepsilon_n\rangle}{\varepsilon_n^o}\right\}^2 + \left\{\frac{\varepsilon_s}{\varepsilon_s^o}\right\}^2 + \left\{\frac{\varepsilon_t}{\varepsilon_t^o}\right\}^2 = 1 \quad (4.6)$$

Furthermore, for damage evolution, the law represents the rate in which the material stiffness degrades after the initiation criteria is fulfilled. Likewise, the framework utilized by the software is the same as for conventional materials and despite the fact that many models have been purposed, as explained in Section 2.3.2, the software has different possibilities as for this part of the simulation.

First of all, the stress components of the traction-separation model are affected by the damage according to the following equations:

$$t_n = \begin{cases} (1-D)\bar{t}_n, & \bar{t}_n \geq 0 \\ \bar{t}_n, & \text{otherwise (no damage to compressive stiffness)} \end{cases} \qquad (4.7)$$

$$t_s = (1-D)\bar{t}_s \qquad (4.8) \qquad t_t = (1-D)\bar{t}_t \qquad (4.9)$$

Here, D represents a scalar variable that relates to the overall damage in the adhesive. Initially, the value is 0 and it monotonically evolves to 1 upon further loading after damage initiation. $\bar{t}_n, \bar{t}_s$ and $\bar{t}_t$ are the stress components predicted by the elastic traction-separation behaviour for the current strains without damage.

For damage under normal and shear deformation, it is crucial to highlight the effective displacement and equivalent normal strain - Equation 4.10 and Equation 4.11 [81].

$$\delta_m = \sqrt{\langle\delta_n\rangle^2 + \delta_s^2 + \delta_t^2} \qquad (4.10) \qquad \varepsilon_m = \sqrt{\langle\varepsilon_n\rangle^2 + \varepsilon_s^2 + \varepsilon_t^2} \qquad (4.11)$$

Since the cohesive elements will be subjected to mixed mode delamination, it is crucial to understand how the software operates in this condition, as observed in Figure 4.5. This figure presents a schematic representation of the dependency of damage initiation and evolution on the mode mix, for a traction-separation response with isotropic shear behaviour [115].

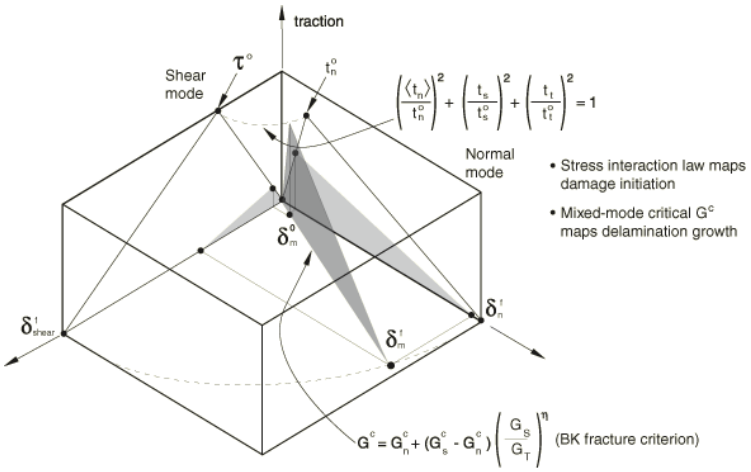


Figure 4.5: Illustration of mixed-mode response in cohesive elements [115].

Figure 4.5 displays the shear and normal separation magnitudes along the two horizontal axes, as well as the traction along the vertical axis. The reaction under pure normal and pure shear deformation are depicted by the uncovered triangles in the two vertical coordinate planes, respectively. The damage response under mixed mode settings with various mode mixes is represented by each intermediate vertical plane (which contains the vertical axis).

There are many possibilities to define damage evolution in Abaqus, and, therefore, Table 4.2 shows a summary of the applicable models and, in order to better understand Table 4.2, Table 4.1 shows additional parameters and important definitions for the analysed models.

Table 4.1: Parameter definition for Damage Evolution [115].

Symbol	**Definition**
$\boldsymbol{\delta_m^0}$	Effective Displacement at damage initiation
$\boldsymbol{\delta_m^f}$	Effective Displacement at failure
$\boldsymbol{\delta_{max}^f}$	Maximum value of the effective displacement during loading history
$\mathbf{G_n}$	Work done by the tractions and their conjugate relative displacement in the normal direction
$\mathbf{G_s}$	Work done by the tractions and their conjugate relative displacement in the first shear direction
$\mathbf{G_t}$	Work done by the tractions and their conjugate relative displacement in the second shear direction
$\mathbf{G_T}$	$G_T = G_n + G_s + G_t$
$\mathbf{G_S}$	Energy dissipated due to work in the first and second shear directions, $G_S = G_s + G_t$
$\mathbf{G^C}$	Energy dissipated due to failure
$\boldsymbol{\eta}$	Material Parameter

Table 4.2: Damage Evolution in Abaqus [115].

	Evolution Law	Formulation
Based on Effective Displacement	Linear Damage	$D = \frac{\delta_m^f(\delta_m^{\max}-\delta_m^o)}{\delta_m^{\max}\left(\delta_m^f-\delta_m^o\right)}$
	Exponential Damage	$D = 1 - \left\{\frac{\delta_m^o}{\delta_m^{\max}}\right\}\left\{1 - \frac{1-\exp\left(-\alpha\left(\frac{\delta_m^{\max}-\delta_m^o}{\delta_m^f-\delta_m^o}\right)\right)}{1-\exp(-\alpha)}\right\}$
	Tabular Damage	Specify directly the fracture energy as a function of the mode mix in tabular form.
Based on Energy	Power Law Form	$G^C = 1/\left(\left\{\frac{m_1}{G_n^C}\right\}^\alpha + \left\{\frac{m_2}{G_s^C}\right\}^\alpha + \left\{\frac{m_3}{G_t^C}\right\}^\alpha\right)^{1/\alpha}$
	BK Form	$G_n^C + \left(G_s^C - G_n^C\right)\left\{\frac{G_S}{G_T}\right\}^\eta = G^C$
	Linear Damage	$D = \frac{\delta_m^f(\delta_m^{\max}-\delta_m^o)}{\delta_m^{\max}\left(\delta_m^f-\delta_m^o\right)}$
	Exponential Damage	$D = \int_{\delta_m^o}^{\delta_m^{\max}} \frac{T_{\text{eff}}\,d\delta}{G^C-G_o}$

For this analysis, the BK law was selected, following the literature. Nonetheless, this quickly proved to be the most efficient option paired with the Quadratic Stress Criteria, especially in terms of accuracy and computational efficiency.

To conclude, there are many element options available depending on the application. Thus, for future understanding, the most efficient cohesive element - and, therefore, the element selected throughout this dissertation-, is the COH3D8, which means that it is a three dimensional 8-node cohesive element.

4.2 Continuum damage mechanics

4.2.1 Introduction

A novel 3D damage approach has been introduced, following the framework developed by Longo [116] to model the progressive failure of thin composite structures, effectively considering both intralaminar and interlaminar damage mechanisms. The advanced nonlinear Finite Element software Abaqus/Standard has been harnessed, incorporating the intralaminar constitutive model through a dedicated Fortran subroutine to interact seamlessly with the Abaqus platform. Intralaminar damage

modes have been examined within the framework of the CDM, utilizing the principles of thermomechanics and nonlinear irreversible processes. To ensure numerical accuracy, the smeared crack formulation has been employed to maintain objectivity in the discretization. Additionally, the interlaminar damage has been studied using the cohesive zone model (CZM) available in Abaqus, adopting a traction-separation approach for comprehensive analysis.

4.2.2 Intralaminar material model

In contrast to Linear Elastic Fracture Mechanics (LEFM), which views the origin and evolution of microcracks as a discontinuous occurrence, Continuum Damage Mechanics (CDM), employs continuous internal state variables known as damage variables. These are associated with the density of internal defects inside a Representative Volume Element (RVE). Therefore, damage variables serve as indicators of the average deterioration of materials, reflecting the many forms of damage occurring at the mesoscale level.

The material model used throughout this project is the work of Longo [116], who developed a stable sub-routine to improve mesoscale models in Abaqus Implicit. Thus, in his work, Classic Lamination Theory (CLT) was adopted and the laminae considered to be an orthotropic material. When considering the mechanical behaviour of a lamina, the relationship between the effective stress tensor $\tilde{\boldsymbol{T}}$ and the strain tensor $\boldsymbol{E}$ may be expressed using the generalised Hooke's equation.

$$\tilde{T} = \mathbb{Q} : E \tag{4.12}$$

where $\mathbb{Q}$ represents the stiffness tensor of the undamaged material, which is equivalent to the reciprocal of the compliance tensor of the undamaged material $\mathbb{Q} = \mathbb{C}^{-1}$. Equation 4.12 can be expanded in terms of components by using the Voigt notation, yielding:

$$\begin{Bmatrix} \bar{\sigma}_{11} \\ \bar{\sigma}_{22} \\ \bar{\sigma}_{33} \\ \bar{\tau}_{12} \\ \bar{\tau}_{13} \\ \bar{\tau}_{23} \end{Bmatrix} = \begin{bmatrix} \frac{1}{E_1^0} & -\frac{\nu_{21}^0}{E_2^0} & -\frac{\nu_{31}^0}{E_3^0} & 0 & 0 & 0 \\ -\frac{\nu_{12}^0}{E_1^0} & \frac{1}{E_2^0} & -\frac{\nu_{92}^0}{E_3^0} & 0 & 0 & 0 \\ -\frac{\nu_{13}^0}{E_1^0} & -\frac{\nu_{23}^0}{E_2^0} & \frac{1}{E_3^0} & 0 & 0 & 0 \\ 0 & 0 & 0 & \frac{1}{G_{12}^0} & 0 & 0 \\ 0 & 0 & 0 & 0 & \frac{1}{G_{13}^0} & 0 \\ 0 & 0 & 0 & 0 & 0 & \frac{1}{G_{23}^0} \end{bmatrix}^{-1} \begin{Bmatrix} \epsilon_{11} \\ \epsilon_{22} \\ \epsilon_{33} \\ \gamma_{12} \\ \gamma_{13} \\ \gamma_{23} \end{Bmatrix} \tag{4.13}$$

Here, the subscript 1 represents the in-plane longitudinal direction, the subscript 2 represents the in-plane transverse direction whilst the subscript 3 represents the

through-the-thickness direction refers. E_1^0, E_2^0 and G_{12}^0 are the in-plane elastic orthotropic properties of the undamaged lamina, E_3^0 is the elastic modulus in the through-the-thickness direction of the undamaged lamina, G_{13}^0 and G_{23}^0 are the out-of-plane shear moduli of the undamaged lamina and $\nu_1^0, \nu_2^0, \nu_{19}^0, \nu_2^0, \nu_{23}^0, \nu_{27}^0$ are the Poisson's ratio of the undamaged lamina.

The constitutive equation for a damaged lamina is given by $\boldsymbol{T} = \mathbb{Q}_d : \boldsymbol{E}$, where $\boldsymbol{T}$ is the nominal stress tensor and $\mathbb{Q}_d$ is the stiffness tensor of the damaged material. Therefore, in order to include the intralaminar damage model into a finite element system, it is necessary to compute the stiffness tensor (or the compliance tensor $\mathbb{C}_d$). When considering a Representative Volume Element (RVE) under a general load, there are two distinct ways that may be employed. These approaches will be outlined in the following two paragraphs.

Compliance tensor calculation: first approach

For the first approach implemented by Longo [116], defined the effective stress tensor as:

$$\tilde{\boldsymbol{T}} = \mathbb{D}\boldsymbol{T} \tag{4.14}$$

in which $\mathbb{D}$ is the damage transformation tensor, described in matrix form as:

$$[\mathbb{D}]_{ij} = \frac{1}{1-d_i}\delta_{ij}, \quad \text{for} \quad i,j = 1\dots 6 \tag{4.15}$$

with δ_{ij} indicating the Kronecker delta.Equation 4.14 can be rewritten in terms of the strain tensor, resulting in:

$$T = \mathbb{D}^{-1}\tilde{T} = \mathbb{D}^{-1}\mathbb{Q} : E = \mathbb{Q}_d : E. \tag{4.16}$$

The above equation implies that $\mathbb{Q}_d = \mathbb{D}^{-1}\mathbb{Q}$, which can also be expressed in terms of the compliance tensor.

$$\mathbb{C}_d = \mathbb{Q}_d^{-1} = \left(\mathbb{D}^{-1}\mathbb{Q}\right)^{-1} = \mathbb{Q}^{-1}\mathbb{D} = \mathbb{C}\mathbb{D} \tag{4.17}$$

Compliance tensor calculation: second approach

An alternative methodology is also viable, as suggested by Maimí et al. [64]. The principles of thermodynamics pertaining to irreversible processes provide the framework for formulating the constitutive equation. This equation is derived by utilising the complementary strain energy density G^*. The scalar function representing the complementary value to the strain energy density G, i.e. $G^* = \boldsymbol{T} : \boldsymbol{E} - G$ can be visually shown on Figure 4.6.

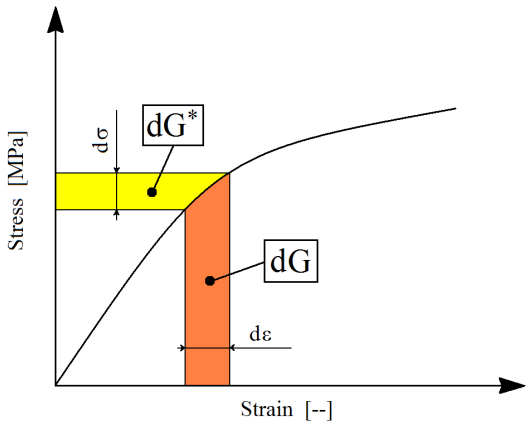


Figure 4.6: Strain energy density G and complementary strain energy density G^* for the unidirectional case

The use of the first and second laws of thermodynamics enables the assessment of the thermodynamic permissibility of a material's constitutive connection. When considering a sample elementary volume, the second law may be expressed as follows:

$$\boldsymbol{T} : \dot{\boldsymbol{E}} - \rho \left(\frac{\partial \Psi}{\partial t} + S \frac{\partial T}{\partial t} \right) - \frac{\boldsymbol{q} \cdot \nabla T}{T} \geq 0 \tag{4.18}$$

In this context, ρ represents the density of the material, Ψ denotes the thermodynamic free energy, which is defined as $\Psi = e - TS$, where e corresponds to the internal energy of the continuum. Additionally, $\boldsymbol{q}$ represents the heat flow, T represents the temperature, and S represents the entropy. When analysing an elastic material that undergoes damage processes, which contribute to the dissipation of energy, in an isothermal process, the change in thermodynamic free energy may be linked to the change in strain energy density. Consequently, it is possible to derive:

$$\boldsymbol{T} : \dot{\boldsymbol{E}} - \rho \frac{\partial \Psi}{\partial t} = T : \dot{E} - \dot{G} \geq 0 \tag{4.19}$$

Given that $G = \boldsymbol{T} : \boldsymbol{E} - G^*$, Equation 4.19 can instead be expressed in relation to the complementary strain energy density G^*.

$$\boldsymbol{T} : \dot{\boldsymbol{E}} - \dot{G} = \boldsymbol{T} : \dot{\boldsymbol{E}} - \left(\dot{\boldsymbol{T}} : \boldsymbol{T} + \boldsymbol{T} : \dot{\boldsymbol{E}} - \dot{G}^* \right) = \dot{G}^* - \dot{\boldsymbol{T}} : \boldsymbol{E} \geq 0 \tag{4.20}$$

This implies that the derivative of the complementary strain energy density with respect to a virtual variation in the stress components, minus the work done by the virtual stress components at constant strain, should not have a negative value. By

expressing the inequality in relation to the nominal stress tensor and the damage tensor, one may derive an expanded form.

$$\frac{\partial G^*}{\partial T} : \dot{T} + \frac{\partial G^*}{\partial \mathrm{D}} : \dot{\mathrm{D}} - \dot{T} : E \geq 0 \tag{4.21}$$

$$\Rightarrow \left(\frac{\partial G^*}{\partial T} - \boldsymbol{E} \right) : \dot{T} + \frac{\partial G^*}{\partial \mathbb{D}} : \dot{\mathbb{D}} \geq 0. \tag{4.22}$$

The constitutive relation of the material can be derived using a chosen function G^* that fulfils two conditions: $\partial G^*/\partial \mathbb{D} \geq 0$ and $\partial G^*/\partial \boldsymbol{T} = E$. These conditions ensure that the constitutive relation is consistent with the principles of the first and second laws of thermodynamics, as the stress components are allowed to vary freely. Furthermore, the second condition specifies that the strain tensor E is determined by taking the derivative of the complementary strain energy density G^* with respect to the stress components:

$$\frac{\partial G^*}{\partial T} = E \tag{4.23}$$

Through manipulation, Longo [116] arrived at the specific element of the compliance tensor for the damaged material can be expressed as:

$$[\mathbb{C}_d]_{ij} = \left[\frac{\partial^2 G^*}{\partial \sigma_i \partial \sigma_j} \right] \tag{4.24}$$

4.2.3 3D stiffness tensor of the damaged model

The 3-dimensional damage model focuses on the analysis of plane stress behaviour, which is a reasonable assumption for thin laminae. No consideration has been given to damage in the through-the-thickness direction and in the out-of-plane components of shear, specifically denoted as $d_3 = d_5 = d_6 = 0$. The compliance tensor of the damaged material, denoted as $\mathbb{C}_d$, may be determined by employing either the concept of strain equivalence or the thermodynamic technique. By adopting the aforementioned methodology and excluding any factors pertaining to temperature and moisture, the complementary strain energy density G^* may be expressed as:

$$\begin{aligned} G^* = & \frac{\sigma_{11}^2}{2E_1^0\,(1-d_1)} + \frac{\sigma_{22}^2}{2E_2^0\,(1-d_2)} + \frac{\sigma_{33}^2}{2E_3^0} - \frac{\nu_{12}^0 \sigma_{22}\sigma_{11}}{E_1^0} - \frac{\nu_{13}^0 \sigma_{33}\sigma_{11}}{E_1^0} - \\ & - \frac{\nu_{23}^0 \sigma_{22}\sigma_{33}}{E_2^0} + \frac{\tau_{12}^2}{2G_{12}^0\,(1-d_4)} + \frac{\tau_{13}^2}{2G_{13}^0} + \frac{\tau_{23}^2}{2G_{23}^0}. \end{aligned} \tag{4.25}$$

When G^* is derived twice with respect to the stress components, the lamina compliance tensor can be obtained and afterwards, the stiffness tensor Q_d can be calculated inverting $\mathbb{C}_d$ as follows:

$$\mathbf{Q}_d = \begin{bmatrix} \frac{1}{(1-d_1 E_1^0} & -\frac{\nu_{21}^0}{E_2^0} & -\frac{\nu_{91}^0}{E_3^0} & 0 & 0 & 0 \\ -\frac{\nu_{12}^0}{E_1^0} & \frac{1}{(1-d_2)E_2^0} & -\frac{\nu_{32}^0}{E_3^0} & 0 & 0 & 0 \\ -\frac{\nu_{13}^0}{E_1^0} & -\frac{\nu_{23}^0}{E_2^0} & \frac{1}{E_3^0} & 0 & 0 & 0 \\ 0 & 0 & 0 & \frac{1}{(1-d_4)G_{12}^0} & 0 & 0 \\ 0 & 0 & 0 & 0 & \frac{1}{G_{13}^0} & 0 \\ 0 & 0 & 0 & 0 & 0 & \frac{1}{G_{23}^0} \end{bmatrix}^{-1} \tag{4.26}$$

4.2.4 Intralaminar damage evaluation strategy

It was essential to establish a technique for determining the damage variables d_i, which are employed to modify the entries of the stiffness tensor of the damaged material $\mathbb{Q}_d$ at each time increment throughout the non-linear analyses. Hence, the methodology consisted of [116]:

- A non-linear analysis is conducted at each time increment to consider the geometric and material non-linearities inherent in the construction.
- Abaqus/Standard endeavours to implement the new time increment, commencing from the equilibrium state at time k. The strain tensor E is evaluated at every integration point of the finite element model in Abaqus/Standard.
- The sub-routine UMAT is used at every integration point to calculate the effective stress tensor $\tilde{T}$. This is done by using the original stiffness tensor $\mathbf{Q}$ of the undamaged material, so that $\tilde{T}$ is equal to the contraction of $\mathbb{Q}$ and the strain tensor E.
- The damage initiation check is executed within the UMAT procedure. In the absence of recognised material damage initiation, its reaction stays in a state of linear elasticity, wherein the nominal stress tensor T is equivalent to the effective stress tensor. In the event that the initiation of material damage is identified, the properties undergo degradation through deterioration of the stiffness tensor $\mathbb{Q}$ components. Subsequently, the nominal stress tensor is determined by evaluating $\boldsymbol{T} = \mathbb{Q}_d : \boldsymbol{E}$.
- Subsequently, Abaqus/Standard assesses if the convergence conditions have been met. If the residual force R_n is below a certain tolerance, it indicates that the equilibrium state for the $(k+1)$ time increment has been achieved, signifying the completion of the analysis and readiness for the subsequent time increment. In the event that the force residual exceeds the specified tolerance, Abaqus/Standard will discard the previous time increment and initiate a new iteration with a reduced time increment compared to the previous one.

- The non-linear analysis proceeds until the structure collapses.

The details of the implemented progressive failure procedure are shown in Figure 4.7.

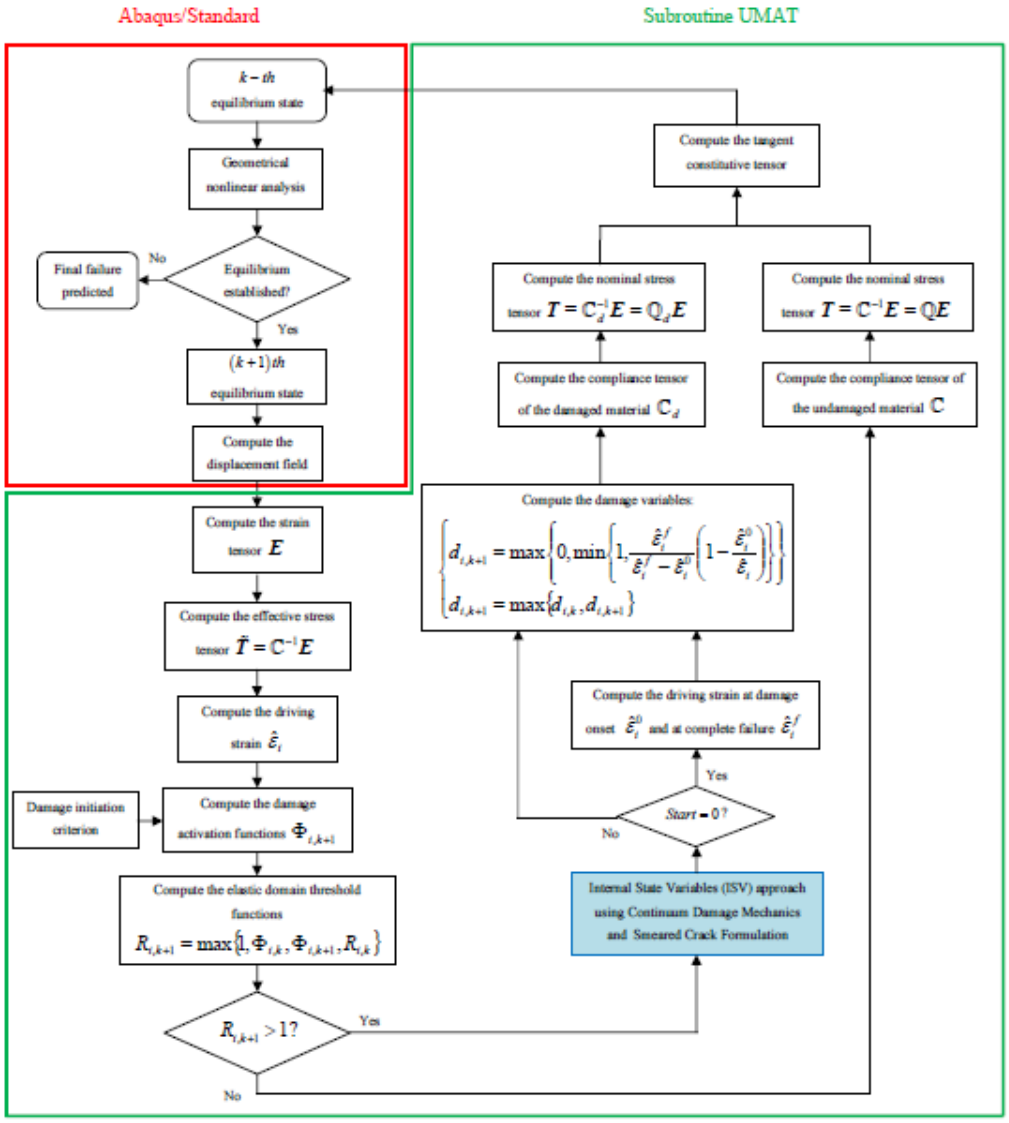


Figure 4.7: Details of the implemented progressive failure procedure [116].

This sub-routine UMAT requires the computation of the stiffness tensor as well as the Jacobian tensor of the constitutive model, $\left[\frac{\partial T}{\partial E}\right]$. The aforementioned defines the change in the $i-th$ stress component at the end of the time increment and its obtained by deriving $\boldsymbol{T} = \mathbb{Q}_d : \boldsymbol{E}$, yielding:

$$\left[\frac{\partial \boldsymbol{T}}{\partial \boldsymbol{E}}\right] = \mathbb{Q}_d + \left[\frac{\partial \mathbb{Q}_d}{\partial \boldsymbol{E}}\right] : \boldsymbol{E}. \tag{4.27}$$

The presented equation can be manipulated as in order to arrive at the following format:

$$\frac{\partial \sigma_{ij}}{\partial \epsilon_{\alpha\beta}} = \frac{\partial}{\partial \epsilon_{\alpha\beta}} \left[[\mathbb{Q}_d]_{ijhk} \, \epsilon_{hk} \right] = [\mathbb{Q}_d]_{ij\alpha\beta} + \left[\frac{\partial \, [\mathbb{Q}_d]_{ijhk}}{\partial \epsilon_{\alpha\beta}} \epsilon_{hk} \right] \tag{4.28}$$

Ergo, Longo [116] applied the chain rule for derivatives, taking into account that the generic damage variable in the $n-th$ direction is a function of the driving strain component in that specific orientation, obtaining Equation 4.29 and Equation 4.30.

$$\frac{\partial \sigma_{ij}}{\partial \epsilon_{\alpha\beta}} = [\mathbb{Q}_d]_{ij\alpha\beta} + \sum_{h,k=1}^{3} \left[\sum_{n=1}^{6} \frac{\partial \, [\mathbb{Q}_d]_{ijhk}}{\partial d_n} \frac{\partial d_n}{\partial \hat{\epsilon}_n} \frac{\partial \hat{\epsilon}_n}{\partial \epsilon_{\alpha\beta}} \right] \cdot \epsilon_{hk} \tag{4.29}$$

$$\Rightarrow \quad \frac{\partial \sigma_{ij}}{\partial \epsilon_{\alpha\beta}} = [\mathbb{Q}_d]_{ij\alpha\beta} + \sum_{n=1}^{6} \left\{ \left[\sum_{h,k=1}^{3} \frac{\partial \, [\mathbb{Q}_d]_{ijhk}}{\partial d_n} \epsilon_{hk} \right] \left(\frac{\partial d_n}{\partial \hat{\epsilon}_n} \frac{\partial \hat{\epsilon}_n}{\partial \epsilon_{\alpha\beta}} \right) \right\} \tag{4.30}$$

Following the assessment of the stiffness tensor of the damaged material, $\mathbb{Q}_d$, and the tangent constitutive tensor, the tangent constitutive tensor is calculated. The nominal stress tensor $\boldsymbol{T}$, and damage variables are output by the sub-routine UMAT. Therefore, the $(k+1)th$ equilibrium state is fully defined, and Abaqus/Standard can proceed with a new time increment until the structure collapses.

4.2.5 Intralaminar damage modes: Fibre Fracture (FF)

Longitudinal tensile damage model

In the UMAT implemented, the tensile load is predicted using a non-interactive strain-based failure criterion, i.e., the following longitudinal tensile damage activation function,

$$\Phi_{1T} = \left(\frac{E_1^0}{X_T} \epsilon_{11} \right)^2, \quad \epsilon_{11} \geq 0 \tag{4.31}$$

here X_T refers to the longitudinal tensile strenght. Damage starts to grow when the function Φ_{1T} reaches the unity value and the material degrades. Thus, the softening law is a linear law, expressed as follows, in which the driving strain component is defined as $\hat{\epsilon}_1 = \epsilon_{11}$.

$$d_{1T} = \max_t \left\{ 0, \min_t \left\{ 1, \frac{\hat{\epsilon}_1^f}{\hat{\epsilon}_1^f - \hat{\epsilon}_1^0} \left(1 - \frac{\hat{\epsilon}_1^f}{\hat{\epsilon}_1} \right) \right\} \right\}, \tag{4.32}$$

Longitudinal compressive damage model

The failure of fibres under compressive loading is characterised by kinking of the aforesaid, which then collapse and ultimately fail. In this study, a strain-based damage initiation criterion is selected, whose damage activation function has the same form as in the case of tensile damage:

$$\Phi_{1C} = \left(\frac{E_1^0}{X_C} \epsilon_{11} \right)^2, \quad \epsilon_{11} < 0, \tag{4.33}$$

where X_C is the transverse compressive strength. Similar to the longitudinal tensile case, when Φ_{1C} reaches a value equal to one, damage increases and material degradation commences. The material softening is defined by the following linear law:

$$d_{1C} = \max_t \left\{ 0, \min_t \left\{ 1, \frac{\hat{\epsilon}_1^f}{\hat{\epsilon}_1^f - \hat{\epsilon}_1^0} \left(1 - \frac{\hat{\epsilon}_1^f}{\hat{\epsilon}_1} \right) \right\} \right. \tag{4.34}$$

with the driving strain component defined as $\hat{\epsilon}_1 = |\epsilon_{11}|$.

4.2.6 Intralaminar damage modes: inter fibre fracture (IFF)

Transverse tensile damage mode

The constitutive law for tensile damage activation in this sub-routine is as follows:

$$\Phi_{2T} = \left(\frac{\tilde{\sigma}_{22}}{Y_T} \right)^2 + \left(\frac{\tilde{\tau}_{12}}{S_L} \right)^2 + \left(\frac{\tilde{\tau}_{23}}{S_T} \right)^2, \quad \tilde{\sigma}_{22} \geq 0 \tag{4.35}$$

where Y_T is the transverse tensile strength, S_L is the in-plane shear strength and S_T is the transverse shear strength. As previously stated, damage begins when this function achieves the unity value and follows the softening law - Equation 4.36.

$$d_{2T} = \max_t \left\{ 0, \min_t \left\{ 1, \frac{\hat{\epsilon}_2^f}{\hat{\epsilon}_2^f - \hat{\epsilon}_2^0} \left(1 - \frac{\hat{\epsilon}_2^f}{\hat{\epsilon}_2} \right) \right\} \right\} \tag{4.36}$$

with the driving strain component defined as $\hat{\epsilon}_2 = \sqrt{\langle \epsilon_{22} \rangle^2 + \gamma_{12}^2 + \gamma_{23}^2}$.

Transverse compressive damage mode

Typically, failure in transverse compression is caused by matrix fracturing. Experimental evidence suggests that the fracture is caused by stresses acting on a typical fracture plane inclined by $\theta_{fp} = 53\circ$ in regard to the direction of the material's thickness. Thus, the stresses operating on the inclined fracture plane are obtained using a transformation matrix:

$$\begin{cases} \sigma_n = \tilde{\sigma}_{22}\cos^2\theta_{fp} + \tilde{\sigma}_{33}\sin^2\theta_{fp} + 2\tilde{\tau}_{23}\cos\theta_{fp}\sin\theta_{fp} \\ \tau_{nl} = \tilde{\tau}_{12}\cos\theta_{fp} + \tilde{\tau}_{13}\sin\theta_{fp} \\ \tau_{nt} = (\tilde{\sigma}_{33} - \tilde{\sigma}_{22})\cos\theta_{fp}\sin\theta_{fp} + \tilde{\tau}_{23}\left(\cos^2\theta_{fp} - \sin^2\theta_{fp}\right) \end{cases} \tag{4.37}$$

Since tensile stress $\sigma_n \geq 0$ fosters crack opening while compressive stress $\sigma_n \leq 0$ inhibits shear fractures, Falzon [117] and Puck [59] concluded that for $\sigma_n < 0$ the shear stresses must cause fracture against an additional resistance, which raise the already increasing $|\sigma_n|$ similar to internal friction. Based on the aforementioned factors, the activation function for transverse compressive damage is determined using a stress-based calculation.

$$\Phi_{2C} = \left(\frac{\tau_{nt}}{Y_C - \mu_T\sigma_n}\right)^2 + \left(\frac{\tau_{nt}}{Y_C/\left(2\tan\theta_{fp}\right) - \mu_L\sigma_n}\right)^2, \quad \tilde{\sigma}_{22} < 0, \quad \sigma_n < 0 \tag{4.38}$$

where Y_C is the transverse compressive strength and the friction coefficients are given by the following equations:

$$\mu_T = \frac{1}{\tan\left(2\theta_{fp}\right)}, \quad \mu_L = \frac{\mu_T}{2Y_C\tan\theta_{fp}} \tag{4.39}$$

To conclude, when the function arrives at the unity value, degradation begins and follows the presented law:

$$d_{2C} = \max_t\left\{0, \min_t\left\{1, \frac{\hat{\epsilon}_2^f}{\hat{\epsilon}_2^f - \hat{\epsilon}_2^0}\left(1 - \frac{\hat{\epsilon}_2^f}{\hat{\epsilon}_2}\right)\right\}\right\} \tag{4.40}$$

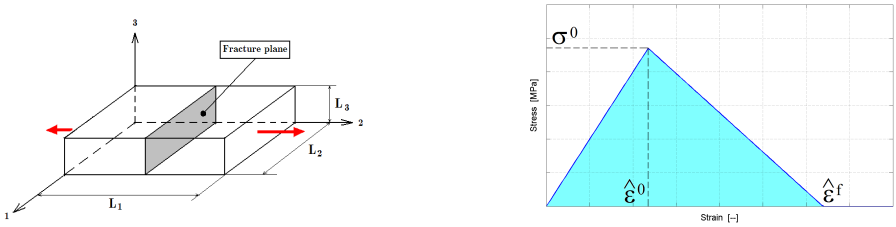
Here, the driving strain component which defines the damage evolution law is given by $\hat{\epsilon}_2 = \sqrt{\gamma_{nl}^2 + \gamma_{nt}^2}$. Therefore, the analysis only focuses on the shear strain components inside the fracture plane when examining the transverse compressive damage mode. The components of shear strain may be determined by evaluating:

$$\begin{cases} \gamma_{nl} = \gamma_{12}\cos\theta_{fp} + \gamma_{13}\sin\theta_{fp} \\ \gamma_{nt} = (\epsilon_{33} - \epsilon_{22})\cos\theta_{fp}\sin\theta_{fp} + \gamma_{23}\left(\cos^2\theta_{fp} - \sin^2\theta_{fp}\right) \end{cases} \tag{4.41}$$

4.2.7 In-plane shear damage mode

Due to simplicity purposes, the non-linear behaviour of the in-plane shear response is not present in the sub-routine implemented. Despite this, two material degradation procedures were defined [116].

The first method takes into account the in-plane shear damage mechanism, which is influenced by the damage processes in the longitudinal and transverse planes. Therefore, the activation function for shear damage, denoted as ϕ_4, is undefined. This implies that the initiation of shear damage occurs only via the occurrence of



(a) Elementary volume

(b) Bilinear constitutive law of material

Figure 4.8: RVE loaded along the 2-direction and subsequent law [116].

fibre breakages. The phenomenon of matrix cracking is seen to occur in the below manner:

$$d_4 = 1 - (1 - d_1)(1 - d_2). \tag{4.42}$$

The second technique does not take into account the shear damage variable as a straightforward function of d_1 and d_2. Instead, it incorporates a shear damage activation function and a bilinear shear softening law. The activation function for in-plane shear damage is expressed by a stress-based connection that is straightforward in nature.

$$\Phi_4 = \frac{|\bar{\tau}_{12}|}{S_L} \tag{4.43}$$

When the value of phi_4 hits unity, the damage starts an increase and the material undergoes degradation. The variable d_4, which represents damage, may likewise be triggered by the transverse direction damage d_2.

$$\begin{cases} d_4 = (1 - d_4^*)(1 - d_2) \\ d_4^* = \max_t \left\{0, \max_t \left\{1, \frac{\hat{\gamma}_{12}}{\hat{\gamma}_{12} - \hat{\gamma}_{12}^0}\left(1 - \frac{\hat{\gamma} f_2}{\hat{\gamma}_{12}}\right)\right\}\right\} \end{cases} \tag{4.44}$$

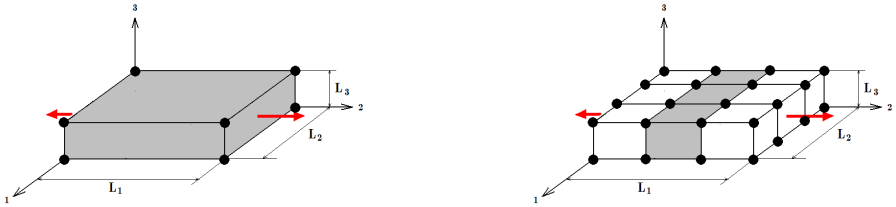
where the driving strain is defined as $\hat{\gamma}_{12} = |\gamma_{12}|$.

4.2.8 Smeared crack formulation

Longo [116] considered a flawed continuum exposed to a certain loading condition. The Griffith energy criteria for fracture postulates that the propagation of a crack is possible when the energy needed to create a new crack segment of length d_a can be precisely supplied by the system via the release of elastic energy.

After highlighting that the energy release rate is dependent on the mesh density, Longo extracted an example from Pinho et al.[118] and Pasi [119] that better explains the problem. Ergo, we shall consider a RVE of composite material ($V = L_1 L_2 L_3$) loaded in tension along the 2-direction, as shown in Figure 4.8.

The energy absorbed by the elementary volume for a complete fracture is:



(a) Single solid element (b) Nine solid elements

Figure 4.9: Possible mesh densities for the composite RVE [116].

$$U = L_1 L_2 L_3 \frac{\sigma^0 \hat{\epsilon}^f}{2} \tag{4.45}$$

The above RVE can be modelled numerically by means of distinct mesh densities, as seen in Figure 4.9.

The energy required to create the hole fracture plane across the defined volume V must be equal for both cases (a) and (b) and match Equation 4.45. Nonetheless, the dissipated energy assessed by a finite element analysis is distinct in the two cases.

$$\begin{aligned} R_a &= L_1 L_2 L_3 \frac{\sigma^0 \hat{\epsilon} f}{2} \\ R_b &= \frac{L_1}{3} L_2 L_3 \frac{\sigma^0 \hat{\epsilon}^f}{2} \end{aligned} \tag{4.46}$$

The observed outcome may be attributed to the circumstance that, in the instance of (b), only three components are involved in the damage process, while the other six elements do not contribute to energy dissipation. This phenomenon leads to the paradoxical observation that as the mesh becomes finer, the amount of energy required to generate the whole fracture plane decreases. Considering this perspective, Longo [116] implemented the smeared crack formulation as it is one of the most straightforward approaches to guarantee the objective response of the overall finite element model. This approach addresses the issue of mesh dependence.

One crucial factor to take into account is the amount of energy absorbed by the Representative Volume Element (RVE) in order to achieve a full fracture. This energy per unit area, denoted as G, is a material attribute often referred to as intralaminar fracture toughness. The total energy absorbed is determined by multiplying G by the fracture area, $L_2 L_3$.

$$U = L_2 L_3 G. \tag{4.47}$$

Furthermore, as shown by Iannucci [120], the less the characteristic length,the bigger the strain at complete failure $\hat{\epsilon}^f$ - Figure 4.10.

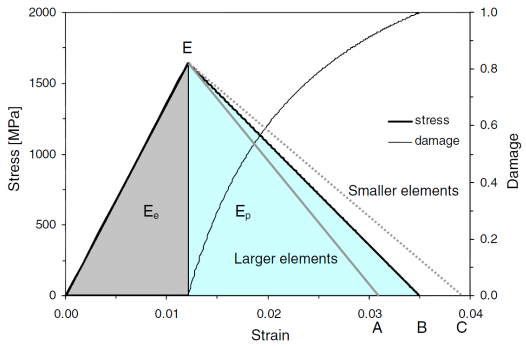


Figure 4.10: Energy dissipation as function of element size [120]

All in all, the smeared crack formulation, despite its rudimentary nature, is the most straightforward approach to address the issue of mesh size dependence. By using this particular methodology, the damage is confined to a specific region that is characterised by a single element in height. Consequently, optimal outcomes may be achieved when the precise position of the damage is known, as it enables the construction of a mesh that is tailored to accommodate the damage appropriately.The user did not provide any text to rewrite. When a well defined damage route is not established, it is often advisable to choose a non-local technique. [121], [122] However, the smeared crack formulation remains applicable, provided that a certain degree of approximation is accepted.

Chapter 5

Skin-stringer validation

5.1 Experimental Data

In order to verify the data retrieved from the FE model, it is crucial to analyse an experimental case to fully understand the best way to model the specimen. Thus, Orifici et al. [98] analysed a similar panel to that presented in Figure 3.6, whose dimensions are shown in Table 5.1.

Table 5.1: Dimension of the panel [mm] [98].

Parameter	**D1**
Total length, L	400
Free length, L_f	300
Width, b	64
Skin lay-up	$[90, \pm 45, 0]_s$
Stiffener lay-up	$[(\pm 45)_3, 0_6]_s$
Material	IM 7/8552UD
Adhesive	FM 300
Ply thickness, t	0.125
Stiffener height, h	14
Stiffener width, w	32
Debond length, d (debonded panels)	80
Adhesive thickness, t_{adh}	0.2

Thus, as part of a research project, two different configurations of the skin-stringer system were tested to as fuselage-representative panels. These designs found in the literature were tested in undamaged (intact) and pre-damaged (debonded) configurations. The latter was achieved by replacing the adhesive with a layer of Teflon placed across the width of the stiffener. In order to achieve an uniform distribution of the applied load, the panels were enclosed in potting. The D1 panels buckled under compression in an eight-buckling half-sine wave pattern, collapsing due to ply degradation at the loaded or clamped ends. Both panels collapsed explosively, and the damaged panels indicated a variety of flaws, including matrix cracking and delamination along the skin-stiffener interface and fibre fracture in the stringer. Nonetheless, ply damages developed instantly, making it impossible to predict how the harm would continue [98].

For the debonded specimen, after collapse, Orifici et al. [98] used one panel to investigate the fracture propagation in the skin-stringer interface. To assess the degree of debonding at the this region, ultrasonic scans of the collapsed panels were performed. After cutting the panel into portions around the debond growing zones, the skin and stiffener were separated, and the bonded interface was visually evaluated. The skins separated off the flange under compression stress in a single half wave that encompassed the flange's entire width. The amount of flange buckling varied depending on the design. For example, D1 panels provided largely symmetrical flange buckles made up of single half waves that buckled away from the skin. Collapse was defined by fibre fracture and delamination in the interface between parts and matrix cracking in the flange, stiffener and skin [98].

The intact panels noted a maximum load of 55kN and a failure around 1.6mm whilst, for the debonded specimens, it was observed that initial stiffness degradation occurred around the displacement of 1.2mm, leading to the final collapse close to 2mm. The panels supported a peak load of 30kN prior to 1.2mm [98].

5.2 Finite Element Model Validation

5.2.1 Material properties

Carbon-fibre reinforced polymer

Following the analysis conducted by Orific et al. [98], the CFRP simulated in Abaqus was the IM7/8552 carbon/epoxy unidirectional tape, whose mechanical properties are shown in Table 5.2. Since the FE analysis consisted of a Dynamic step, it was necessary to implement the density of the composite material in the software. This can depend on many aspects, although, following the literature, the density chosen for the plies was 1.77E-06 kg/cm^3, as defined in [123]. Finally, for the Benzeggah and Kenane (BK) law, a $B-K$ coefficient, η of 1.2 was introduced to the software.

Table 5.2: Material properties for IM7/8552 carbon/epoxy unidirectional tape [98], [124]–[132].

Stiffness property	**Value**	**Fracture property**	**Value**
E_{11}(GPa)	147.0	X_T (MPa)	2625
E_{22}(GPa)	11.8	X_C (MPa)	1451
E_{33}(GPa)	11.8	Y_T (MPa)	60.2
υ_{12}	0.32	Y_C (MPa)	248.7
υ_{13}	0.32	S_{12} (MPa)	112.7
υ_{32}	0.435	G_{IT} (N/mm)	120.0
G_{12}(GPa)	6.0	G_{IC} (N/mm)	101.0
G_{23}(GPa)	4.0	G_{IIT} (N/mm)	0.66
G_{31}(GPa)	6.0	G_{IIC} (N/mm)	0.922

Adhesive and Cohesive Elements

The adhesive between the skin and stringer was modelled using cohesive elements in Abaqus. As explained, the behaviour for this section of the model must be defined as Traction with the Quadratic Nominal Stress Criteria. This makes necessary to introduce into the software the strength and fracture toughness parameters, summarized in Table 5.3. Finally, for the FM 300 adhesive, Ong et al. [133] measured a density of 1.317E-06 kg/cm^3, being this value the one used throughout this thesis.

Table 5.3: Material data for cohesive elements [89].

Cohesive element properties	**Value**
Interface element stiffness before the damage onset, K (N/mm^3)	10^6
Interfacial strength, mode I, τ_I(MPa)	61
Interfacial strength, mode II and III, τ_{II}, τ_{III}(MPa)	68
Fracture toughness, mode I, G_{Ic}(N/mm)	0.243
Fracture toughness, mode II and III, G_{IIc}, G_{IIIc}(N/mm)	0.514
Viscosity stabilization coefficient	0.001

Stringer filament

To conclude, since the stringer has an adhesive filament in the cross-section, as observed in Figure 5.1.

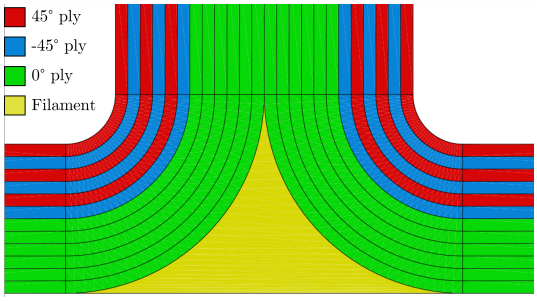


Figure 5.1: Local model of the stiffener with ply orientations.

Here, it should be considered different material properties from the plies and, since the purpose of this analysis is to detect delamination in the interface and material cracks in the laminates, this region should be considered elastic throughout the entire simulation. Thus, the density is the same of the adhesive layer between the skin and stiffener (1.317E-06 kg/cm^3) and the elastic properties are presented in Table 5.4.

Table 5.4: Elastic filament material properties.

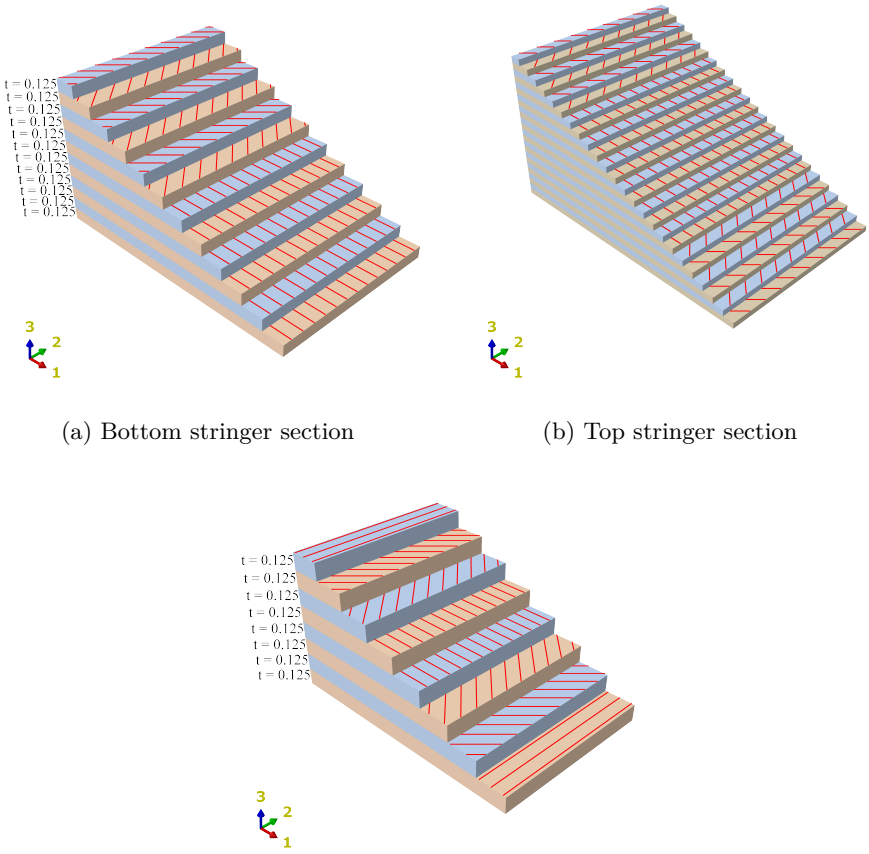
Property	**Value**
Young's Modulus, E (MPa)	1000
Poisson's ratio, υ	0.3

5.2.2 Global model

A finite element model using Python scripting, was developed employing shell elements to simulate the behaviour of the complete skin-stringer system. The primary objective of this model was to determine nodal displacements, which could then

be utilized in the local model. In order to strike a balance between computational efficiency and accuracy, the model was optimized meticulously.

The individual parts were represented using two-dimensional 4-node S4R shell elements with reduced integration. To accurately define the composite region, the Composite Layup feature in Abaqus was employed, paying particular attention to establishing the correct normal orientations, especially between the bottom and top sections of the stringer. These orientations can be visualized in Figure 5.2.



(a) Bottom stringer section

(b) Top stringer section

(c) Skin specimen

Figure 5.2: Ply stack definition.

For the assembly, a simple "Tie" option in Abaqus was used to connect the two parts. However, for the debonded analysis, the tie was removed in the region where the Teflon layer was positioned. Regarding the boundary conditions, the potting effect was simulated by applying a BC restricting every degree of freedom except longitudinal displacement, while the edge was subjected to a compressive displacement of 2mm, following experimental procedures, as observed in Figure 5.4. A Smooth Amplitude step was implemented, which proved to be extremely beneficial when compared to the first analysis conducted with the standard Ramp amplitude- shown in Figure 5.3.

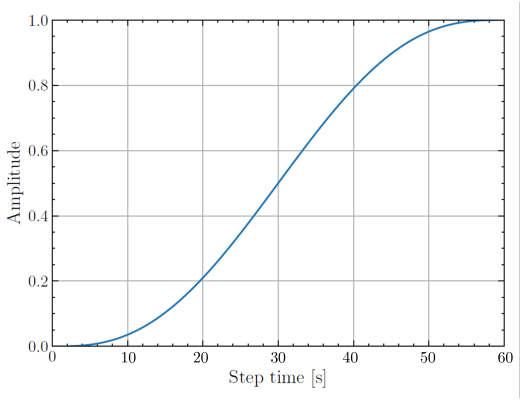


Figure 5.3: Smooth step implemented for the boundary conditions

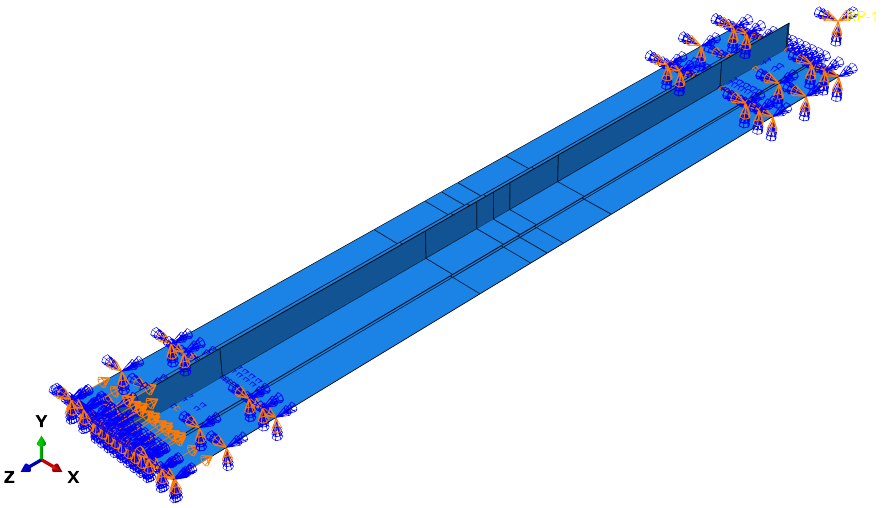


Figure 5.4: Boundary conditions implemented.

A mesh sensitivity study was conducted, which concluded that an element size of 2 mm provided the most accurate results. This choice yielded a total of 11.110 shell elements in the global model.

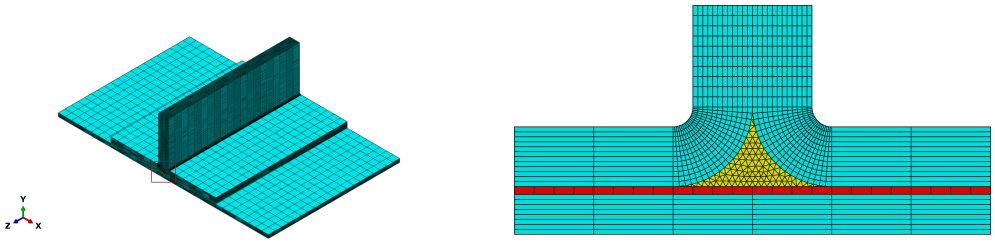
Finally, a Static, General step was implemented with a time period of 60 seconds and a minimal increment of 1E-10. Since this is just a simple linear elastic analysis, and, therefore, it is vital that these procedures is as simple and as fast as possible. Given the simplicity and computational efficiency of the model, the step chosen proved to be sufficient. However, it was also crucial to consider the parameters for the local step, which proved to be more complex and significant. In the shell-to-solid submodelling technique, ensuring equal time discretization for both the global and local models was imperative. This emphasizes the need to strike a delicate balance between computational efforts and the overall analysis results, striving for an optimal combination.

5.2.3 Local Models

Focusing now on the solid models, based on the crucial regions found during the global analysis, local model locations were identified. The skin and flange of the stringer where the debonding is anticipated to occur are represented by local models.

Here, the skin and stringer are modelled with 8-nodes C3D8 linear solid elements. For the adhesive layer, it was computed with cohesive elements with non-zero thickness (COH3D8) and quadratic traction-separation law. The in-plane length of the local element is 2 mm, as preliminary mesh convergence studies verified it to be optimal for this system panel, whilst the out-of-plane length is 0.125mm, resulting in one element per lamina in the thickness direction.

Furthermore, two main adversities arose while computing the local models, the filament mesh density and the cohesive element size. For the former, an element size of 0.15 mm was determined to be the smaller possible element that did not increase complexity and computational costs and, as this section is directly connected to the adhesive layer, this value was found to be accurate. For the latter, following Akterskaia et al. [89], a number of 4 cohesive elements per solid element was implemented, resulting in an element size of 0.50 mm - Figure 5.5.



(a) Full local model. (b) Local model close-up.

Figure 5.5: 3D local model.

As for the BCs, the submodelling technique in Abaqus was adopted, specifying that the (global) shell model drives the (local) solid model. Thus, as this tool in Abaqus requires improvements, thickness discretization was impossible to implement, i.e., applying various submodel boundary conditions to either the skin or the stringer's web and flange was impassable.

Nonetheless, after further investigation, it was determined that applying a single sub-model boundary condition to each region of the local stringer with the respective thickness -Figure 5.6 - and increasing the exterior tolerance of 10% was an accurate and effective technique as for the nodal displacement transfer from the global to the local model. Since this model was directly dependent on the global analysis, it was fundamental to use the same analysis type as the global model, in order to assure low computational costs.

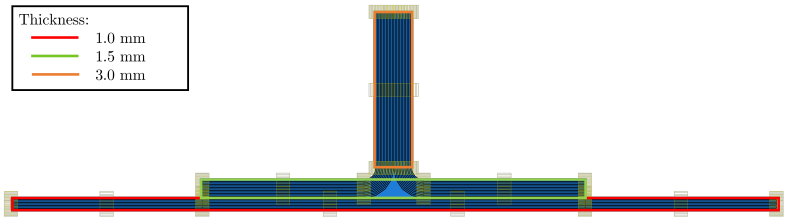
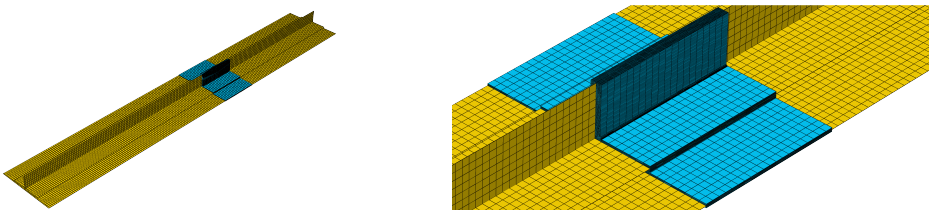


Figure 5.6: Sub-modelling boundary conditions.

Thus, since in this model, cohesive elements suffer softening and eventually are deleted, the Static, General step cannot be applied. Hence, this left us with two options, either Implicit or Explicit Dynamic analysis. Here, the decision was to implement a Dynamic, Implicit step, with a time period of 60 seconds and a minimal increment of 1E-10, as it is better for convergence in a quasi-static delamination analysis. This choice was also backed by the fact that an previously tested material sub-routine, as proved in [116] was introduced, in order to determine intralaminar failure and it was verified for the Dynamic, Implicit step.

To conclude, after assuring that the Assembly was accurately made and that the local model was in the correct location of the interface between models, the final model combination can be observed in Figure 5.7.



(a) Full global-local models. (b) Interface close-up.

Figure 5.7: Final global-local models.

Chapter 6

Numerical results

In the present section we delve into the results extracted from each analysis. We first start by assessing the credibility of the global model by investigating the displacement field, stress distribution and load-displacement curve. After validating this step, we move into the solid model, maintaining the same line of thought and complementing it with the study of the delamination propagation.

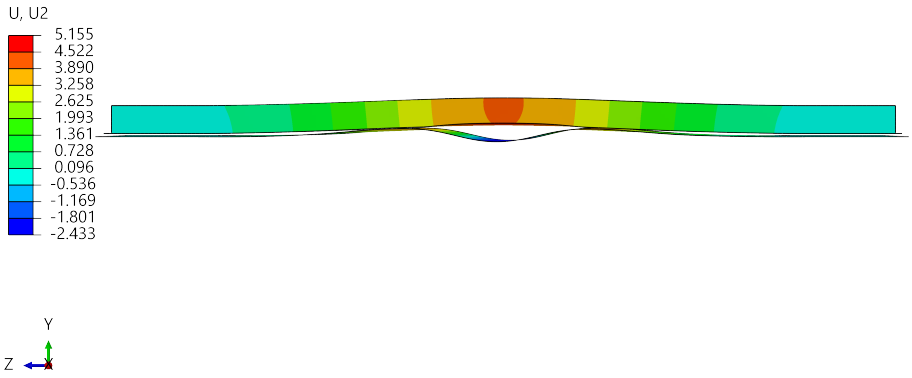
6.1 Global analysis

The global analysis results, presented in this section, marks a pivotal juncture in our exploration of the structural behaviour under scrutiny. This phase is instrumental in unravelling the intricate interplay between external forces and the system's response, providing a macroscopic understanding of the structural integrity.

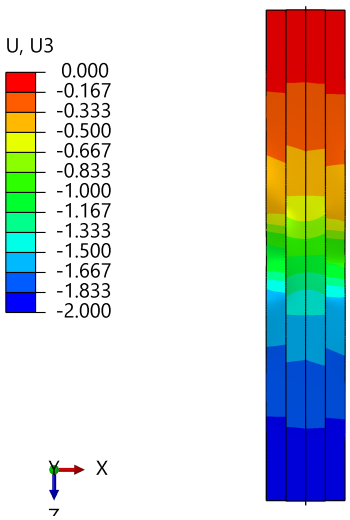
The global analysis stage encapsulates the initial step in this process, offering a panoramic view of the structural response to applied displacement, a view which is instrumental in guiding engineering decisions and ensuring the realistic structural response. Therefore, this model is crucial to validate the material properties, since they have been determined from the literature, and, more importantly, determine the critical regions for delamination to further move to the local model.

6.1.1 Displacement Field

Insights into the deformation of the structure resulting from the imposed displacement may be obtained from Figure 6.1. The examination of deformation plays a crucial role in evaluating the structural integrity and verifying that the deformations remain below acceptable thresholds.



(a) Displacement field along the y-axis direction.



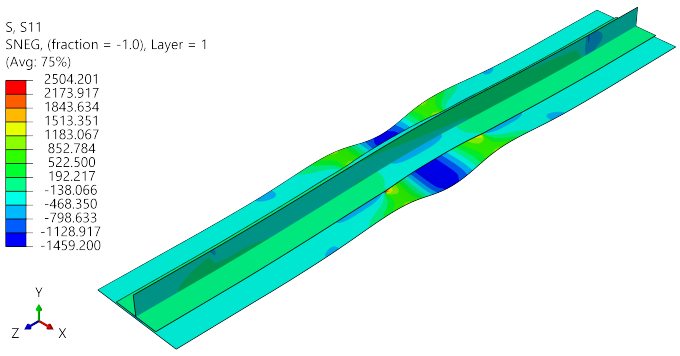
(b) Displacement field along the z-axis direction.

Figure 6.1: Deformation overview of the static model.

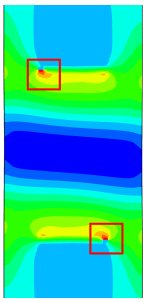
One important aspect to highlight is, as proved experimentally, both the skin and the stringer buckle towards opposite directions, as shown in Figure 6.1a. Furthermore, the displacement in the longitudinal direction shows to be distributed as expected, existing a concentration in the region between the imposed boundary condition and the debonded region- Figure 6.1b.

6.1.2 Stress Distribution

The normal stress contour along the x-axis direction plot (Figure 6.2a) illustrates the distribution of stress within the analysed structure. The simulation was subjected to a displacement of 2 millimmeters applied at one edge, in the negative z-direction. Stress distribution is a critical factor in understanding potential failure points and assessing the material's capacity to withstand loads.



(a) Full normal stress distribution along the x-axis of the global shell model.



(b) Critical region close-up.

Figure 6.2: Normal stress along the x-axis distribution of the static model.

As shown in Figure 6.2, the red regions indicate high-stress concentrations, while blue regions represent lower-stress areas. The highest stress concentration occurs near start of the Teflon layer, as expected, highlighted in red in Figure 6.2b. The maximum S11 stress in the structure reaches 2504 MPa at this location.

This high-stress concentration near the point of load application warrants close attention, as it could be indicative of potential failure. It is crucial to analyse this area further in the local analysis to gain a deeper understanding of the localized stress behaviour. It is expected that the delamination will commence on that region and, thus, it will be the focus of the local models.

6.1.3 Reaction Forces

To conclude, the final key aspect necessary for verifying the reliability of shell model is the load-displacement curve, as observed in Figure 6.3.

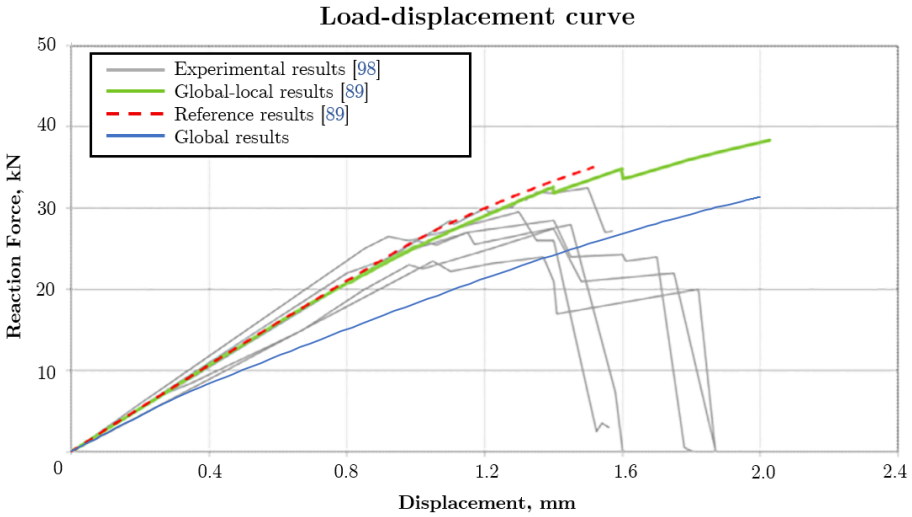


Figure 6.3: Load-displacement curves of global analysis for debonded panel D1 with comparison to experimental and numerical results extracted from literature [89].

By carefully analysing the curve above, it is possible to observe that the behaviour of the system follows the experimental results. Nonetheless, it is notary that no drops are observed, due to the fact that this analysis conducted does not account for any failure mechanisms, i.e., is a elastic analysis of the skin-stringer parts. Compared to the global-local results, extracted from Akterskaia et al. [89], the final reaction force is approximately 20% lower than the expected from the global-local analysis.

Despite this, when comparing the results to the experimental values, it is possible to observe an improvement in credibility. Around the displacement where the tested specimens begin, i.e., around 1.4mm, the reaction force of the developed global model fall around the experimental results.

All in all, it can be defined that this simulation is well-defined and a good base for the one-way global-local methodology studied throughout this process. The difference in stiffness when compared to the experimental results is attributed to the simplicity of the model when it comes to the non-linear behaviour of the material. However, due to the fact that the aeronautical industry safety driven, these results prove to be more conservative and account for a safer component. Focusing on the computational time, this model required a total of 300.70 seconds of CPU time, in an 8 CPU computer, an extremely satisfactory value when it comes to the global analysis.

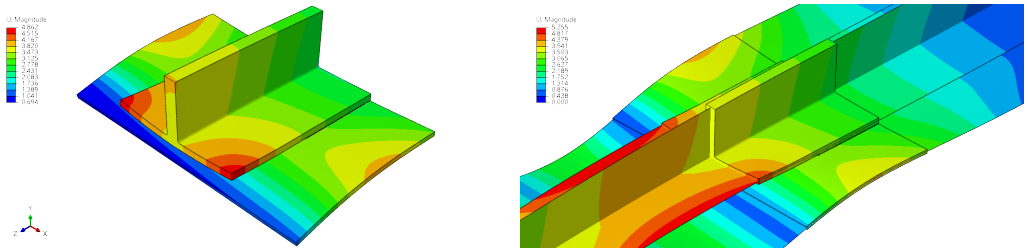
6.2 Local Results

The analytical findings pertaining to the solid components inside the local area, as reported in this part, have significant importance within our thorough investigation of the structural system being studied. Expanding upon the fundamental knowledge acquired via the comprehensive global analysis, the subsequent phase of local analysis focuses on particular areas of interest within the structure, providing a comprehensive and nuanced comprehension of localised behaviour.

In the field of structural engineering and finite element analysis (FEA), it is essential to possess a comprehensive understanding of the complexities associated with localised behaviour. Although the global analysis offers a comprehensive perspective on the overall structural response to external pressures and boundary conditions, it often fails to account for the intricacies present in complicated geometries, intricate linkages, or places that are susceptible to stress concentrations. Anomalies may manifest inside these specific localised zones, highlighting the pronounced influence of design alterations or material qualities.

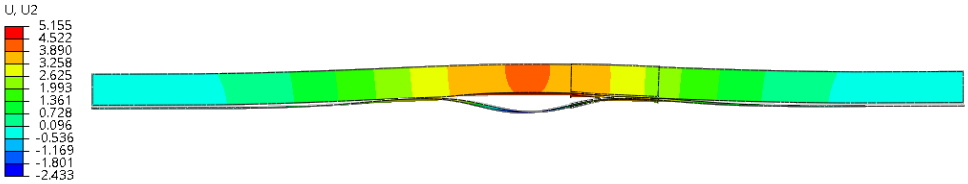
6.2.1 Displacement Field

In a global-local analysis, the coherence between displacement field is probably one of the most important aspects to assure that the solid model is correctly defined. There must be a constant relation between the displacement in the shell and solid models, as the cross section where boundary conditions are applies, should, at all times, be precisely aligned with the shell cross section - Figure 6.4 and Figure 6.5.

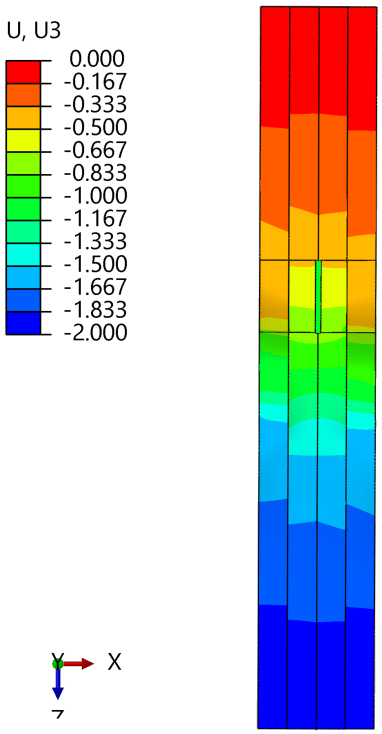


(a) Overall results. (b) Local close-up.

Figure 6.4: Magnitude displacement field.



(a) Displacement field along the y-axis direction.



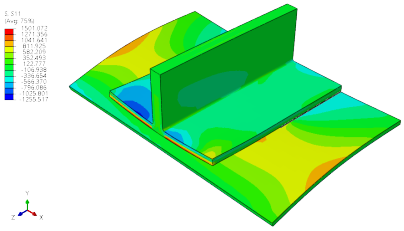
(b) Displacement field along the z-axis direction.

Figure 6.5: Deformation overview the local validation model along directions.

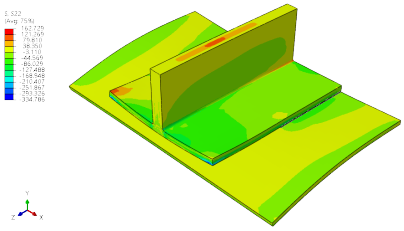
It is concluded that the displacement field is accurately transferred from the global to the local model, as it coherent throughout the models along different axis. All in all, the local model appears well defined and, thus, results highlight a high degree of confidence.

6.2.2 Stress Distribution

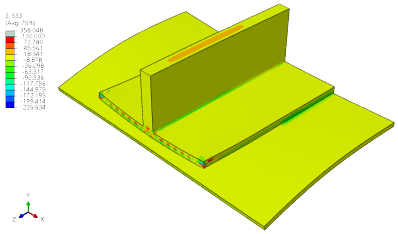
Advancing, it is crucial to observe the stress distribution across the local specimen - Figure 6.6.



(a) S11 stress field.



(b) S22 stress field.



(c) S33 stress field.

Figure 6.6: Stess distribution in the local model.

One of the first takeaways from this methodology is the incompatibility with the material sub-routine selected, which will be later explained in chapter 9 and thus, impedes us to directly compute fibre and matrix failure. Withal, it is important to highlight that, by analysing the stress fields previously displayed, composite failure occurs before the end of the step.

Furthermore, by analysing carefully the stress distribution, it is easily perceptible that the plies subjected to the highest stress are the 0∘ plies on the stringer attached to the cohesive material, as shown in Figure 6.7. Following experimental findings [98], it is possible to assume that the aforestated region is where the stringer component and, ultimately, the skin-stringer system fails.

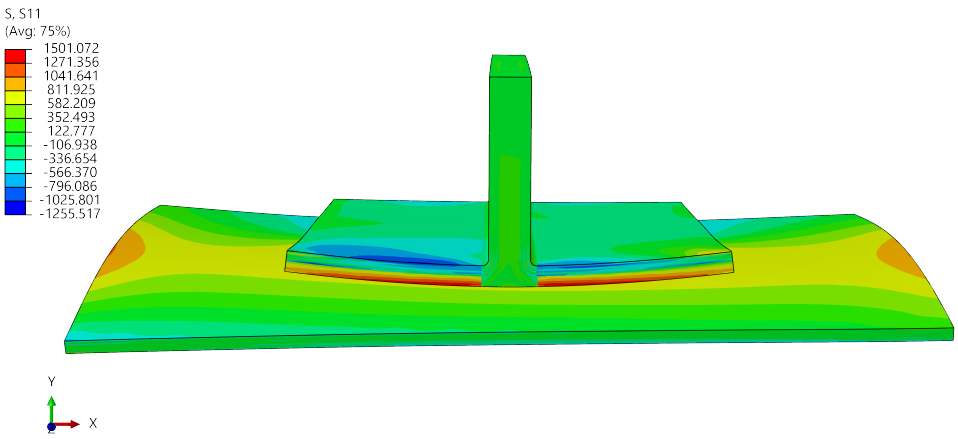


Figure 6.7: S11 distribution focus on the interface region.

6.2.3 Reaction Forces

In order to better understand the reliability of the local finite element mode, it is imperative to analyse the load-displacement curve of the system, whilst comparing it to experimental and numerical results extracted from literature [89], [98].

Hence, the load-displacement curve computed from the local analysis is shown in Figure 6.8.

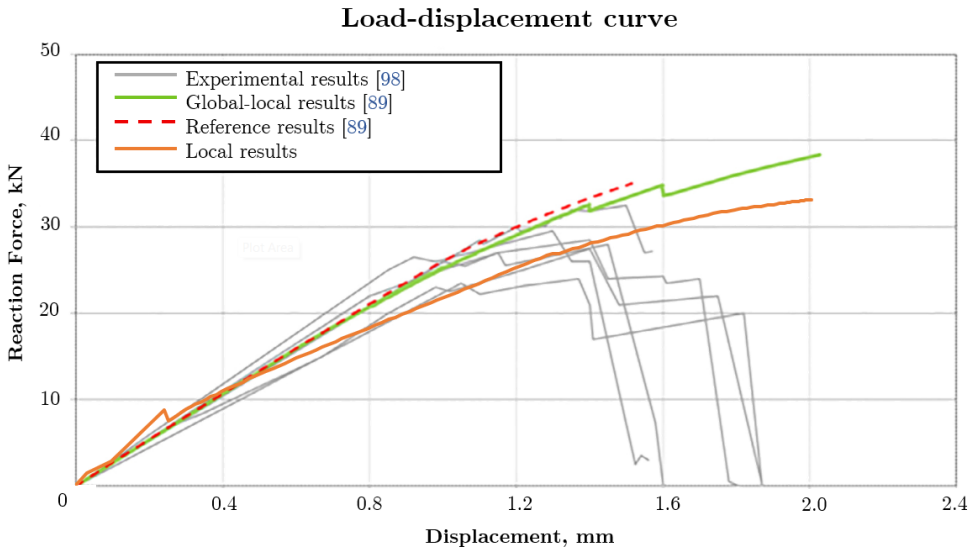


Figure 6.8: Load-displacement curves of the local analysis for debonded panel D1 with comparison to experimental and numerical results extracted from literature [89].

Firstly, it is imperative to understand the drop in stiffness around the displacement of 0.3mm, which is due to the start of damage initiation (the point where the Abaqus variable DMCRIT, which measures the damage initiation criteria of the cohesive elements, reaches the unity value) in the cohesive layer. After the drop, we must compare the results to both the numerical data from Akterskaia et al. [89] and experimental procedures executed by Orifici et al. [98].

When comparing to the numerical results from Akterskaia et al. [89], we see a decrease of 13% in load prior to failure of the component- around 1.2mm. Nonetheless, this number is not at all worrying as, by simple observation of Figure 6.8, we can understand that our results match the experimental findings, as our load-displacement curve is situated in the midst of the several experimental tests conducted.

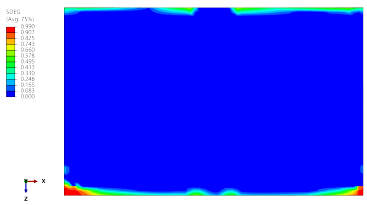
Overall, it is safe to state that this local model, despite being an one-way global-local model, contrary to the two-way local model developed in [89], is more coherent to experimental findings and, accurately exhibits the component of the system. Nonetheless, it is crucial to highlight the fact that no significant drops are noticeable in the model as composite failure was applicable. In addition, the material

sub-routine proved to be one of the limitations of this methodology, which will be explained in chapter 9, which inhibited the computation of the ultimate failure of the component, as portrayed by the final drop in the experimental results.

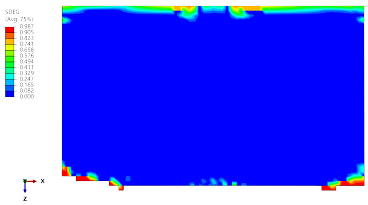
To conclude, the total CPU time required for this model was 973 345 seconds. Considering the accuracy of the model, it should be noted that this time is aa favourable value and should be considered as an advantage of the technique studied. Moreover, this model was allowed to run until the end of the step, which proved to be unnecessary as failure is expected to occur before the maximum displacement of 2.0mm and the analysis could be terminated whenever desired, after the Scalar Stiffness Degradation variable (SDEG) reaches 1.

6.2.4 Delamination Analysis

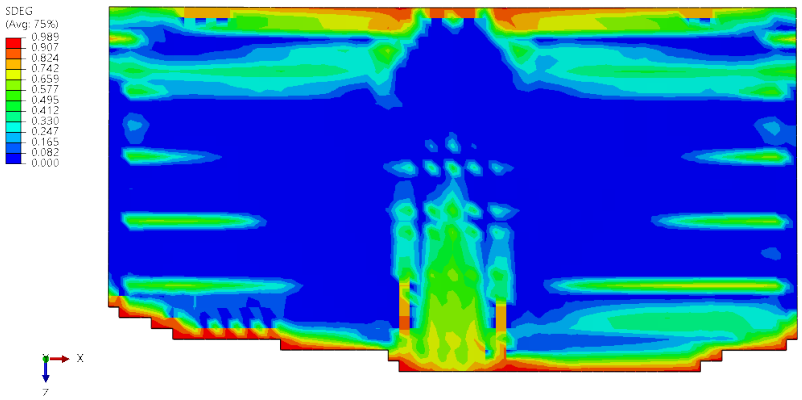
To conclude this analysis, the main focus of this model was to precisely predict delamination in the skin-stringer interface. Thus, it is vital to analyse the cohesive layer independently to better understand the behaviour of the model - Figure 6.9.



(a) Displacement applied of 0.8mm.



(b) Displacement applied of 1.05mm.



(c) Final displacement applied of 2.0mm.

Figure 6.9: Delamination evolution at distinct displacements.

By analysing the presented figures, various takeaways should be noted. Firstly, it is important to consider that delamination initiation (SDEG=1.0) falls approximately around 0.8mm but it reaches significant values around 1.05mm - Figure 6.9b. By analysing the load-displacement curves of the experimental tests, it can be noted

that a drop occurs around the same displacement, which is attributed to delamination growth in the interlaminar interface. Ergo, the model follows the behaviour and, therefore,can be considered satisfactory even though initiation starts earlier in the model, albeit in a very localized and small area.

A crucial point to underscore is the precise initiation of delamination, occurring exactly as indicated by the global model in the highlighted left corner of Figure 6.2b. Given that this region served as a notable stress concentration within the global model, it was imperative to ensure that the same behaviour was replicated in the local analysis. This vital consistency is effectively demonstrated by Figure 6.9a, where the progression of delamination is clearly depicted as originating from the aforementioned stress concentration zone and subsequently advancing towards the center of the cohesive layer.

Furthermore, another key takeaway of this model is that there is a stress concentration around the first free edge of the local model, due to the sub-model boundary conditions being applied in that region. Clearly, this poses as unrealistic and exhibits one of the first disadvantages of the model - localised effects in specific regions of the mesh due to concentrations. Nevertheless, this could be easily fixed by the creation of a buffer zone in the beginning of the cohesive layer. To enhance the credibility of the overall results, it is advisable to introduce a material property analogous to cohesion within a specific section of the component. This material property should precisely mirror the characteristics of cohesion, with the notable omission of any damage initiation criteria. It's worth emphasising that this addition should not disrupt or influence the behaviour of the already delaminated region; rather, it serves the purpose of bolstering the overall integrity and trustworthiness of the findings.

Thus, in order to prove the previous statements, a local model composed of two distinct skin-stringer sets was developed with a buffer zone at the edge of the cohesive layer. The main purpose of this model was to see how the delamination would propagate in both sides of the debonded area. This model was stopped after a time step of 27.60 seconds, due to computational expenses (CPU time was already at 178 200 seconds) and motivated because delamination was propagating at a marvellous rate.

Prior to this analysis, it is key to verify the correct transfer between global and local models, which is depicted in Figure 6.10.

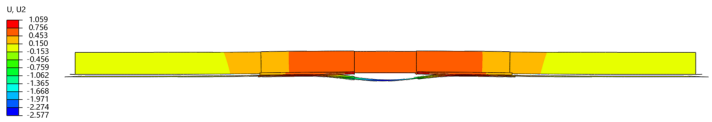


Figure 6.10: Displacement relation between the global and local models along the y-axis direction.

As the model is well defined, it is now important to verse into the delamination propagation in this structure. Hence, considering the damage initiation criteria, i.e., QUADSCRT, when this values reaches the unity value, damage starts and propagates from that element. This evolution can be visualised in Figure 6.11.



(a) Initiation



(b) $t = 27.6$

Figure 6.11: Quadratic stress criteria evolution.

The most important conclusion of this model was that delamination starts where it was anticipated, i.e., the corners shown in Figure 6.2b. This increases the degree of confidence of this model and, thus, the technique.

To conclude, Figure 6.12 shows the delaminated area at the end of this analysis, which can be determined as successful and thus, the methodology can be implemented in a more realistic aeronautic structure.



Figure 6.12: Final delamination plot at $t = 27.60s$.

Part IV

Wing-box analysis

Chapter 7

Finite Element Model

7.1 Wing-box geometry

The wing-box in study complies with the planform depicted in Figure 7.1.

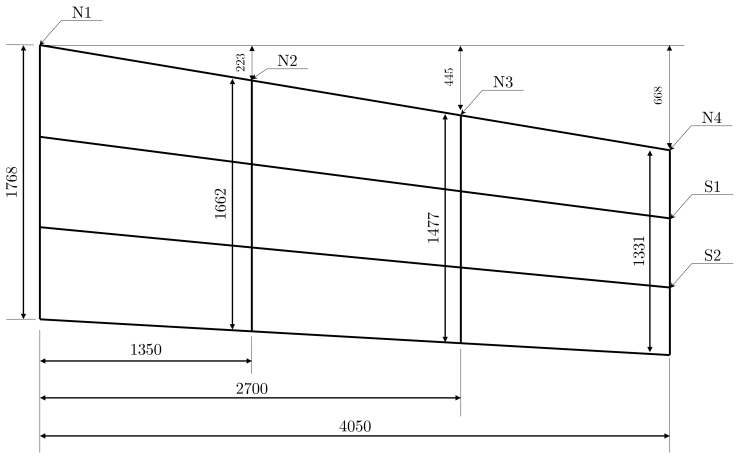
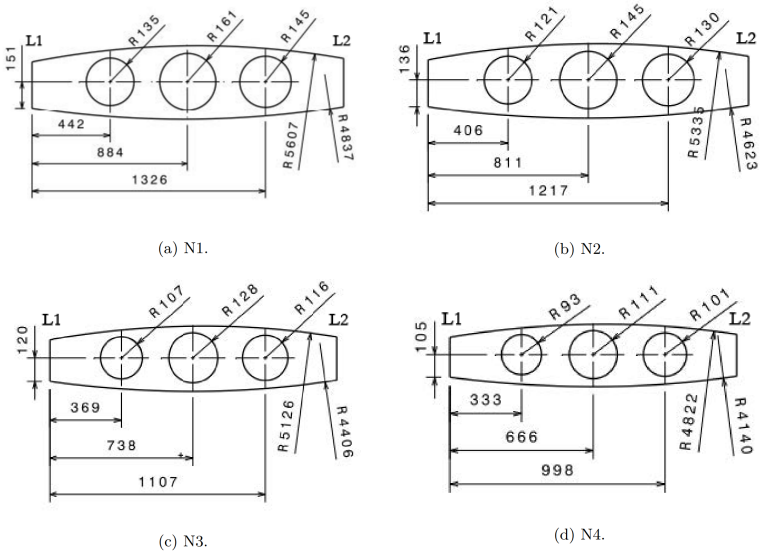


Figure 7.1: Wing planform of the wing-box in study.

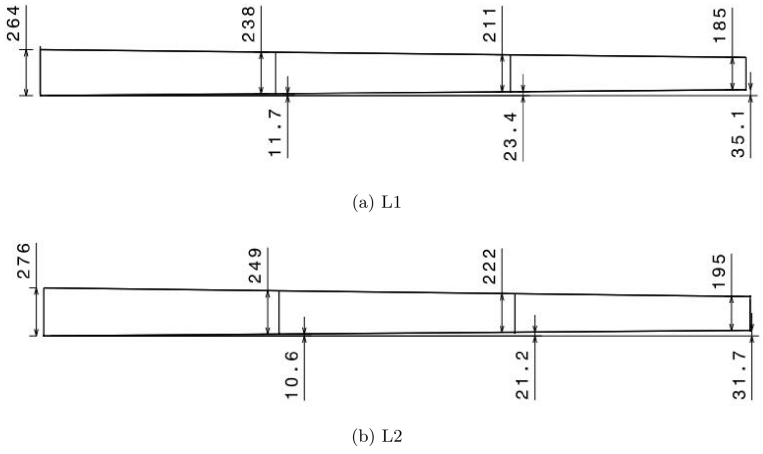
In addition, in Figure 7.1, the ribs (N1 through N4), main front spar (L1), secondary rear spar (L2), stringers (S1 and S2) and panels are included. Concerning the geometric parameters of the structural sub-components, we refer to Figure 7.2, Figure 7.3 and Figure 7.4 for the ribs, spars and flanges' features respectively - concerning the latter, the stringers and both spars are displayed.



(a) N1. (b) N2.

(c) N3. (d) N4.

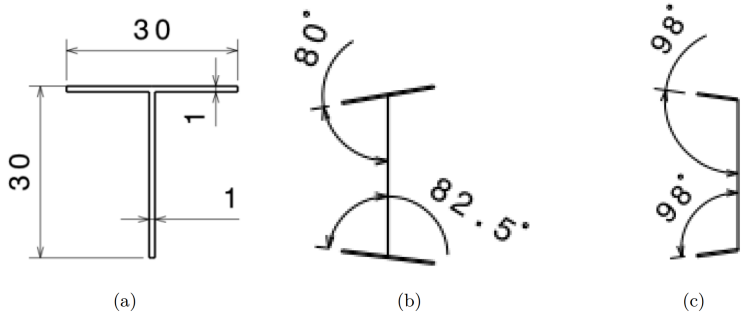
Figure 7.2: Cross-section geometry of the ribs.



(a) L1

(b) L2

Figure 7.3: Spar geometry.



(a) (b) (c)

Figure 7.4: Geometry of the flanges: (a) Stringer, (b) Main front spar (L1), (c) Secondary rear spar (L2).

As mentioned previously, as the aeronautical industry progresses to composite materials, more specifically, to Carbon Fibre-Reinforced Polymers, the skins of both the upper and lower panels were modelled following the material properties presented in chapter 5, i.e., IM7/8552 -Table 5.2. Furthermore, the layup used in the composite section of the skins was a $[0°/+45°/-45°/90°/0°/+45°/-45°/90°]_s$ with ply thickness of 0.1 mm. Moreover, the stringer design followed the strategy analysed in chapter 5, i.e., a the same layup as the skins no alteration to the thickness of the latter.

Nonetheless, since aluminium alloys are still common in the aeronautical industry, for this analysis, an Al2024-T3 alloy was selected for the skin and the ribs (for the web and the flanges), whilst the spars are composed of Al7475-T6. Furthermore, in Table 7.1, the thickness, t, of each structural element is depicted.

Table 7.1: Thickness, t, of the main structural elements.

	$\boldsymbol{t}$ **[mm]**
Rib web	1.5
Main spar (L1) web	2.5
Secondary spar (L2) web	2

Further geometrical considerations are noteworthy nonetheless. Firstly, it should be noted that the position of the rib N1 is not coincident with the wing's root, locating itself 450 mm from the former. Concerning the stringers, these are situated at 13% and 75% of the aerodynamic chord (L1 and L2 respectively) and, thus, do not represent the leading and trailing edge of the wing. On the other hand, the stringers are equally distributed along the wing-box chord (33% for the S1 stringer, whereas this value increases to 66% for S2). Focusing on Figure 7.4, we identify that the T-cross-section of the stringers is constant as well, whilst the main front spar L1 is consistent with an inclined I-profile (where the flanges are considered to boast a constant dimension of 70 mm x 1.5 mm) seeing as both flanges are oblique in relation to the web (angle of 80°for the top flange and 82.5°for the bottom one). Similarly, the flanges of the secondary rear spar L2 (constant 30 mm x 1.5 mm) also position themselves at an angle with respect to the web. However, this angle is equal for both the top and bottom flanges (98°) and the cross-section resembles a C-profile. Likewise, the ribs also assume a C-cross-section (flange dimension of 30 mm x 1 mm). Finally, it should be noted that each structural sub-component is manufactured with a unique vending radius of 2 mm.

7.2 Boundary Conditions

Concerning the boundary conditions, we resort to beam theory in order to define them, seeing as our wing-box constitutes a slender body. Firstly, considering the entire wing, we identify that the root is clamped, whilst the tip is free. We also know from the problem definition that our wing is subjected to a distributed load. In turn, the wing-box in study only comprises a portion of the wing. Thus, we can consider it to be subjected to flexo-torsional loads in both the left and right-hand side cuts that constitute the actual boundary conditions for our wing-box. This is concatenated in Figure 7.5.

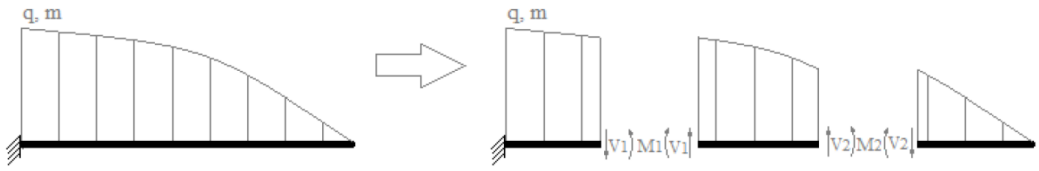


Figure 7.5: Approximation of the wing as a beam.

However, we are not able to replicate the natural boundary conditions in the finite element software. Hence, we resort to geometric ones, i.e, by enforcing the known displacements and rotations (continuity conditions) on one of the extremities (in our case, the one near the wing's root), and the resulting loads from the remaining unmodelled part of the structure (the wing tip) on the other, as per Figure 7.6.

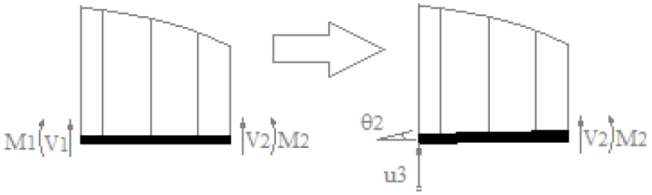


Figure 7.6: Equivalent boundary conditions for the wing-box.

The use of these parameters ensures the continuity condition of the structure. Furthermore, for the problem at hand, we assume that the point close to the root is fixed as the displacements and rotations are small and, thus, may be neglected. Still, caution must be exerted. Saint-Venant's principle, used to describe the behavior of loads and stresses, states:
"If the forces acting on a small portion of the surface of an elastic body are replaced by another statically equivalent system of forces acting on the same portion of the surface, this redistribution of loading produces substantial changes in the stresses locally but has a negligible effect on the stresses at distances which are large in comparison with the linear dimensions of the surface on which the forces are changed."[134]

Consequently, considering the rib N1 to be entirely clamped would result in an unrealistic stress concentration on that area and an artificial over-stiffness of the whole structure. To avoid this, a concession is made by only clamping the spars' web and simply supporting the stringers on the same section. This allows us to maintain the integrity of the structural representation, whilst also complying with the NACA 3781 [135] hypothesis that considers the frame, in the case of the ribs, as simply supported.

7.3 Loading Conditions

Defining the loading condition is obviously a crucial step of our analysis. For analysis purpose, one scenario is enough to test the validity of the global-local technique. Nonetheless, for scientific purposes, it was determined the variety of load conditions that the wing-box can be subjected to according to regulations. Thus, the wing-box studied will be subjected to two main types of loads, i.e., aerodynamic and inertial ones. As mentioned, these are given as combined load distributions for positive and negative gust. Thereby, it is reasonable to assume that they are applied in an imaginary line along the wingspan that lies between the aerodynamic centre and the centre of mass of each cross-section of the aerofoil. However, we are given the load distribution for the shear forces acting on both the main front, v_{z_1}, and secondary rear spars, v_{z_2}, and hence loads are applied within these sub-components. Furthermore, they are enforced as concentrated forces acting at the middle line of the spars - mitigates stress concentrations to the panels whilst preserving structural accuracy of the stress states in each sub-component - and at the intersection between the spars and the ribs - application of the forces at these points ensures that no over-deformation occurs in regions away from the spars due to the concentrated forces - as per Figure 7.7.

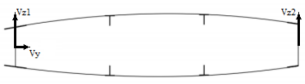
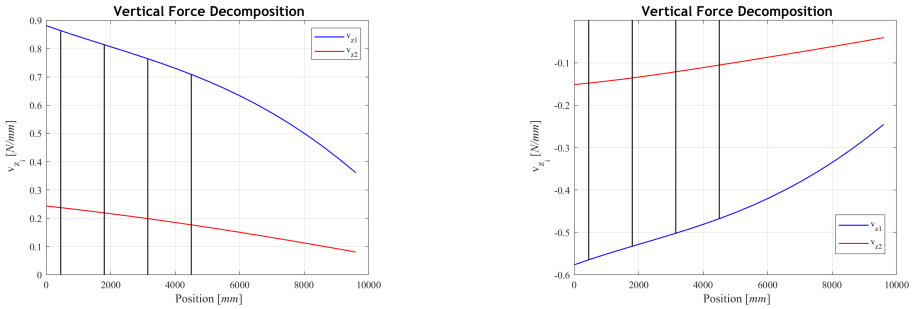


Figure 7.7: Concentrated forces in the rib section.

However, we still need to calculate the shear forces to be applied at each rib - as concentrated forces. To this effect, beginning with the vertical shear distribution, we must initially define the position along the wing span of each rib, resulting in Figure 7.8.

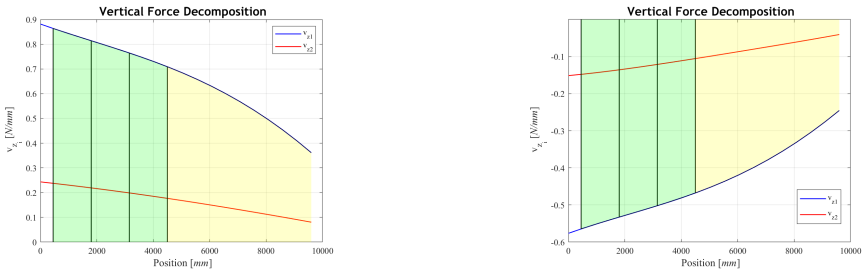


(a) Load case 1. (b) Load case 2.

Figure 7.8: Position of the distributed shear force components for each rib.

Furthermore, the wing-box occupies the region along the wing-span between 450 mm and 4500 mm. The section between the wing's root and the first rib can, nonetheless, be neglected as the corresponding load is replicated by the continuity conditions. This ultimately leads to the delineation of the two distinct regions displayed in Figure 7.9:

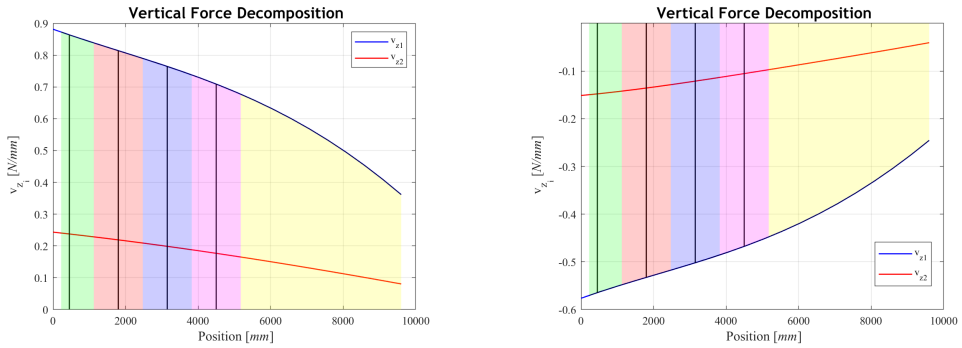
- A green region corresponding to the load acting on the wing-box.
- A yellow region corresponding to the load acting on the wing tip - not represented in the model; that will be applied on the N4 rib.



(a) Load case 1. (b) Load case 2.

Figure 7.9: Load regions along the wing span.

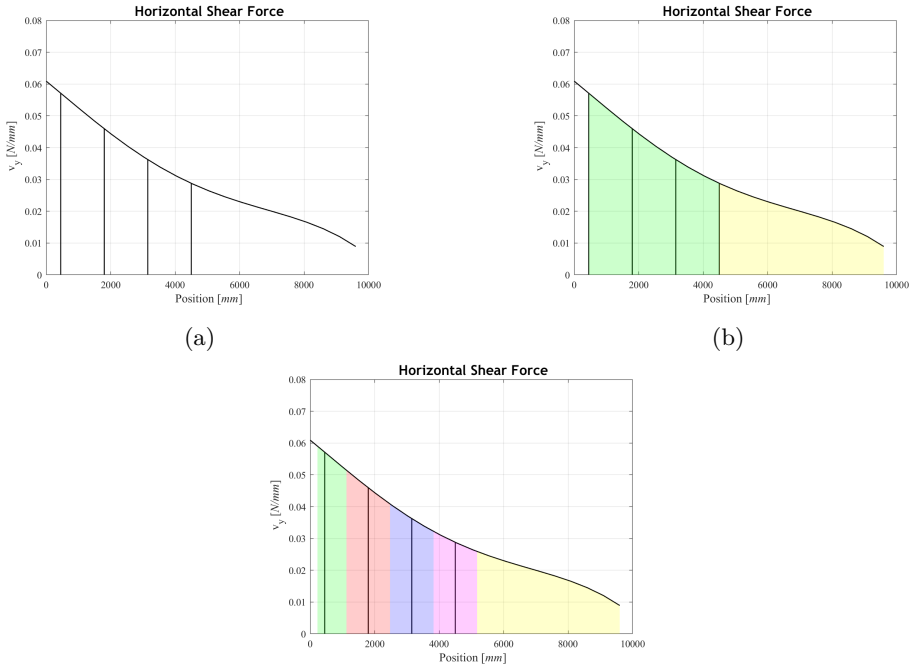
The load acting on each rib can then be evaluated by integrating the curve over the sections corresponding to each rib and to the tip. Concerning the former, the wing-box region is split between 225 mm and 1125 mm for N1, 1125 mm and 2475 mm for N2, 2475 mm and 3825 mm for N3 and between 3825 mm and 5175 mm for N4 respectively - Figure 7.10 -, with each rib sustaining the load of their respective region.



(a) Load case 1. (b) Load case 2.

Figure 7.10: Wing regions along the wing span for load estimation.

In this way, it is then possible to estimate the vertical shear force for each rib via integration and, adopting the same methodology for the horizontal shear force - Figures 7.11 and 7.12 for, respectively, load cases 1 and 2 -, the concentrated loads are promptly determined and compiled in Tables 7.2 and 7.3 for, respectively, load cases 1 and 2.



(a) (b)

(c)

Figure 7.11: Methodology for determining the horizontal shear force applied in each rib for load case 1.

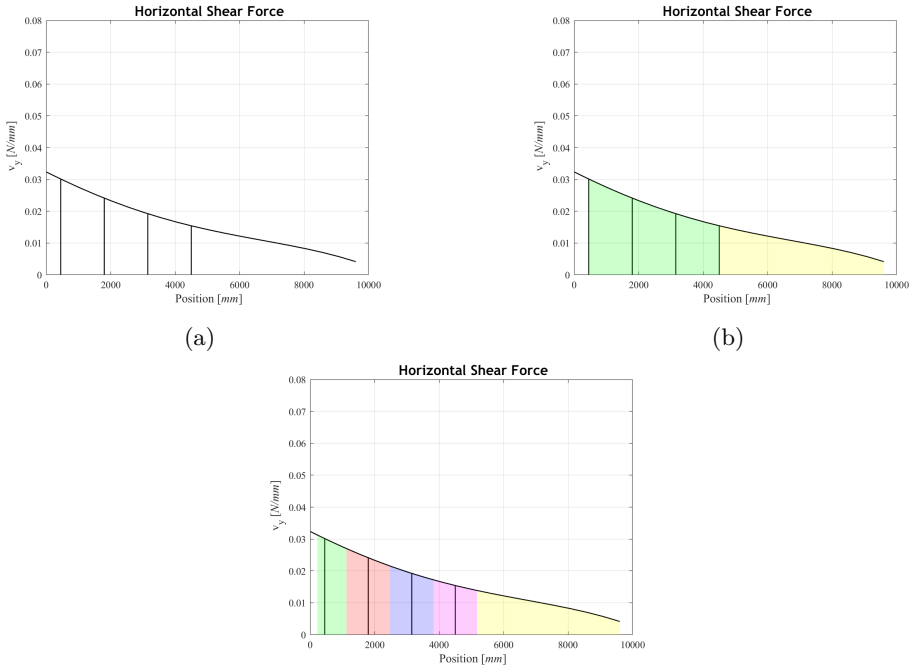


Figure 7.12: Methodology for determining the horizontal shear force applied in each rib for load case 2.

Table 7.2: Shear forces acting on the modelled part of the wing-box for the load case 1.

	N1	**N2**	**N3**	**N4**	**Tip**
$\boldsymbol{V_z}$ **[N]**	981.0	1394.7	1299.9	1194.9	2924.8
$\boldsymbol{V_{z_1}}$ **[N]**	769.8	1099.0	1031.7	956.3	2376.0
$\boldsymbol{V_{z_2}}$ **[N]**	211.2	295.7	268.3	238.6	548.7
$\boldsymbol{V_y}$ **[N]**	49.7	62.1	49.1	39.0	81.3

Table 7.3: Shear forces acting on the modelled part of the wing-box for the load case 2.

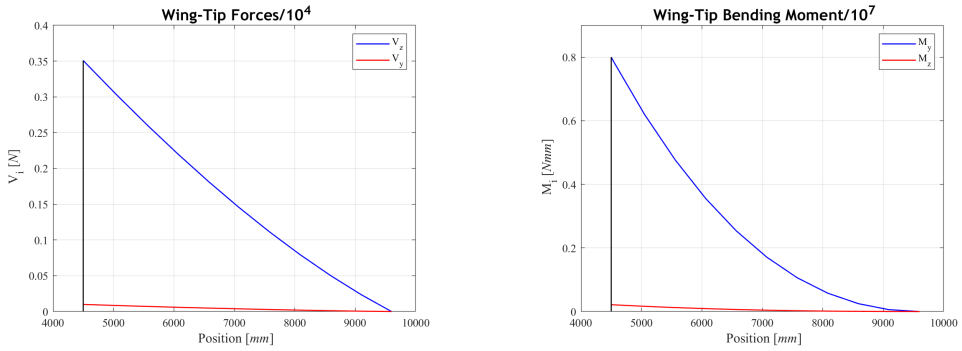
	N1	**N2**	**N3**	**N4**	**Tip**
$\boldsymbol{V_z}$ **[N]**	−634.5	−902.1	−840.8	−772.9	−1891.8
$\boldsymbol{V_{z_1}}$ **[N]**	−503.1	−719.1	−677.3	−630.7	−1584.7
$\boldsymbol{V_{z_2}}$ **[N]**	−131.4	−183.0	−163.5	−142.2	−307.1
$\boldsymbol{V_y}$ **[N]**	26.2	32.6	26.0	20.9	41.5

Still, the flexo-torsional loads resulting from the wing-tip must be determined via:

$$V_i = V_{i-1} + \frac{v_i + v_{i-1}}{2}(Y_{i-1} - Y_i) \tag{7.1}$$

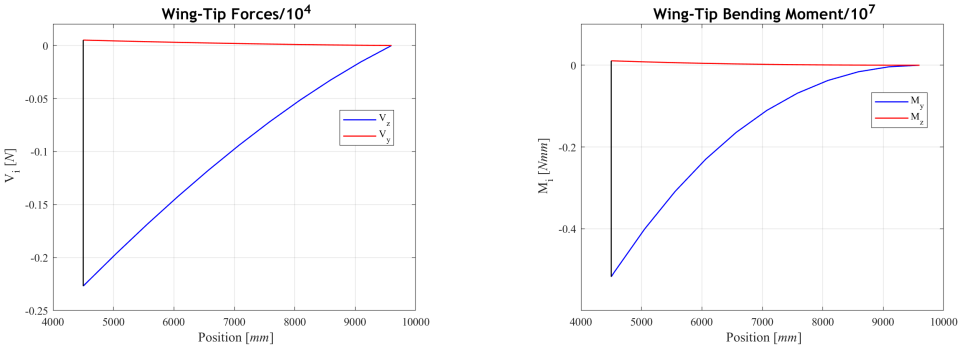
$$M_i = M_{i-1} + \frac{V_i + V_{i-1}}{2}(Y_{i-1} - Y_i) \tag{7.2}$$

where V is the resulting shear force, v the distributed shear force - per unit length -, M the resulting bending moment and Y is the distance of the application point of the force with respect to the considered pole - in this case, the last modelled rib. The resulting diagrams are shown in Figures 7.13 and 7.14 for, respectively, load cases 1 and 2, where it is worth noting that the vertical load, V_z, is the one producing the bending moment M_y, whilst V_y introduces the bending moment M_z. The moments to be taken into account are given in Tables 7.4 and 7.5 for, respectively, load cases 1 and 2.



(a) Vertical shear force. (b) Bending moment.

Figure 7.13: Resulting loads on the wing tip for load case 1.



(a) Vertical shear force. (b) Bending moment.

Figure 7.14: Resulting loads on the wing tip for load case 2.

Table 7.4: Resulting bending and torsional moments acting on the wing tip for load case 1.

M_y [Nmm]	7.9991e6
M_z [Nmm]	2.1567e5

Table 7.5: Resulting bending and torsional moments acting on the wing tip for load case 2.

M_y [Nmm]	−5.1741e6
M_z [Nmm]	1.0814e5

Within the finite element software, to introduce the loads acting on the tip, it is also necessary to define a *structural distributed coupling* with linear weighting as per Figure 7.15, a constraint that enables us to transfer mechanical information from one point - where the load is applied - to another set of points. However, since the forces reported above are the combined loads - inertial + aerodynamic -, the position of the reference point - application point - to be used must be assumed. Still, it is reasonable to assume that such point lies between the aerodynamic centre and the baricentre of the aerofoil for rib N4. Within the context of this report, the aerodynamic centre was selected as the reference point - refer to Figure 7.16.

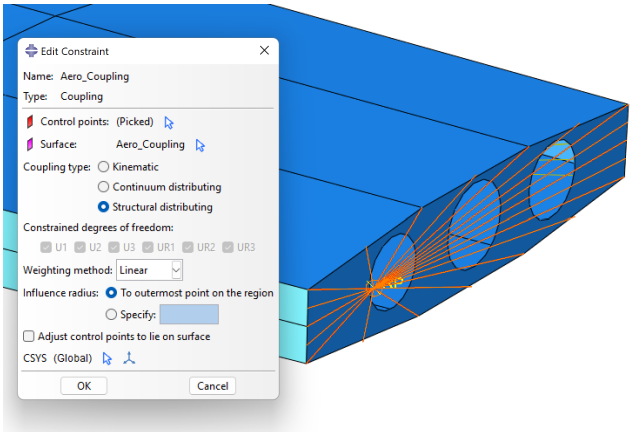


Figure 7.15: Coupling constraint for the wing tip loads.

7.4 Limit and ultimate loading

Finally, it should be noted that the analysis must be conducted in both limit and ultimate loading conditions. For the latter, it should be noted that every load must be multiplied by a safety factor of 1.5. The fully loaded and constrained model is depicted in Figure 7.16 for, respectively, loading cases 1 and 2, and the applied load and moment values are compiled in Table 7.6 to Table 7.13 for each loading case and condition.

Table 7.6: Forces for limit condition: load case 1.

	CF1 [N]	**CF2 [N]**	**CF3 [N]**
N1/L1	49.7	1769.8	0
N1/L2	0	211.2	0
N2/L1	62.1	1099.0	0
N2/L2	0	295.75	0
N3/L1	49.1	1031.7	0
N3/L2	0	268.3	0
N4/L1	39.0	956.3	0
N4/L2	0	238.6	0
Tip	81.3	2924.8	0

Table 7.7: Forces for ultimate condition: load case 1 [N].

	CF1 [N]	**CF2 [N]**	**CF3 [N]**
N1/L1	74.5	1154.7	0
N1/L2	0	316.8	0
N2/L1	93.2	1648.5	0
N2/L2	0	443.5	0
N3/L1	73.6	1547.5	0
N3/L2	0	402.4	0
N4/L1	58.5	1434.4	0
N4/L2	0	357.9	0
Tip	121.9	4387.1	0

Table 7.8: Forces for limit condition: load case 2.

	CF1 [N]	**CF2 [N]**	**CF3 [N]**
N1/L1	26.2	−503.1	0
N1/L2	0	−131.4	0
N2/L1	32.6	−719.1	0
N2/L2	0	−183.0	0
N3/L1	26.0	−677.3	0
N3/L2	0	−163.5	0
N4/L1	20.9	−630.7	0
N4/L2	0	−142.2	0
Tip	41.5	−1891.8	0

Table 7.9: Forces for ultimate condition: load case 2.

	CF1 [N]	**CF2 [N]**	**CF3 [N]**
N1/L1	39.3	−754.7	0
N1/L2	0	−197.1	0
N2/L1	49.0	−1078.6	0
N2/L2	0	−274.5	0
N3/L1	39.0	−1016.0	0
N3/L2	0	−245.2	0
N4/L1	31.3	−946.0	0
N4/L2	0	−213.3	0
Tip	62.2	−2837.7	0

Table 7.10: Moments for limit condition: load case 1.

	CM1 [Nmm]	**CM2 [Nmm]**
Tip	−7.9991e06	2.1567e05

Table 7.11: Moments for ultimate condition: load case 1.

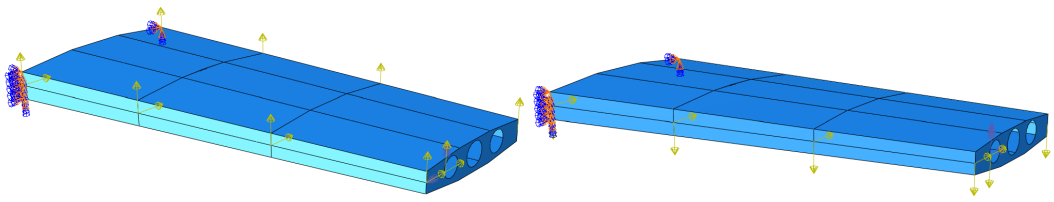
	CM1 [Nmm]	**CM2 [Nmm]**
Tip	−1.1999e07	3.2351e05

Table 7.12: Moments for limit condition: load case 2.

	CM1 [Nmm]	**CM2 [Nmm]**
Tip	5.1741e06	7.7611e06

Table 7.13: Moments for ultimate condition: load case 2.

	CM1 [Nmm]	**CM2 [Nmm]**
Tip	1.0814e05	1.6222e05



(a) (b)

Figure 7.16: Boundary conditions and loads applied in the wing-box: (a) load case 1 (b) load case 2.

7.5 Global Model

A quadrilateral structured mesh was selected for our model[1]. The model was seeded with an average mesh size of 20 mm - Figure 7.17. Concerning the elements employed, the beam sections are discretized via B31 2-node linear beam elements and the skins with fully integrated S4 general-purpose shell elements - Table 7.14 -, instead of the usual reduced-integration S4R ones.

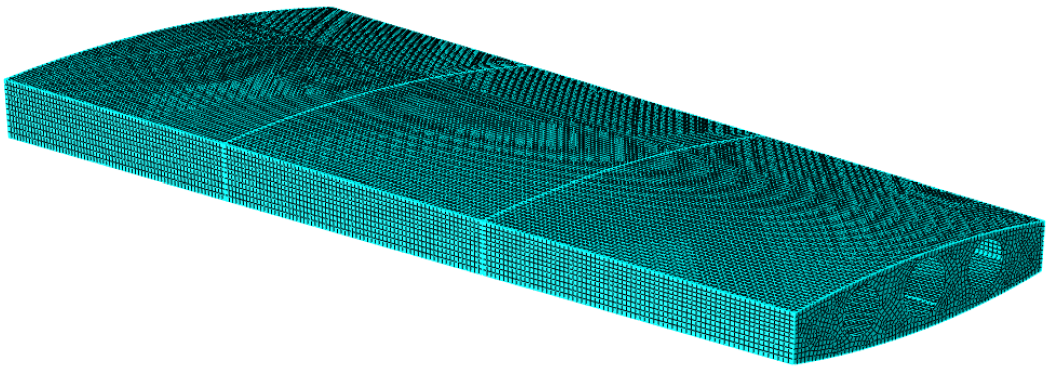


Figure 7.17: Mesh.

Table 7.14: Types of elements per region.

Region	**Element Type**
Beam sections	B31
Skins	S4

Furthermore, let us also focus on the previously mentioned details for the fatigue study. Beginning with the inspection hole, as per Figure 7.18, a structured mesh was enforced and the refinement was achieved via local seeding on the radial partitions - with 25 elements. A bias ratio was also selected in order to more accurately capture the stress distribution in areas within the circular crown extremely close to the radius of the hole.

[1]Except for the ribs, where it is not available. Hence, a free quadrilateral mesh is chosen for this section.

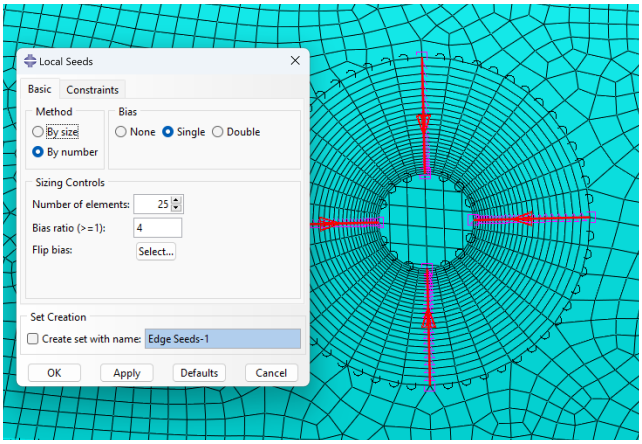
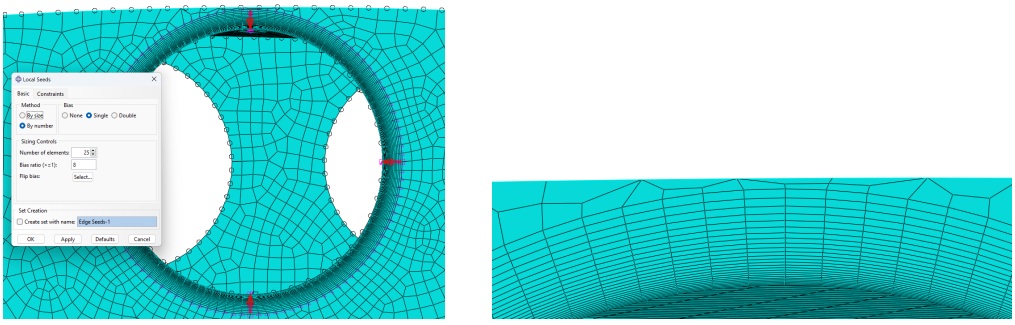


Figure 7.18: Structured mesh in the lower panel around the inspection hole.

Similarly to the inspection hole, a structured mesh was enforced within the partitioned region of the ribs - Figure 7.19. Mesh refinement was performed via local seeding on both the radial - 25 elements - and circumferential directions - 30 elements -, and, for the aforementioned reason, a bias ratio was adopted. Furthermore, when it comes to this component, extreme care should be taken in the region close to the flange illustrated in Figure 7.19b, as an improper mesh definition could lead to distorted elements - due to the proximity of the outer crown to the flange - that would naturally affect our results. Nevertheless, no distortion is visible, strengthening our mesh construction. Finally, it should also be noted that, for both the inspection hole and ribs, such meshes provide an efficient manner for which a radial path may be selected for a swift determination of the stress concentration factors.



(a) Mesh refinement.

(b) Mesh close to the flange.

Figure 7.19: Structured mesh in the partition around the central hole in rib N2.

All material properties followed those selected in subsection 5.2.2, for both the CFRP laminae and the cohesive elements. The exact proven technique was applied, related to both material definition. Nonetheless, the main distinction between these models, was that in the full shell wing-box, the stringers were represented via the

stringer option, contrary to the shell stringers introduced in subsection 5.2.2. This was do to two distinct factors: the shell stringer in the full model would cause severe complications in terms of material penetration and, since the main purpose of this model is to be as simple as possible, the introduction of this component would, ultimately, jeopardize the shell model. Furthermore, this option was also justified by the fact that, after carefully investigating all options possible for the validation model, it was determined that the submodel boundary condition in the flange of the stringer was directly correlated with computational problems and did not impact the solution.

7.6 Local Model

The solid model were examined with a focus on the critical areas indicated during the global analysis, leading to the identification of specific sites in the local models. Local models are used to depict the skin and stringer in areas where debonding is expected to occur.

In this analysis, the skin and stringer components are represented using 8-nodes C3D8 linear solid elements. The cohesive layer was modelled using cohesive components with a non-zero thickness (COH3D8) and a quadratic traction-separation rule. Early mesh convergence experiments have shown that the appropriate in-plane length of the local element for this system panel is 5 mm. Additionally, the out-of-plane length is determined to be 0.1 mm, resulting in one element per lamina in the thickness direction.

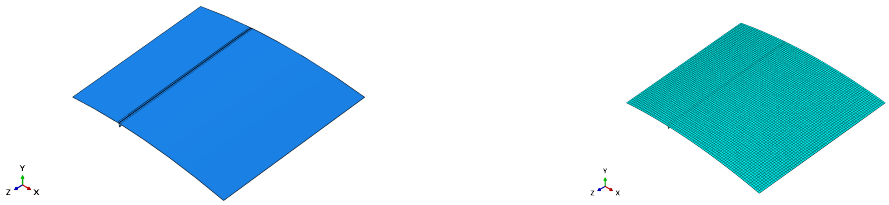
Moreover, during the early stages of the computation of the local models, two primary challenges emerged, namely the density of the filament mesh and the size of the cohesive elements. In the preceding analysis, it was discovered that an element size of 5 mm represents the dimension that can be used without introducing additional complexity and computational overhead. Increasing it to 20 mm yielded fewer elements but it caused the elements to be over the recommended aspect ratio. Given the direct connection between this section and the adhesive layer, it was ascertained that the 5mm value precisely fulfils the requirements.

The submodelling approach in Abaqus was used to define the boundary conditions (BCs), with the global shell model governing the behaviour of the local solid model. Therefore, due to the limitations of the tool in Abaqus, it was not feasible to execute thickness discretization. Specifically, it was not possible to apply different submodel boundary conditions to either the skin or the stringer's web and flange.

Given the direct dependence of this model on the global analysis, it was imperative to use the same analysis type as the global model to ensure minimal computing expenses. Following the methodology validated in the previous Part, a Dynamic, Implicit step was defined albeit now with a total step time of 1 seconds. This is

due to the fact, during turbulence, the wing suffers substantial deflection in a short amount of time. The global model followed this statement and, thus, the local must too.

In conclusion, after the verification of the exact assembly of the Assembly and the proper positioning of the local model at the interface between models, the resultant combined model may be shown in Figure 7.20a. Furthermore, in Figure 7.20b it is possible to observe the final mesh of the local model. Due to computational expenses, an element length of 20mm was defined in the longitudinal direction, whilst maintaining 1 element per ply in the transverse direction. This yielded a total of 131.852 total C3D8 elements, that, considering the desired computational costs, anticipated a slow convergence during the local analysis. The element size defined was, things considered, a extremely difficult task as it caused problems considering the large aspect ratio of the elements. Nevertheless, this highlighted one negative aspect of the global-local technique in large models, which will be discussed later.



(a) Local assembly. (b) Local mesh.

Figure 7.20: First local model.

During analysis, it was determined that the above model was too complex for an effective global-local methodology. Ergo, this model was simplified by removing the all of the sides of the skin, leaving just the interface between the stringer and the cohesive region, as observed in Figure 7.21. Moreover, by decreasing the overall dimensions of the model, it was possible to decrease the element size so that the aspect ratio stopped being an issue. Yet, by decreasing the element length, the overall number of elements increased to 155 506 C3D8 and 4536 COH3D elements, which boosts computational costs.

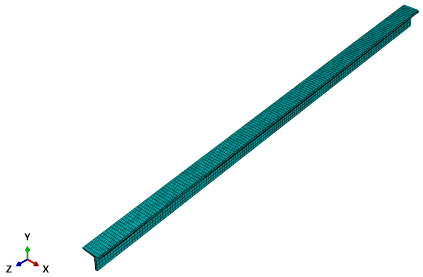


Figure 7.21: Mesh.

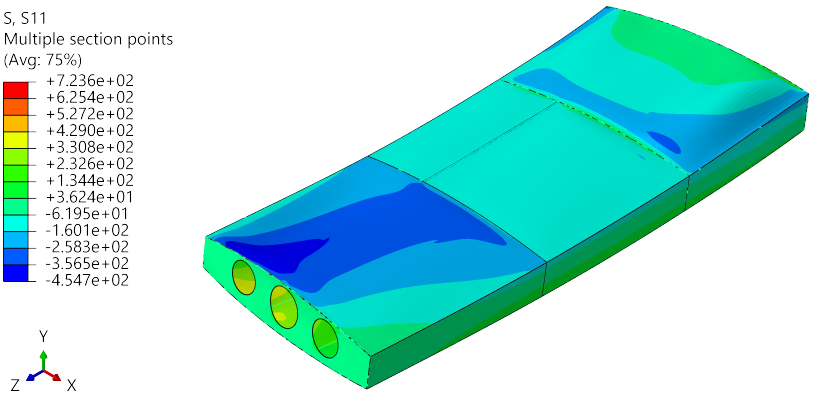
Chapter 8

Wing-Box Results

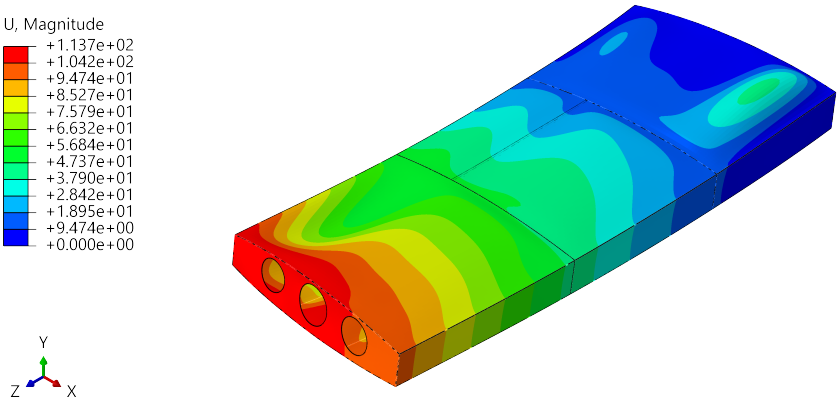
In this chapter, our objective is to provide an exhaustive analysis of the outcomes obtained through the application of the global-local technique to a wing-box model. To achieve this aim, we initiate by presenting the results from the global analysis and the consequent interpretation.

8.1 Global Results

In this section, we aim to post-process the results obtained from the finite element simulation to determine the relevant stress components in the ventral composite panel, as well as the stress concentration and fatigue notch factors in the central panel of the lower skin - where the hole is located - and the N2 rib. Still, let us begin with the displacement field obtained - depicted in Figure 8.1 for the ultimate load for load case (1). From the figures, and focusing specifically on the ultimate loading condition, we identify maximum normal stress in the x-axis direction of 723.6 MPa and maximum displacement values of 1.137e02 mm for load case 1. Remaining displacement field outputs are presented in Appendix A.



(a) S11 stress field.



(b) Displacement field.

Figure 8.1: Results for the global wing-box analysis.

For research purposes, the values extracted from this model do not have any form of validation other than mechanical engineering knowledge. Thus, by analysing the outputs and considering that the total computational time for this model was 98.00 seconds, this global model is extremely satisfactory.

8.2 Local Results

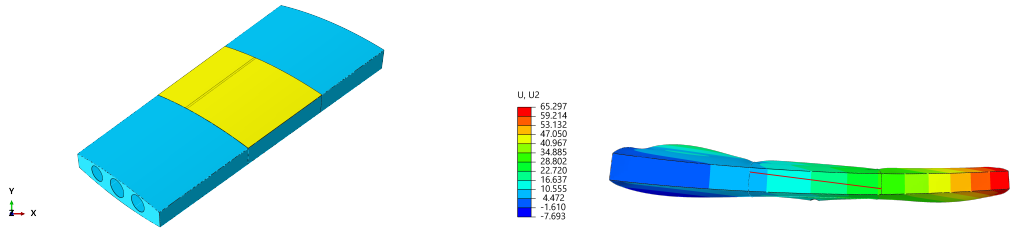
The main purpose of this project was to develop an accurate and efficient one way global-local technique to predict delamination in a skin-stringer interface in a real aeronautical case. Thus, the methodology was validated using a small, flat skin-stringer interface, with the overall dimension of 400mm and a local of 60mm. By expanding the procedure to the wing-box, the overall size of the model increased to 4050mm, whilst the total length of the local increased to 1350mm, meaning that the model size expanded about 1000% and 2250% respectively.

Furthermore, with an element size that disrespected aspect ratio parameters in Abaqus, the number of total elements increased from 37 250 total elements from the

validation model, to 132 678 elements - an increase of 356%. When compared to the model with a smaller element size, this boost in elements rose to 429%. Prior to analysis, this could be an early indicative that the global-local technique would not prove itself as beneficial as initially supported. The overall computational costs would increase substantially due to an enormous model.

In addition, another important aspect to considerer was the curvature of the panel, which was not present in the validation section. Despite being impossible to measure, all models reflected large difficulties when transmitting the displacement field from the global to the local model. This was attributed to the complex geometry since the exact same problem occurred when the local model was simplified to just the skin-stringer region - Figure 7.21.

Nevertheless, important takeaways must be determined from this model. Thus, in Figure 8.2, the displacement evolution of the local model is observed. It is notorious that, at the initial state, as mandatory, the local panel is precisely aligned with the shell surface of the global model.

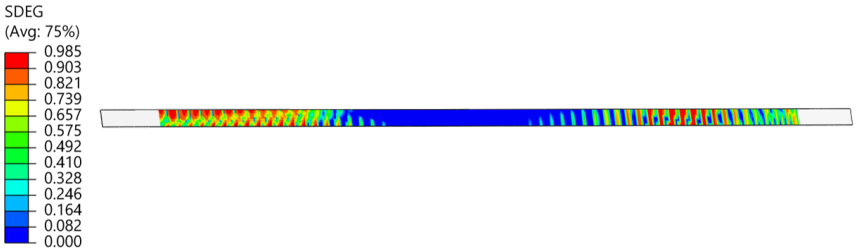


(a) Global and locaal displacement at $t = 0.0s$.

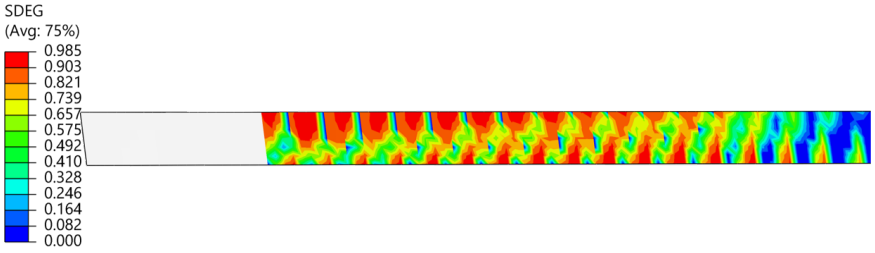
(b) Displacement field at $t = 0.57s$.

Figure 8.2: Displacement evolution in the wing-box global-local model.

Nevertheless, despite the local model not exhibiting the same displacement field as the global, it is possible to understand if the it would eventually delaminate. By assessing Figure 8.3, it is possible to observe that the skin-stringer would, in the real life scenario, delaminate when subjected to those conditions. Albeit not accurate, it is a good indicative that the model needs improvements in terms of materials, either improvement in the adhesive or increase in stiffness to resist better the deflection caused by gust loads.



(a) Global and locaal displacement at $t = 0.0s$.



(b) Close-up.

Figure 8.3: SDEG field in the cohesive layer of the wing-box [1].

Moreover, it is important to mention that this model required a total of 32,476 seconds in CPU time to get close to delamination. This means that, if the accurate displacement field was transferred between models, this time would increase substantially. In addition, this model was established with an element size too big for the requirements of the model, being that in order to improve the accuracy of the analysis, the number of elements would grow, enlarging extensively computational expenses and, thus, lowering the main advantage of this methodology.

To conclude, it is notorious that the one-way global-local technique with the use of material sub-routines still requires a lot of improvements and, albeit the notorious advantages shown during the validation procedure, still possesses some remarks that restrict its use. Throughout the course of this project, many problems arose that required adaptations and improvements. Hence, in order to better understand the limitations of this methodology, chapter 9 demonstrates many variations of the technique that proved to be unsuitable.

Part V

Limitations and Conclusion

Chapter 9

Limitations

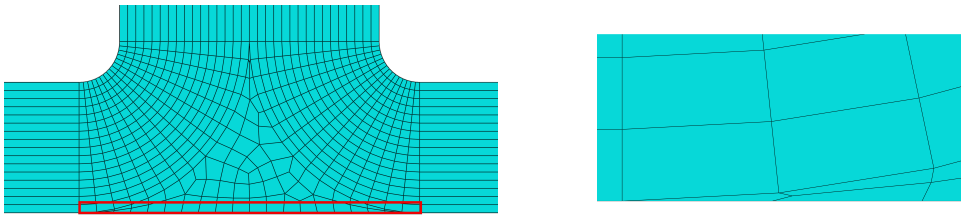
Being that the main focus of this project was to develop a novel one-way global-local technique using Abaqus software, it was clear from the start that the methodology had some restrictions that required adaptations throughout the whole process.

First of all, it is crucial to highlight that the first limitation that arose was the sub-model boundary condition applied in the web region of the stringer. By trial an error, it was clear that this condition did not allow the model to run. During the execution of this project, numerous simulations were conducted and all aborted when the aforementioned condition was present. This does not possess a logical explanation other than the fact Abaqus Implicit Solver was not coherent when transmitting the displacement fields in both the x and y-axis directions at the same time.

This was quickly surpassed by the removal of the boundary condition which, all this considered, did not affect at all the final displacement field of the local model. Nonetheless, the first takeaway extracted from this limitation is that the load-displacement curve does not account for the totality of the reaction forces present in the model.

Advancing, another key aspect was the presence of singularities in both the validation and the wing-box models. By applying the sub-model boundary condition, the ply closer to the cohesive elements showed enormous reaction forces well over the normal for the rest of the model. In the validation stringer, this was attributed to the hexahedron elements in the elastic region in the middle of the component

closest to the fist ply- Figure 9.1. This is due to the fact that these elements have 2 nodes extremely close to each other, as it possible to observe.



(a) Region responsible for the concentrations. (b) Close-up on the responsible elements.

Figure 9.1: Mesh stress concentrations.

Ergo, these elements influenced the model arriving at the results depicted in Figure 9.2. By simple visual analysis, it is clearly visible that these results are negligible and had to be improved.

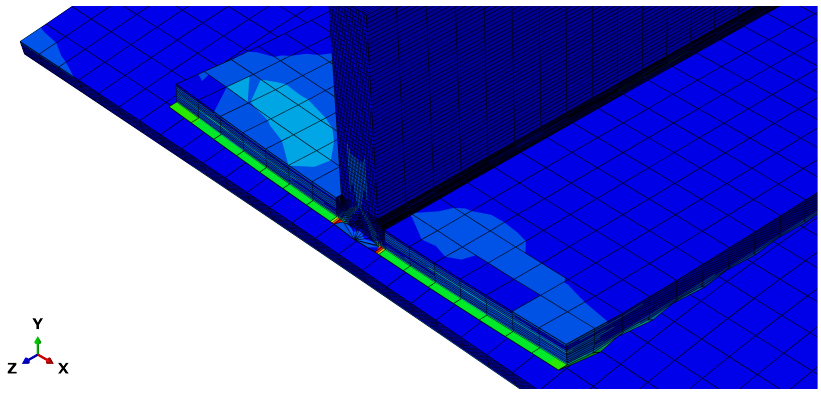


Figure 9.2: Resultant of the stress concentration.

This problem was solved by removing the sub-model boundary condition in the last ply of the flanges and resulted in the accurate values presented in section 6.2 . This is crucial to take into account when performing the one-way local global-local technique herein developed.

Likewise, a singularity can occur in the extremities of the skin being analysed, which is presented in Figure 9.3.

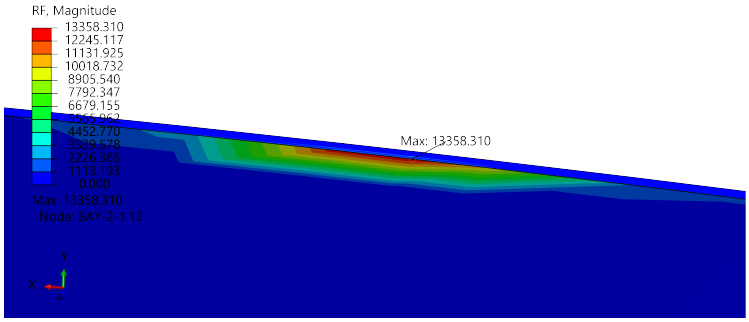


Figure 9.3: Resultant of the stress concentration in the local wing-box skin.

The aforestated problem is, thus, solved by either removing the sub-model BC from the extremity plies, which decreases the reaction forces present in the model or by dividing the boundary conditions and decreasing the Exterior Tolerance in the extremity plies to 0.05. The latter should be the option utilised as it results in a more accurate model.

To conclude, the main limitation of this methodology rose from the wing-box local model. Here, the number of elements heavily increased and thus computational costs. It was clearly noted that the curvature of the panel also proved to be one of the most limiting conditions. Moreover, the size of the model, which resulted in excessive computational times. The aforestated model required over 75,600 seconds in CPU time to arrive at 75% of the time step. This value is incredibly long considering the fact that no delamination was achieved. Comparing to the validated skin-stringer, the CPU time necessary to achieve delamination was just under 1200 seconds. Ergo, this fact defeated the main purpose of the methodology and exhibited the most important limitation of the technique, its extreme sensibility to the number of elements.

Chapter 10

Conclusions and future work

In this thesis, a novel modelling and simulation approach was used to investigate interlaminar failure within the scope of the aeronautical industry. The objective was to assess the efficiency of this technique and determine its main advantages and disadvantages. This chapter is dedicated to the presentation of the primary findings derived from our research. This section presents the key elements to be retained from the current state of the art, the numerical technique used, and the accompanying findings. Finally, considering that the current thesis represents a first endeavour in comprehending the methodologies of modelling and simulating via an one-way global-local technique. it is necessary to investigate potential future research that should be undertaken in light of the results drawn from this study.

10.1 Conclusions

The incorporation of innovative materials plays a crucial role in the development of lightweight and high-performance structures within the dynamic field of aeronautical engineering. Carbon fiber-reinforced polymers (CFRPs) have arisen as a significant innovation within the realm of materials, presenting a notable equilibrium between strength and weight. Carbon fibre reinforced polymers (CFRPs) possess the capacity to bring about a transformative impact on the aviation sector. To effectively incorporate CFRPs into aircraft structures, it is essential to possess a comprehensive comprehension of their mechanical characteristics, failure causes, and reliable

modelling methodologies. This study has examined the Global-Local approach as an effective methodology for analysing Carbon Fibre Reinforced Polymer (CFRP) structures. The investigation begins by reviewing the current knowledge in composite materials and certification protocols, and concludes with the implementation of this strategy in a real-world aircraft context.

As the aeronautical industry undergoes a paradigm change from prioritising maximum performance regardless of cost to adopting more cost-conscious solutions, there is a growing focus over the use of Finite Element Models that depict even the most profound intricacies of all failure mechanisms present in composite materials. Although many techniques and failure criteria have been developed in the past, computational improvements paired with a more cost-conscious industry highlight the necessity of more detailed simulations capable of certifying CFRP components that cost enormous amounts of money to develop. In order to address this issue, considerable research efforts have been dedicated to damage initiation and growth criteria as a tool to improve commercial software, such as Abaqus, to allow the creation of models capable of certifying components.

However, the effective implementation of these innovations heavily relies on the support of structural validation initiatives, which are often initiated when a new composite material is developed. Typically, these experiments follow a building-block methodology, where a series of modest and cost-effective samples are subjected to basic loading conditions. The purpose of this technique is to establish design allowables before examining the material's behaviour in more intricate structural configurations. The process of testing in isolation is, however, characterised by significant expenses and time requirements. As a result, it is crucial to prioritise the development of precise analytical and numerical models that may assist or possibly replace this technique.

In order to achieve this objective, it is crucial to possess a comprehensive understanding of the damage processes that need to be identified. In the case of composite materials, these mechanisms are intrinsically more complex compared to their conventional metallic equivalents. Laminated materials often exhibit several localised failures at smaller length scales before experiencing rupture. These failures progressively develop and aggregate throughout the loading process, eventually leading to catastrophic failure. Given the complex nature of damage initiation and progression in composite materials, it is crucial to establish a suitable definition of the modelling scale, since this has significant importance in the field of composite materials. Although lower scales provide a more detailed explanation of individual instances of damage, the associated micromechanical models are too intricate given the existing

computer capabilities. Consequently, mechanical models that rely on a ply-by-ply discretization approach are considered more appropriate for assessing the damage and failure of the overall laminate. In this approach, the laminate layers are treated as the fundamental homogeneous components, while disregarding imperfections and variabilities present at smaller scales. In the context of meso-mechanics, the modelling of interlaminar damage often involves the use of cohesive zone models. These models rely on precise kinematic representations of the fracture process and are guided by a traction-separation law that determines the initiation of delamination and full decohesion. In contrast, intralaminar damage is commonly modelled using a continuum damage mechanics approach, which seeks to forecast the material's behaviour. Specifically, this approach examines how the material responds when damage is initiated under certain stress conditions and subsequently propagates as the applied loads further increase the stresses within the material.

The Global-Local approach has evolved as a robust tool for the analysis of CFRP structures, with the potential to effectively integrate global behaviour and local subtleties. By using this methodology, we effectively integrated the comprehensive perspectives derived from global analysis with the meticulous investigations facilitated by local analysis. The present study demonstrated the effectiveness of cohesive zone models in Abaqus as important tools for accurately representing the intricate aspects of CFRP failure behaviour. The creation and validation of a skin-stringer model played a crucial role in showcasing the effectiveness of the Global-Local approach in simulating intricate delamination events.

The numerical model herein adopted consisted of a composite damage model implemented within a finite element framework capable of predicting intra- and interlaminar damage mechanisms. The intralaminar failure was depicted with the usage of a material sub-routine that proved to be a severe limitation in the modelling of 3-dimensional solid models, whilst the modelling of interlaminar failure was achieved with the implementation of Abaqus/Implicit cohesive surfaces with damage onset and propagation being respectively governed by a quadratic traction criterion and the Benzeggagh-Kenane criteria. Moreover, to accurately represent the behaviour of the material, ply-by-ply discretization was executed throughout every local model portrayed, whilst more conservative shell models were developed for the global step of the analysis.

The numerical results pertaining to the validation of the technique,i.e., the 400mm skin-stringer system show a remarkable correlation with the experimental ones. For the aforestated model, many iteration were done in the hopes of achieving the mos accurate displacement transition between the global and local tests. The

influence of different boundary conditions and the respective tolerance was studied in order to validate the theory herein presented. Furthermore, many key findings were achieved throughout this process, such as the influence of element normals that, if not properly defined, could completely invalidate the model. Mesh dependency was also studied, considering findings taken from literature and the relation of 4 cohesive elements to 1 solid element was confirmed. Another determinant aspect analysed was the direct correlation between stress concentrations and the efficiency of the model. The effect of small-scale hexahedron elements was proved to be very influential and improvements were established to surpass this impediment. In the hopes of expanding over the main focus of this project, a material sub-routine was implemented to determine composite failure mechanisms, which, after a enormous amount of time, was eventually depicted as a limitation of the methodology. Overall, the results obtained affirmed the validity of the adopted modelling procedure and a coherent global-local technique was developed.

With respect to the wing-box model, a good shell model was defined and coherent results were achieved with low computational costs. Moving to the local models, poor results were nonetheless observed. As the main purpose of this project was to determine the validity of an one-way global-local technique that could achieve meticulous results whilst ensuring reduced time expenses, that objective was successfully achieved, albeit not for more complex structures. The exact same technique was implemented and highlighted limitations due to curvature and dimensions of the model.

In summary, we have successfully established a robust modelling technique, and the results obtained strongly affirm the appropriateness and validity of the adopted modelling methodology for the analysis of plane aircraft skin-stringer structures. Notwithstanding, some limitations were identified, which future research should focus on and that are highlighted in the following section.

10.2 Future work

Despite of the significant advancements achieved in the modelling and simulation of skin-stringer structures, some work must still be performed in order to reliably accomplish this task. Focusing on the plane structure, few limitations rose related to the definition of more complex regions. Although improvements were achieved, different mesh techniques could be investigated in order to mitigate the problem. In addition, as such shortcomings have been noted in literature, mainly the incorporation of inter and intralaminar damage in the same local model without requiring the introduction of two-way global-local techniques. Thereby, revisions into the standard methodology to overcome the limitation of pairing material sub-routines with sub-modelling procedures may be necessary. In addition, although delamination was successfully captured, research is still required to address the shortcoming observed in literature in terms of final delaminated area.

Lastly, and most importantly, severe limitations were observed for the displacement transition between more complex structures. Extensive research is thereby required, which may encompass the use of alternative modelling strategies. Within our work, it was postulated that increasing the complexity of the geometry, in terms of the presence of reasonable curved elements, may unable the transfer of displacement fields between models. Given the complexity of aeronautical structures, evaluating the reasons behind these adversities comprises a matter of the utmost importance that any future research into out methodology should focus on.

Bibliography

[1] A. Arteito, "Technology development and structural mechanics of composites built of spread tow thin-ply technology," *Master's Thesis*, 2012.

[2] I. Lapczyk and J. A. Hurtado, "Progressive damage modeling in fiber-reinforced materials," *Composites Part A: Applied Science and Manufacturing*, vol. 38, no. 11, pp. 2333–2341, 2007.

[3] N. Zimmermann and P. H. Wang, "A review of failure modes and fracture analysis of aircraft composite materials," *Engineering failure analysis*, vol. 115, p. 104 692, 2020.

[4] J. R. Vinson, "Sandwich structures: Past, present, and future," *Sandwich structures*, vol. 7, pp. 3–12, 2005.

[5] M. Arif, M. Asif, and I. Ahmed, "Advanced composite material for aerospace application—a review," in 2. Research India Publications, 2017, vol. 7, pp. 393–409. [Online]. Available: `https://www.ripublication.com/ijems17/ijemsv7n2_21.pdf`.

[6] R. Boyer, "Aircraft materials," in *Encyclopedia of Materials: Science and Technology*, K. H. J. Buschow, R. W. Cahn, M. C. Flemings, *et al.*, Eds. Oxford: Elsevier, 2001, pp. 66–73, ISBN: 978-0-08-043152-9. DOI: `https://doi.org/10.1016/B0-08-043152-6/00013-9`. [Online]. Available: `https://www.sciencedirect.com/science/article/pii/B0080431526000139`.

[7] C. Soutis, "Carbon fiber reinforced plastics in aircraft construction," *Materials Science and Engineering: A*, vol. 412, no. 1-2, pp. 171–176, 2005.

[8] A. A. Baker, *Composite materials for aircraft structures*. AIAA, 2004.

[9] M. A. Lepore, L. Ferrante, L. Sanguigno, and A. R. Maligno, "A non-crimp fabric mechanical characterization for the production of aerospace components," *Material Design & Processing Communications*, vol. 3, no. 5, e222, 2021.

[10] D. Gay, *Composite materials: design and applications*. CRC press, 2022.

[11] S. Rana and R. Fangueiro, *Advanced composite materials for aerospace engineering: processing, properties and applications*. Woodhead Publishing, 2016.

[12] G. La Rocca and M. J. van Tooren, "Knowledge-based engineering to support aircraft multidisciplinary design and optimization," *Proceedings of the Institution of Mechanical Engineers, Part G: Journal of Aerospace Engineering*, vol. 224, no. 9, pp. 1041–1055, 2010.

[13] X. Zhang, Y. Chen, and J. Hu, "Recent advances in the development of aerospace materials," *Progress in Aerospace Sciences*, vol. 97, pp. 22–34, 2018.

[14] P. Jerome, "Composite materials in the airbus a380-from history to future," in *Beijing: Proceedings 13th International Conference on Composite Materials (ICCM-13)*, 2001.

[15] L. A. Pilato and M. J. Michno, *Advanced composite materials*. Springer Science & Business Media, 1994.

[16] E. Shehab, W. Ma, and A. Wasim, "Manufacturing cost modelling for aerospace composite applications," in *Concurrent Engineering Approaches for Sustainable Product Development in a Multi-Disciplinary Environment: Proceedings of the 19th ISPE International Conference on Concurrent Engineering*, Springer, 2013, pp. 425–433.

[17] *Composites: Airbus continues to shape the future*, Aug. 2017. [Online]. Available: `https://www.airbus.com/en/newsroom/news/2017-08-composites-airbus-continues-to-shape-the-future`.

[18] B. Piquet, "Fast - special edition a350xwb," *Airbus technical magazine*, Jun. 2013, ISSN: 1293-5476. [Online]. Available: `https://aircraft.airbus.com/sites/g/files/jlcbta126/files/2022-04/FAST_specialA350.pdf`.

[19] H. Altenbach, J. Altenbach, W. Kissing, and H. Altenbach, *Mechanics of composite structural elements*. Springer, 2004, pp. 21–29.

[20] J. Rouchon, "Certification of large airplane composite structures," in *ICAS Congress Proceedings*, vol. 2, 1990, pp. 1439–1447.

[21] C. Niu and M. C.-Y. Niu, *Composite airframe structures: practical design information and data*. Adaso Adastra Engineering Center, 1992.

[22] R. Healey, J. Wang, W. K. Chiu, N. M. Chowdhury, A. Baker, and C. Wallbrink, "A review on aircraft spectra simplification techniques for composite structures," *Composites Part C: Open Access*, vol. 5, p. 100 131, 2021.

[23] G. A. Schoeppner and M. S. Tillman, "Composite structures durability design and substantiation," in *Long-term durability of polymeric matrix composites*, Springer, 2011, pp. 427–481.

[24] M. Weiland, "Low cost manufacturing and assembly of composite and hybrid structures," *Skyline*, vol. 18, p. 9, 2016.

[25] T. Dong and N. H. Kim, "Cost-effectiveness of structural health monitoring in fuselage maintenance of the civil aviation industry," *Aerospace*, vol. 5, no. 3, pp. 1–24, 2018. [Online]. Available: https://doi.org/10.3390/aerospace5030087.

[26] J. Schijve, "Fatigue damage in aircraft structures, not wanted, but tolerated?" *International Journal of Fatigue*, vol. 31, no. 6, pp. 998–1011, 2009.

[27] S. M. Tavares and P. M. De Castro, "Damage tolerance of metallic aircraft structures: Materials and numerical modelling," in Springer, 2019, pp. 17–23. [Online]. Available: https://doi.org/10.1007/978-3-319-70190-5_2.

[28] J. Lin, "Durability and damage tolerance analysis methods for lightweight aircraft structures: Review and prospects," *International Journal of Lightweight Materials and Manufacture*, 2022.

[29] F. De Florio, *Airworthiness: An introduction to aircraft certification and operations*. Butterworth-Heinemann, 2016.

[30] C. Boller and M. Buderath, "Fatigue in aerostructures—where structural health monitoring can contribute to a complex subject," *Philosophical Transactions of the Royal Society A: Mathematical, Physical and Engineering Sciences*, vol. 365, no. 1851, pp. 561–587, 2007.

[31] F. A. Administration, "Fatigue, fail-safe, and damage tolerance evaluation of metallic structure for normal, utility, acrobatic, and commuter category airplanes," *Advisory Circular*, vol. 23-13A, 2005.

[32] T. Mills, S. Prost-Domasky, K. Honeycutt, and C. Brooks, "Corrosion and the threat to aircraft structural integrity," in *Corrosion control in the aerospace industry*, Elsevier, 2009, pp. 35–66.

[33] R. Wanhill, L. Molent, S. Barter, and E. Amsterdam, "Milestone case histories in aircraft structural integrity," vol. NLR-TP-2002–521, 2002.

[34] F. A. Administration, "Damage-tolerance and fatigue evaluation of structure," *Advisory Circular*, vol. 25.571-C, 1998.

[35] F. A. Administration, "Advisory circular 20-107a," *Composite Aircraft Structure*, 1984.

[36] G. Negaard, "The history of the aircraft structural integrity program, aerospace structures information and analysis center report no," en, in *680.1B, Air Force Flight Dynamics Laboratory, Wright-Patterson Air Force Base*, Dayton, Ohio, 1980. [Online]. Available: https://apps.dtic.mil/dtic/tr/fulltext/u2/a361289.pdf..

[37] X. Jian and L. Yao, "Study on airworthiness requirements of composite aircraft structure for transport category aircraft in faa," *Procedia Engineering*, vol. 17, pp. 270–278, 2011.

[38] A. Administration, "Federal aviation administration, dot ards: Transport category subpart a — general," io, *Main*, no. 1, pp. 650–735, 2009.

[39] E.A.S.A., *Cs-25 certification specifications and acceptable means of compliance for large aeroplanes*, en, 2011.

[40] J. Tomblin, T. Lacy, B. Smith, S. Hooper, and A. Vizzini, "Review of damage tolerance for composite sandwich airframe structures," WICHITA STATE UNIV KS, Tech. Rep., 1999.

[41] T. Swift, "Damage tolerance certification of commercial aircraft," *Fatigue and Fracture*, vol. 19, pp. 566–576, 1996.

[42] F. A. Administration, "Composite aircraft structure," *Advisory Circular*, vol. 20-107B, 2009.

[43] A. Baker, A. J. Gunnion, and J. Wang, "On the certification of bonded repairs to primary composite aircraft components," *The journal of adhesion*, vol. 91, no. 1-2, pp. 4–38, 2015.

[44] J. Rouchon and M. Bos, "Fatigue and damage tolerance evaluation of structures: The composite materials response," 2009.

[45] J. H. Kweon, H. J. Son, J. Y. Choi, S. Y. Shin, J. H. Choi, and G. M. Lee, "Progressive failure analysis of unidirectional-fabric laminated composite joints under pin-loading," in *Key Engineering Materials*, Trans Tech Publ, vol. 334, 2007, pp. 1–4.

[46] M. K. Budzik, S. Heide-Jørgensen, and R. Aghababaei, "Fracture mechanics analysis of delamination along width-varying interfaces," *Composites Part B: Engineering*, vol. 215, p. 108 793, 2021.

[47] P. Liu and Z. Gu, "Finite element analysis of single-leg bending delamination of composite laminates using a nonlinear cohesive model," *Journal of Failure Analysis and Prevention*, vol. 15, pp. 846–852, 2015.

[48] P. Camanho and S. Hallett, *Numerical modelling of failure in advanced composite materials*. Woodhead Publishing, 2015.

[49] A. Turon, J. Costa, P. Maimi, D. Trias, and J. Mayugo, "A progressive damage model for unidirectional fibre-reinforced composites based on fibre fragmentation. part i: Formulation," *Composites Science and Technology*, vol. 65, no. 13, pp. 2039–2048, 2005.

[50] P. P. Camanho and C. G. Dávila, "Failure criteria for frp laminates in plane stress," Tech. Rep., Nov. 2003.

[51] R. Talreja, "Assessment of the fundamentals of failure theories for composite materials," *Composites Science and Technology*, vol. 105, pp. 190–201, 2014.

[52] V. Azzi and S. W. Tsai, "Anisotropic strength of composites: Investigation aimed at developing a theory applicable to laminated as well as unidirectional composites, employing simple material properties derived from unidirectional specimens alone," *Experimental mechanics*, vol. 5, pp. 283–288, 1965.

[53] R. Hill, "A theory of the yielding and plastic flow of anisotropic metals," *Proceedings of the Royal Society of London. Series A. Mathematical and Physical Sciences*, vol. 193, no. 1033, pp. 281–297, 1948.

[54] O. Hoffman, "The brittle strength of orthotropic materials," *Journal of Composite materials*, vol. 1, no. 2, pp. 200–206, 1967.

[55] S. W. Tsai and E. M. Wu, "A general theory of strength for anisotropic materials," *Journal of composite materials*, vol. 5, no. 1, pp. 58–80, 1971.

[56] Z. Hashin, "Fatigue failure criteria for unidirectional fiber composites.," Pennsylvania Univ Philadelphia Dept of Materials Science and Engineering, Tech. Rep., 1980.

[57] A. C. Orifici, I. Herszberg, and R. S. Thomson, "Review of methodologies for composite material modelling incorporating failure," *Composite structures*, vol. 86, no. 1-3, pp. 194–210, 2008.

[58] F.-K. Chang and K.-Y. Chang, "A progressive damage model for laminated composites containing stress concentrations," *Journal of composite materials*, vol. 21, no. 9, pp. 834–855, 1987.

[59] A. Puck and H. Schürmann, "Failure analysis of frp laminates by means of physically based phenomenological models," *Composites science and technology*, vol. 62, no. 12-13, pp. 1633–1662, 1998.

[60] P. P. Camanho, C. G. Dávila, S. T. Pinho, L. Iannucci, and P. Robinson, "Prediction of in situ strengths and matrix cracking in composites under transverse tension and in-plane shear," *Composites Part A: Applied Science and Manufacturing*, vol. 37, no. 2, pp. 165–176, 2006.

[61] L. Greszczuk, *Microbuckling of lamina-reinforced composites*. ASTM International, 1974.

[62] F.-K. Chang and L. B. Lessard, "Damage tolerance of laminated composites containing an open hole and subjected to compressive loadings: Part i—analysis," *Journal of composite materials*, vol. 25, no. 1, pp. 2–43, 1991.

[63] S. T. Pinho, C. G. Dávila, P. P. Camanho, L. Iannucci, and P. Robinson, "Failure models and criteria for frp under in-plane or three-dimensional stress states including shear non-linearity," Tech. Rep., Feb. 2005.

[64] P. Maimí, P. P. Camanho, J. Mayugo, and C. Dávila, "A continuum damage model for composite laminates: Part i–constitutive model," *Mechanics of materials*, vol. 39, no. 10, pp. 897–908, 2007.

[65] J. D. Lee, "Three dimensional finite element analysis of damage accumulation in composite laminate," *Computers & Structures*, vol. 15, no. 3, pp. 335–350, 1982.

[66] R. Christensen, "Stress based yield/failure criteria for fiber composites," *International journal of solids and structures*, vol. 34, no. 5, pp. 529–543, 1997.

[67] H. Huang, G. S. Springer, and R. M. Christensen, "Predicting failure in composite laminates using dissipated energy," *Journal of composite materials*, vol. 37, no. 23, pp. 2073–2099, 2003.

[68] J. Gosse and S. Christensen, "Strain invariant failure criteria for polymers in composite materials," in *19th AIAA Applied Aerodynamics Conference*, 2001, p. 1184.

[69] I. Raju and T. O'brien, "Fracture mechanics concepts, stress fields, strain energy release rates, delamination initiation and growth criteria," in *Delamination behaviour of composites*, Elsevier, 2008, pp. 3–27.

[70] G. R. Irwin, "Analysis of stresses and strains near the end of a crack traversing a plate," 1957.

[71] J. R. Reeder, "Composite materials handbook (CMH-17-1f)," vol. 1, no. 6. 2002.

[72] M. Aliha, R. Ashtari, and M. R. Ayatollahi, "Mode i and mode ii fracture toughness testing for a coarse grain marble," in *Applied mechanics and materials*, Trans Tech Publ, vol. 5, 2006, pp. 181–188.

[73] E. M. Wu and R. Reuter Jr, "Crack extension in fiberglass reinforced plastics," Illinois University: Department of Theroretical and Applied Mechanics, Tech. Rep., 1965.

[74] M. L. Benzeggagh and M. Kenane, "Measurement of mixed-mode delamination fracture toughness of unidirectional glass/epoxy composites with mixed-mode bending apparatus," *Composites science and technology*, vol. 56, no. 4, pp. 439–449, 1996.

[75] J. R. Reeder, "3-d mixed mode delamination fracture criteria-an experimentalist's perspective," in *American Society for composites 21st annual technical conference*, 2006.

[76] L. Tong, "An assessment of failure criteria to predict the strength of adhesively bonded composite double lap joints," *Journal of Reinforced Plastics and Composites*, vol. 16, no. 8, pp. 698–713, 1997.

[77] J. D. Whitcomb, *Analysis of instability-related growth of a through-width delamination*. National Aeronautics and Space Administration, Langley Research Center, 1984, vol. 86301.

[78] J. R. Reeder, "A bilinear failure criterion for mixed-mode delamination," *ASTM special technical publication*, vol. 1206, pp. 303–303, 1993.

[79] M. Smith, *ABAQUS/Standard User's Manual* (Damage Initiation for Fiber-Reinforced Composites), English. United States: Dassault Systèmes Simulia Corp, 2022.

[80] M. Smith, *ABAQUS/Standard User's Manual* (Damage Evolution and Element Removal for Fiber-Reinforced Composites), English. United States: Dassault Systèmes Simulia Corp, 2022.

[81] P. P. Camanho and C. G. Dávila, "Mixed-mode decohesion finite elements for the simulation of delamination in composite materials," Tech. Rep., 2002.

[82] C. G. Dávila and E. R. Johnson, "Analysis of delamination initiation in post-buckled dropped-ply laminates," *AIAA journal*, vol. 31, no. 4, pp. 721–727, 1993.

[83] P. Camanho and F. Matthews, "Delamination onset prediction in mechanically fastened joints in composite laminates," *Journal of Composite Materials*, vol. 33, no. 10, pp. 906–927, 1999.

[84] E. F. Rybicki and M. F. Kanninen, "A finite element calculation of stress intensity factors by a modified crack closure integral," *Engineering fracture mechanics*, vol. 9, no. 4, pp. 931–938, 1977.

[85] S. Rinderknecht and B. Kröplin, "A computational method for the analysis of delamination growth in composite plates," *Computers & Structures*, vol. 64, no. 1-4, pp. 359–374, 1997.

[86] D. S. Dugdale, "Yielding of steel sheets containing slits," *Journal of the Mechanics and Physics of Solids*, vol. 8, no. 2, pp. 100–104, 1960.

[87] G. I. Barenblatt, "The mathematical theory of equilibrium cracks in brittle fracture," *Advances in applied mechanics*, vol. 7, pp. 55–129, 1962.

[88] P. P. Camanho, *Numerical simulation of delamination growth in composite materials*. NASA Langley Research Center, 2001.

[89] M. Akterskaia, E. Jansen, S. R. Hallett, P. Weaver, and R. Rolfes, "Analysis of skin-stringer debonding in composite panels through a two-way global-local method," *Composite Structures*, vol. 202, pp. 1280–1294, 2018.

[90] R. Borg, L. Nilsson, and K. Simonsson, "Simulation of delamination in fiber composites with a discrete cohesive failure model," *Composites Science and Technology*, vol. 61, no. 5, pp. 667–677, 2001.

[91] D. Xie and A. M. Waas, "Discrete cohesive zone model for mixed-mode fracture using finite element analysis," *Engineering fracture mechanics*, vol. 73, no. 13, pp. 1783–1796, 2006.

[92] J. T.-S. Wang and S. B. Biggers, "Skin-stiffener interface stresses in composite stiffened panels," Tech. Rep., 1984.

[93] B. Falzon, G. Davies, and E. Greenhalgh, "Failure of thick-skinned stiffener runout sections loaded in uniaxial compression," *Composite Structures*, vol. 53, no. 2, pp. 223–233, 2001.

[94] C. Balzani and W. Wagner, "Numerical treatment of damage propagation in axially compressed composite airframe panels," *International Journal of Structural Stability and Dynamics*, vol. 10, no. 04, pp. 683–703, 2010.

[95] A. Riccio, A. Raimondo, and F. Scaramuzzino, "A robust numerical approach for the simulation of skin–stringer debonding growth in stiffened composite panels under compression," *Composites Part B: Engineering*, vol. 71, pp. 131–142, 2015.

[96] A. Raimondo and A. Riccio, "Inter-laminar and intra-laminar damage evolution in composite panels with skin-stringer debonding under compression," *Composites Part B: Engineering*, vol. 94, pp. 139–151, 2016.

[97] S. Hühne, J. Reinoso, E. Jansen, and R. Rolfes, "A two-way loose coupling procedure for investigating the buckling and damage behaviour of stiffened composite panels," *Composite Structures*, vol. 136, pp. 513–525, 2016.

[98] A. C. Orifici, I. O. de Zarate Alberdi, R. S. Thomson, and J. Bayandor, "Compression and post-buckling damage growth and collapse analysis of flat composite stiffened panels," *Composites science and technology*, vol. 68, no. 15-16, pp. 3150–3160, 2008.

[99] A. Brandt, "Multi-level adaptive technique (mlat) for fast numerical solution to boundary value problems," in *Proceedings of the Third International Conference on Numerical Methods in Fluid Mechanics: Vol. I General Lectures. Fundamental Numerical Techniques July 3–7, 1972 Universities of Paris VI and XI*, Springer, 2008, pp. 82–89.

[100] I. Parsons and J. Hall, "The multigrid method in solid mechanics: Part i—algorithm description and behaviour," *International Journal for Numerical Methods in Engineering*, vol. 29, no. 4, pp. 719–737, 1990.

[101] I. Parsons and J. Hall, "The multigrid method in solid mechanics: Part ii—practical applications," *International Journal for Numerical Methods in Engineering*, vol. 29, no. 4, pp. 739–753, 1990.

[102] L. Gendre, O. Allix, P. Gosselet, and F. Comte, "Non-intrusive and exact global/local techniques for structural problems with local plasticity," *Computational Mechanics*, vol. 44, pp. 233–245, 2009.

[103] Y. Liu, Q. Sun, and X. Fan, "A non-intrusive global/local algorithm with non-matching interface: Derivation and numerical validation," *Computer Methods in Applied Mechanics and Engineering*, vol. 277, pp. 81–103, 2014.

[104] M. Smith, *ABAQUS/Standard User's Manual* (Submodeling analysis), English. United States: Dassault Systèmes Simulia Corp, 2022.

[105] P. Linde, J. Pleitner, H. de Boer, and C. Carmone, "Modelling and simulation of fibre metal laminates," in *ABAQUS Users' conference*, vol. 421, 2004.

[106] J. B. Chang, V. K. Goyal, J. C. Klug, and J. I. Rome, "Composite structures damage tolerance analysis methodologies," 2012.

[107] A. Soto Masip *et al.*, "Development of efficient numerical models for the simulation of low velocity impact and compression after impact on composite structures," 2018.

[108] C. G. Dávila, C. A. Rose, E. V. Iarve, and F. A. Leone, "Modeling fracture and complex crack networks in laminated composites," in *Mathematical methods and models in composites*, World Scientific, 2023, pp. 439–496.

[109] S. Abdel-Monsef, B. Tijs, J. Renart, and A. Turon, "Accurate simulation of delamination under mixed-mode loading using a multilinear cohesive law," *Engineering Fracture Mechanics*, vol. 284, p. 109 233, 2023.

[110] C. Sarrado, A. Turon, J. Costa, and J. Renart, "An experimental analysis of the fracture behavior of composite bonded joints in terms of cohesive laws," *Composites Part A: Applied Science and Manufacturing*, vol. 90, pp. 234–242, 2016.

[111] S. A. Monsef, A. Ortega, A. Turon, P. Maimí, and J. Renart, "An efficient method to extract a mode i cohesive law for bonded joints using the double cantilever beam test," *Composites Part B: Engineering*, vol. 178, p. 107 424, 2019.

[112] S. A. Monsef, M. Pérez-Galmés, J. Renart, A. Turon, and P. Maimí, "The influence of mode ii test configuration on the cohesive law of bonded joints," *Composite Structures*, vol. 234, p. 111 689, 2020.

[113] A. Airoldi and C. G. Dávila, "Identification of material parameters for modelling delamination in the presence of fibre bridging," *Composite Structures*, vol. 94, no. 11, pp. 3240–3249, 2012.

[114] C. G. Dávila, C. A. Rose, and P. P. Camanho, "A procedure for superposing linear cohesive laws to represent multiple damage mechanisms in the fracture of composites," *International Journal of Fracture*, vol. 158, pp. 211–223, 2009.

[115] M. Smith, *ABAQUS/Standard User's Manual* (Cohesive Elements), English. United States: Dassault Systèmes Simulia Corp, 2022.

[116] G. Longo, "Models and methods to simulate low-energy impact damage on composite aerospace structures," 2011.

[117] B. Falzon and P. Apruzzese, "Numerical analysis of intralaminar failure mechanisms in composite structures. part ii: Applications," *Composite Structures*, vol. 93, no. 2, pp. 1047–1053, 2011.

[118] S. Pinho, L. Iannucci, and P. Robinson, "Physically-based failure models and criteria for laminated fibre-reinforced composites with emphasis on fibre kinking: Part i: Development," *Composites Part A: Applied Science and Manufacturing*, vol. 37, no. 1, pp. 63–73, 2006.

[119] M. PASI, "Caratterizzazione di un materiale composito e studio sperimentale di laminati per la validazione di modelli numerici di tipo "progressive failure"," 2011.

[120] L. Iannucci and J. Ankersen, "An energy based damage model for thin laminated composites," *Composites Science and Technology*, vol. 66, no. 7-8, pp. 934–951, 2006.

[121] Z. P. Bazant and M. Jirásek, "Nonlocal integral formulations of plasticity and damage: Survey of progress," *Journal of engineering mechanics*, vol. 128, no. 11, pp. 1119–1149, 2002.

[122] P. P. Camanho, C. G. Dávila, S. T. Pinho, *et al.*, "Progressive damage modeling of composite materials under both tensile and compressive loading regimes," in *Mechanical Response of Composites*, Springer, 2008, pp. 179–195.

[123] MatWeb, *Hexcel® HexTow® IM7 12K Intermediate Modulus Carbon Fiber (12,000 Filaments)*, `https://www.matweb.com/search/datasheet.aspx?matguid=0ec4ff24a0604bb2b89e492174d3bce4&ckck=1`, Accessed: 12/04/2023.

[124] K. W. Gan, S. R. Hallett, and M. R. Wisnom, "Measurement and modelling of interlaminar shear strength enhancement under moderate through-thickness compression," *Composites Part A: Applied Science and Manufacturing*, vol. 49, pp. 18–25, 2013.

[125] H. Cui, D. Thomson, A. Pellegrino, J. Wiegand, and N. Petrinic, "Effect of strain rate and fibre rotation on the in-plane shear response of±45 laminates in tension and compression tests," *Composites Science and Technology*, vol. 135, pp. 106–115, 2016.

[126] M. Ploeckl, P. Kuhn, J. Grosser, M. Wolfahrt, and H. Koerber, "A dynamic test methodology for analyzing the strain-rate effect on the longitudinal compressive behavior of fiber-reinforced composites," *Composite Structures*, vol. 180, pp. 429–438, 2017.

[127] M. Yasaee, G. Mohamed, A. Pellegrino, N. Petrinic, and S. R. Hallett, "Strain rate dependence of mode ii delamination resistance in through thickness reinforced laminated composites," *International Journal of Impact Engineering*, vol. 107, pp. 1–11, 2017.

[128] P. Kuhn, G. Catalanotti, J. Xavier, P. Camanho, and H. Koerber, "Fracture toughness and crack resistance curves for fiber compressive failure mode in polymer composites under high rate loading," *Composite Structures*, vol. 182, pp. 164–175, 2017.

[129] H. Cui, A. R. Melro, and M. Yasaee, "Inter-fibre failure of through-thickness reinforced laminates in combined transverse compression and shear load," *Composites Science and Technology*, vol. 165, pp. 48–57, 2018.

[130] J. Hoffmann, H. Cui, and N. Petrinic, "Determination of the strain-energy release rate of a composite laminate under high-rate tensile deformation in fibre direction," *Composites Science and Technology*, vol. 164, pp. 110–119, 2018.

[131] X. Xu, M. R. Wisnom, X. Sun, and S. R. Hallett, "Experimental determination of through-thickness compression (ttc) enhancement factor for mode ii fracture energy," *Composites Science and Technology*, vol. 165, pp. 66–73, 2018.

[132] H. Cui, D. Thomson, S. Eskandari, and N. Petrinic, "A critical study on impact damage simulation of im7/8552 composite laminate plate," *International Journal of Impact Engineering*, vol. 127, pp. 100–109, 2019.

[133] W. Ong, N. Rajic, W. Chiu, and C. Rosalie, "Adhesive material property evaluation for improved lamb wave simulation," *International Journal of Adhesion and Adhesives*, vol. 71, pp. 28–38, 2016.

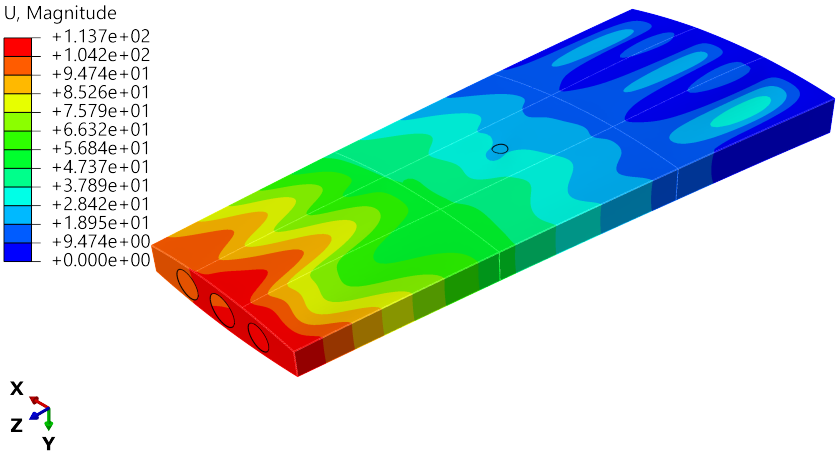
[134] B. d. Saint-Venant, "Memories des savants etrangers, vol. 14," *Paris Academie des Sciences, Paris, France (in French)*, 1855.

[135] G. Gerard and H. Becker, *NACA 3781 - Buckling of Flat plates.* 1957.

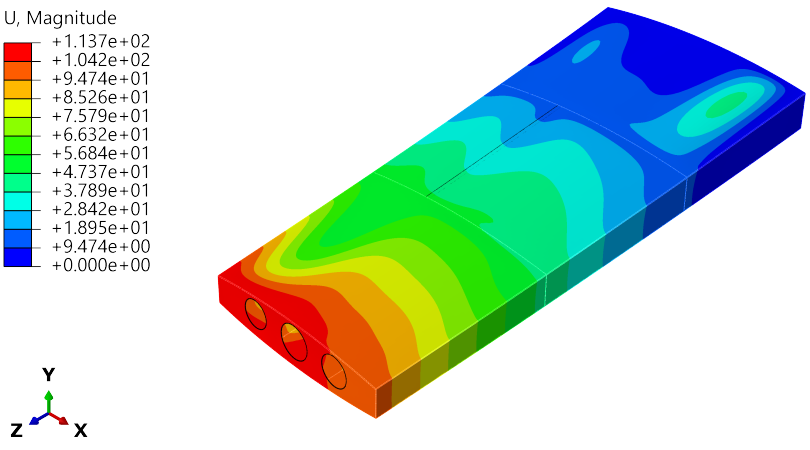
Appendix A

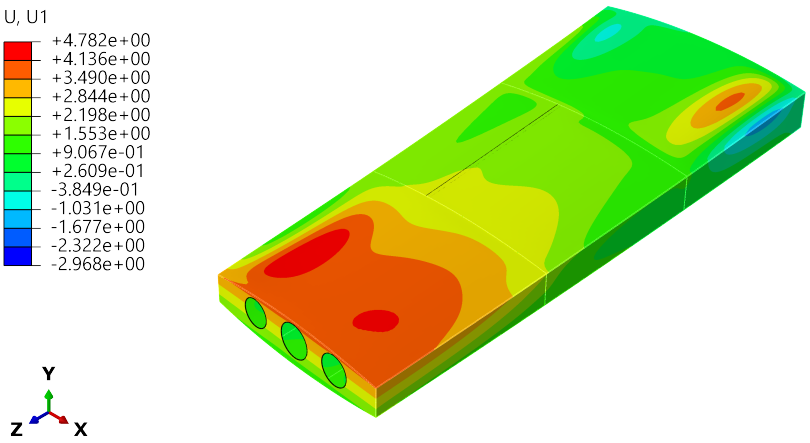
Wing-box Global Model Results

A.1 Displacement Field, U

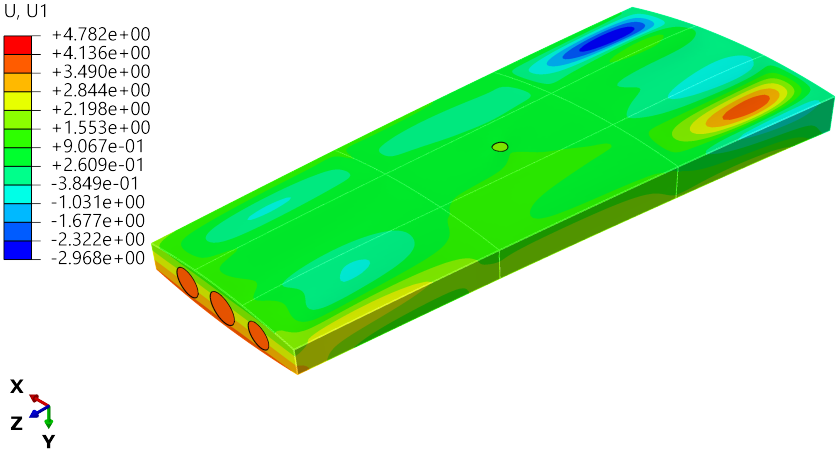


(a) Top view.



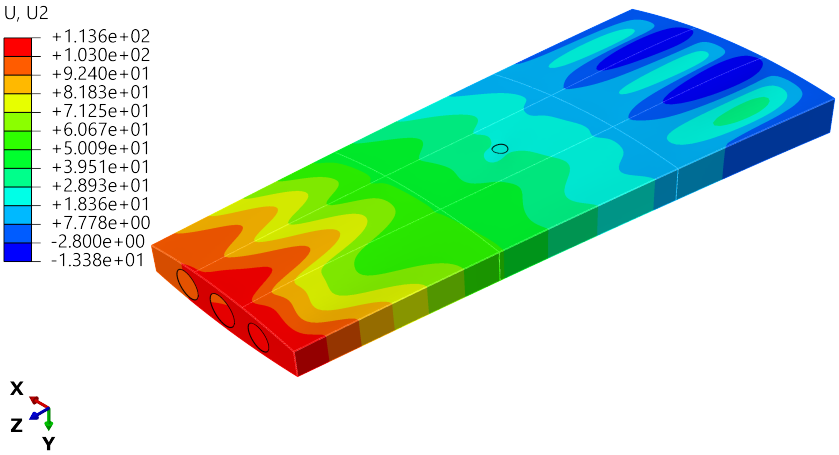


(a) Top view.

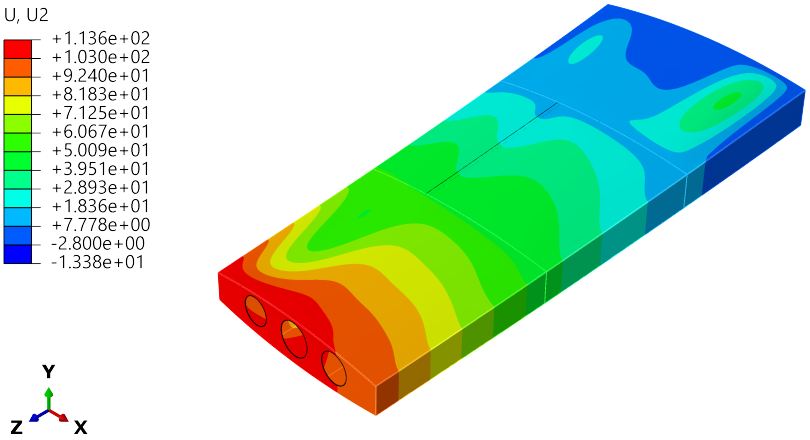


(b) Bottom view.

Figure A.2: Displacement field along the x-axis direction.

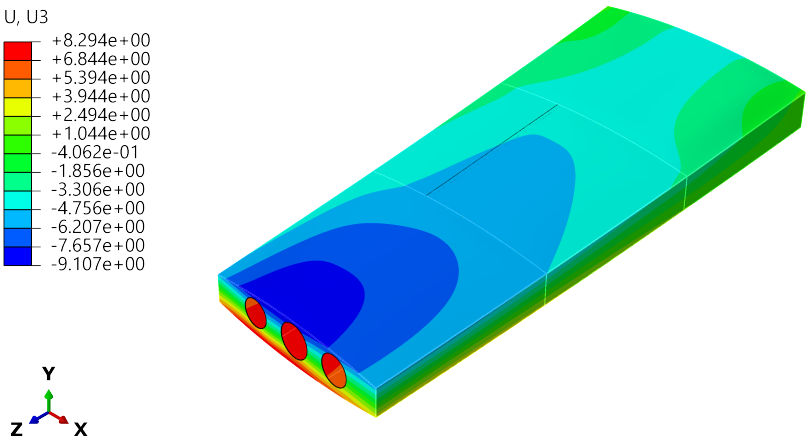


(a) Top view.

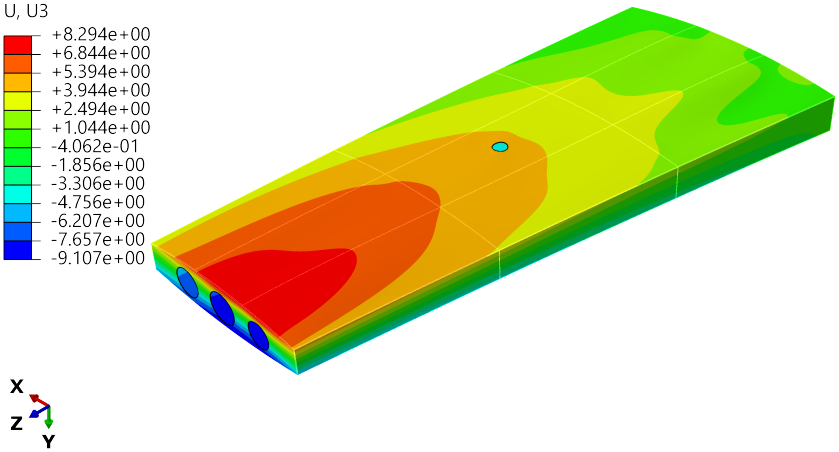


(b) Bottom view.

Figure A.3: Displacement field along the y-axis direction.



(a) Top view.



(b) Bottom view.

Figure A.4: Displacement field along the z-axis direction.